Skin Dose Measurement for Interventional Cardiology

A thesis
submitted in partial fulfilment
of the requirements for the Degree
of
Master of Science in Medical Physics

by

Andrew W. Blair (BSc)

Department of Physics and Astronomy
University of Canterbury
Christchurch, New Zealand
2009

Abstract

This thesis details the measurement and simulation of patient skin doses arising from X-ray exposure during interventional cardiology procedures. Interventional cardiology procedures can be long and complex resulting in high skin doses, to the extent that radiation burns may be produced. Twenty patients were used in the study consisting of 10 coronary angiogram and 10 coronary angioplasty procedures.

Radiochromic films were used to measure skin dose directly. The Gafchromic® XR-RV2 film was chosen for its suitability for this project. The key characteristics of this film were experimentally determined including: dose response, energy dependence, polarisation and post-exposure growth. The dose range was found to be ideally suited for the doses encountered in this study. Energy dependence was found to be ~14% between 60 and 125 kVp at 1 Gy and introduced an unavoidable uncertainty into dose calculations from unknown beam energies. Document scanner characteristics were also been investigated and a scanning protocol is determined.

A mathematical model was created to use the geometry and exposure information encoded into acquisition files to reconstruct dose and dose distributions. The model requires a set of study files encoded according to the DICOM format, as well as user input for fluoroscopic estimations. The output is a dose map and dose summary.

Simulation parameters were varied and results compared with film measurements to provide the most accurate model. From the data collected the relation between dose area product, maximum skin dose and fluoroscopic time were also investigated.

The results demonstrated that a model based on acquisition information can accurately predict maximum skin dose and provide useful geometrical information. The model is currently being developed into a standalone program for use by the Medical Physics and Bioengineering department.

Acknowledgments

Foremost, I would like to thank my supervisor Dr. Juergen Meyer. His enthusiasm and cheerful attitude have made it a pleasure to work with him. I am especially grateful for the assistance and encouragement to submit my work to a journal. Finally, I'd like to thank him for the huge effort in proof reading this thesis.

Near the beginning of this project I contacted Dr. Slobodan Devic (McGill University, Montréal) for assistance in radiochromic film matters. My plea was answered. His generous assistance and advice came when it was needed most. Without that I might never have made it to the simulations!

I would like to express my sincere gratitude to all the staff in the Christchurch Hospital Cardiology department, especially Dr David Smyth and Linda Dawe. Without their support and enthusiasm this project would have been in vain.

Thanks to all the folks at Medical Physics and Bioengineering for the support. Especially Dr Steven Marsh for the interesting discussions and Assoc Prof Richard Jones and Dr Nicholas Cook for helping proof read this work.

Finally, and most importantly, I would like to thank my family and friends. Thank you Mum & Dad for always being there and encouraging my interest in science. And especially thanks to Nicola for all the support and encouragement over the years.

I wish to gratefully acknowledge the financial assistance of: Clinical Training Agency for covering my MSc fees, University of Canterbury Masters Scholarship, and CMS Alphatech for providing comparator strips with the films.

Contents

List of Figures

Glossary

3D	*Three-Dimensional*
A/D	*Analog to Digital*
BSF	*Back Scatter Factor*
C/Angio	*Coronary Angiogram*
Cd/Caudal	*Caudal (away from head)*
CPE	*Charge Particle Equilibrium*
Cr/Cranial	*Cranial (towards the head)*
CR	*Computed Radiography*
DAP	*Dose Area Product*
DICOM	*Digital Information and Communications in Medicine*
FP	*Flat Panel*
GUI	*Graphical User Interface*
II	*Image Intensifier*
KVP	*Peak Kilovoltage*
OD	*Optical Density*
PACS	*Picture Archiving and Communications System*
PTCA	*Percutaneous Transluminal Coronary Angioplasty*
PV	*Pixel Value*
ROI	*Region of Interest*
SPD	*Source to Patient Distance*

1. Introduction

Cardiology is a branch of medicine dealing specifically with the heart. Every year millions of life saving operations are performed on the heart through the use of X-rays. These procedure are often referred to as interventional cardiology. In the USA alone over 2.4 million interventional cardiac procedures were performed in 2005 [1]. These procedures are performed by guiding thin wires through a patient's vessels under the guidance of X-rays. Thin tubes may also be inserted and contrast agent injected into the vessel. Through these techniques the cardiologist is able to map out the circulatory system of the heart and indentify blockages. The process of imaging cardiac arteries is referred to as *angiography* and is commonly abbreviated as C/Angio. Once a blockage is identified it can often be cleared through the use of intravenous balloons and held open by stents. This procedure is called an *angioplasty* and is commonly abbreviated as PTCA standing for Percutaneous Transluminal Coronary Angioplasty. The revolutionary aspect of interventional cardiology is that none of these procedures requires the patient to be "cut open". Open surgery and general aesthetic carry a significant risk with mortality rates as high as 7% for open heart surgery [2]. In contrast, interventional procedures only require a local anaesthetic and many patient's are able to walk around within hours of the procedure. This fact alone saves many lives as is reflected by the vastly lower mortality rate of around 0.2% for cardiac catheterisations [3].

The aim of this thesis is to develop a mathematical model to calculate and localise the maximum radiation dose to a patient who has undergone an interventional cardiology procedure. Before the motivation and approach are discussed, a brief historical introduction is given on the use of X-rays for diagnostic purposes.

1.1 History

The use of X-rays for diagnostic purposes is as old as the discovery of X-rays themselves. X-rays were first discovered by Wilhelm Roentgen over 100 years ago in 1895 [4]. At the time of discovery Roentgen was working on phenomena relating to high voltage electric current passing through low pressure gas [5]. His apparatus was enclosed in a light tight box and he observed that a nearby barium platincyanide coated screen fluoresced. For this reason barium platincyanide is often thought of as the first radiation detector [6]. Roentgen had planned to use this screen for future experiments therefore the discovery was not entirely accidental. Unsure of the nature of these rays he named them "X-rays", the X being the standard symbol for an unknown. His experiments showed these X-rays to be able to penetrate where ordinary light could not. Nearly two weeks later the worlds first radiograph

was taken of Roentgen's wife, Anna Bertha on 22 December 1885. Her hand is shown in Figure 1.1. The field of radiology was thus born and Roentgen was the father. Within a year of discovery scientists and doctors all over the world were experimenting with X-rays for research, imaging [7] and therapeutic purposes. By the end of 1896 more than 1,000 papers relating to x-rays had been published [8].

Figure 1.1. The first X-ray image [9].

The X-ray's enormous potential for medical imaging was quickly realised. As early as 7 January 1896 the morning edition of the Frankfurter *Zeitung* wrote:

> "At the present time, we wish only to call attention to the importance this discovery would have in the diagnosis of diseases and injuries of bones, provided that the process can be developed technically so that not only the human hand can be photographed but that details of other bones may be shown without the flesh." [8]

Chest radiography became an established clinical technique within years of the discovery of X-rays. It was particularly important for diagnosing tuberculosis, which was prevalent at the time. One of the first inventions in the field of radiology were the fluoroscopes. These devices, developed by many in 1896, consisted of a fluorescing screen and a surrounding hood to provide a darkened viewing environment. These scopes allowed the direct observation of objects in real time, although the image quality was inferior to static plates. As the years

progressed there were numerous advances in X-ray generation technology as well as imaging plate efficiencies.

Cardiac studies were a natural extension to chest radiography and as a result the field of cardiac radiology developed very early on. In 1906 the first contrast enhanced X-ray image was taken of a renal exam [10]. Contrast agents are a vital part of cardiology today. In 1929 Werner Forssmann performed a landmark procedure on himself by inserting a catheter into his antecubital vein and guiding it under fluoroscopy to his heart [11]. Over the next two years Forssmann conducted further operations investigating the use of contrast media for imaging chambers of the heart, including examinations on himself. He was awarded the Nobel Prize for medicine in 1956. The next significant advancement in cardiology was in 1953 when the first image intensifier system was made commercially available. Image intensifiers use a photocathode to convert fluorescent light into electrons which are then electrically accelerated and then converted back into light via a phosphor. The image intensifier provided huge gains in X-ray efficiency. Not only that but it was possible to attach a video camera to the output window and record the examination and cardiac cinematography soon became commonplace.

Modern day catheterisation labs consist of high capacity, water cooled X-ray tubes, high efficiency image intensifiers or digital detectors and safe, organic iodine based, contrast agents.

1.2 Motivation

Although X-rays have contributed enormously to medicine since they were first discovered, their use is not without consequence. The deleterious affects of X-rays were first observed on the hands of fluoroscopic operators [8]. When using the fluoroscope, operators would often place their hand in the beam to test its strength. This resulted in numerous cases of dermatitis to the hands and face of operators. One of Thomas Edison's assistants, Clarence M. Dally became the first X-ray martyr when he died in 1904 [8]. Many similar cases of serious burns and dermatitis lead to an appreciation for the harmful affects that X-rays have on the body. Thus the focus of radiology began to include methods to reduce patient and operator exposure in addition to providing higher quality images. That focus continues today and is the dogma of radiation protection agencies around the world [12].

During a cardiac catheterisation procedure the radiation dose to a patient's skin can become great enough that a burn may be produced. Although rare, even worse cases of severe ulceration and ischemic necrosis have been reported [13,14]. The risk of radiation damage to patients in cardiology has been highlighted by many authors [15-21].

At present very few machines give any kind of realistic estimation of skin dose. The machines at Christchurch Hospital are typical for catheterisation labs and provide only dose

area product (DAP) and total fluoroscopic time as radiation measures. DAP will be discussed in Chapter 2. DAP has already been shown to be a very poor indicator of maximum skin dose by Vano et al [22]. Therefore the interventionalist has no way of knowing the maximum dose and no way of being able to locate where on the patient it may be.

Although completing the procedure is likely to overrule any radiation protection concerns (i.e., heart problems carry a far greater risk than the radiation), frequently patients will need to return to the cath lab within days of a previous exam. When they return it would be advantageous for the cardiologist to know if the patient was at risk of deterministic effects and where they might occur. That way the cardiologist could attempt views on a different orientation or other aggressive dose saving measures. It could also be used to identify those patients at risk of developing skin complications so that appropriate post operative care can be given.

The aim of this thesis is to develop a model for predicting magnitude and location of maximum skin dose based on information which is routinely available. The difficulty in this task becomes apparent when a selection of fields are mapped out as shown in Figure 1.2. The fields were calculated using the dose calculation software PCXMC [23] for a simple coronary angiogram. Outlines were traced to produce the larger image. It can be seen that the amount of overlap is rather complex and will be very dependent on exact geometry and positioning. The best system at present is a proprietary program for calculating maximum dose in real time [24]. The system is called CareGraph™ and is available on certain Siemens (Siemens Medical, Erlangen, Germany) machines for a cost. Aside from the cost of the system other limitations are that the program will only work on specific machines, and of course only on Siemens machines.

The next section describes the approach that was used to produce the final model.

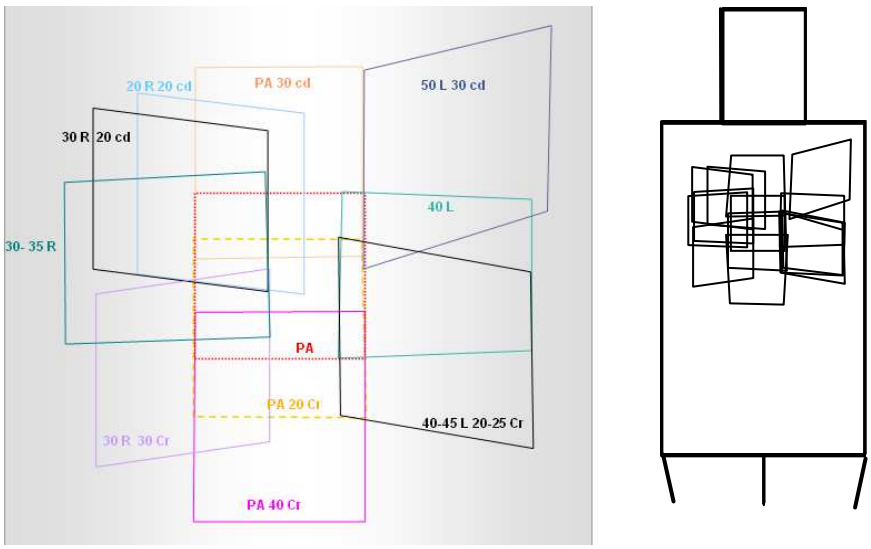

Figure 1.2. Overlapping fields from a typical coronary angiogram.

1.3 Summary of Approach

The approach used is broadly similar to that of Morrell and Rogers [25]. To the author's knowledge this is the only published work at the time of writing on the subject of retrospective reconstruction. The method developed will be extended beyond Morrell and Rogers by using better films and more dose estimation options.

The summary of the approach is as follows:

1. Before any simulations are made, the true dose distribution must be found in order to make comparisons. The only practical way to achieve a complete dose measurement across a large surface area is to use films. Large film sheets were placed under the patient's back and therefore were exposed identically to the patient's skin. Two suitable types of film exist; radiographic and radiochromic. Conventional radiographic film, as used by Morrell and Rogers, is typically designed for taking radiographs and tends to saturate easily. In this study the radiochromic film Gafchromic® XR-RV2 was used. Gafchromic® XR-RV2 is specially designed to be sensitive to the dose ranges encountered in fluoroscopic interventional procedures and is available in large 14" x 17 " sheets. The properties of this film are investigated in Chapter 3.

2. Reconstruction of the radiation fields was performed and simulated by using the geometrical data contained within the stored acquisition data files. This is possible owing to the DICOM standard, which requires certain information be encoded into all medical images. A number of methods for dose estimation were investigated. The reconstruction process is discussed in Chapter 4.

3. The final step was to compare the film measurements and simulations. Many simulations can be made based on different parameter estimates and assumptions. The best set of simulations can be found by comparison with the film measurements. These results as well as some other interesting findings are presented in Chapter 5.

For completeness, the next chapter (Chapter 2) provides background information relating to these topics.

2. Background

In this chapter some basic background information is provided. First the underlying principles of radiation physics and radiobiology are presented. Following that the important dose area product metric is described. Finally a brief description of a cardiac cath lab is given including some basic procedures.

2.1 Radiation Interactions with Matter

Radiation interactions with matter can be grouped into two categories: charged particle interactions and non-charged particle interactions. Charged particles such as electrons and protons are directly ionising and they can interact and ionise atoms via coulomb forces. Uncharged particles such as photons and neutrons are indirectly ionising, these interactions produce energetic electrons, which in turn can cause ionisation. It is these energetic electrons, which deposit energy via ionisation and damage cells.

2.1.1 Photons

When a photon interacts with an atom there are four effects which may be observed; photoelectric absorption, Rayleigh scattering, Compton scattering and pair production. Specific mechanics of these interactions can be found in elementary radiation physics books such as Johns & Cunningham [26] or Khan [27]. For dosimetry at diagnostic energies, only photoelectric absorption and Compton scattering are important. At low energies or in high Z material, the photoelectric process dominates. This is significant since essentially all energy is transferred to the electron in the photoelectric process. The following figures (Figure 2.1, Figure 2.2), generated by XMuDat [28], provide a summary of the relative importance for each interaction. For low Z materials such as tissue (Figure 2.1), the photoelectric and Compton effect become equal at roughly 30 keV. Whereas for a high Z material such as lead (Figure 2.2), the photoelectric process dominates right up to 500 keV.

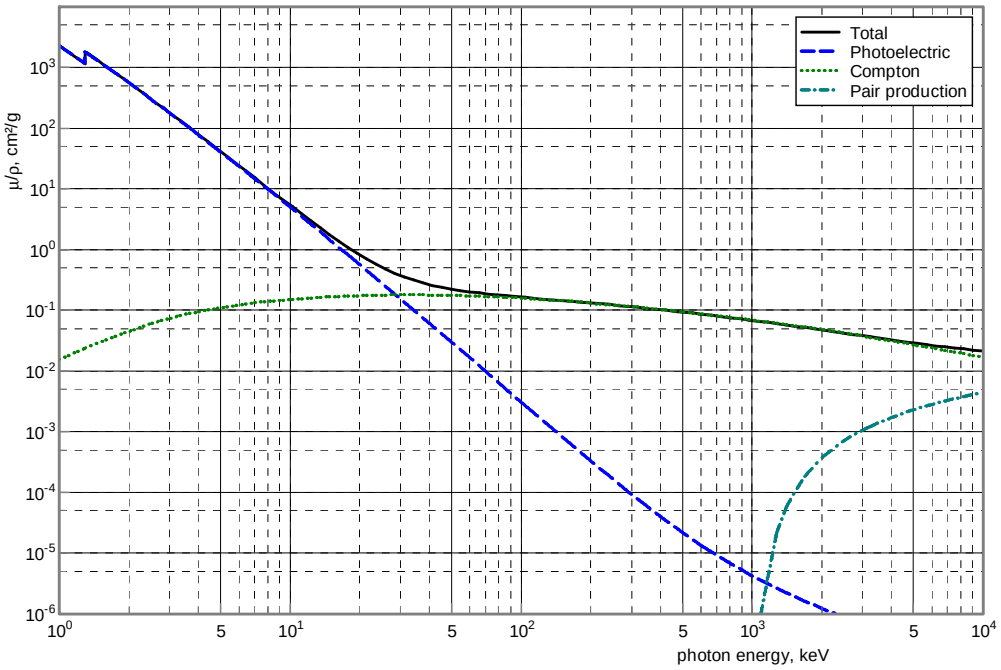

Figure 2.1. Photon attenuation coefficients for a tissue equivalent material.

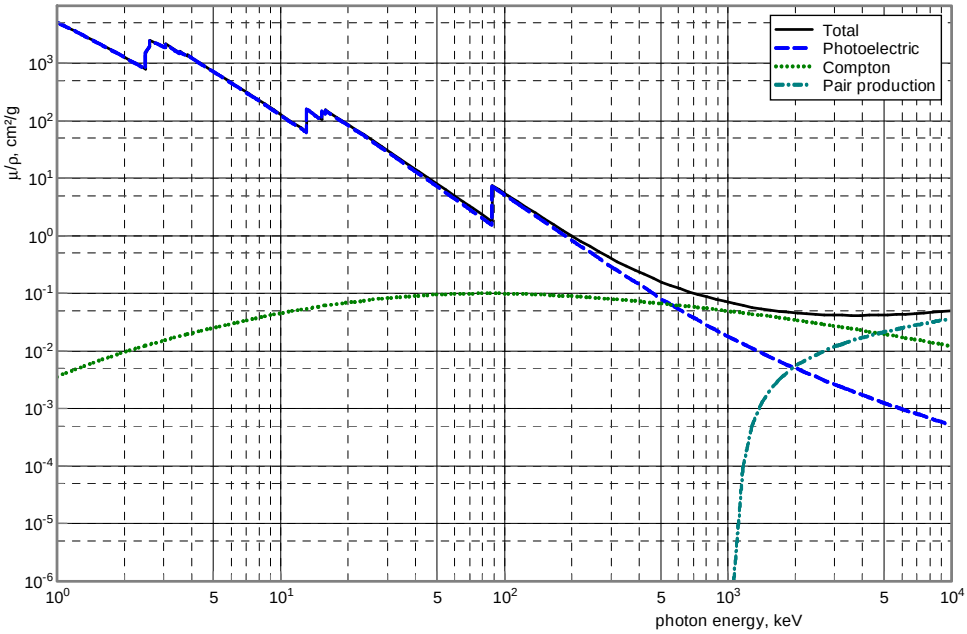

Figure 2.2. Photon attenuation coefficients for lead. Note the distinct K, L and M photoelectric absorption peaks.

2.1.2 Electrons

Electrons lose energy via excitation, ionisation and radiative losses. As electrons move through matter they are continually subject to coulomb forces by any charged particles in proximity. The energy lost depends upon $1/b^2$ and $1/v^2$ where b is the impact parameter (path of closest approach) and v is the speed of the electron [26]. If the force between a travelling electron and an atom is not sufficient to liberate any bound electrons, then the atom will be

left in an excited state; this is an *excitation* loss. Likewise, when the forces are strong enough then electrons will be liberated thus *ionising* the atom. In fact, an electron may gain enough energy from the ionisation that it may create its own ionisation tracks. A highly energetic electron produced in this way is called a δ-ray.

In a different type of interaction the electron may lose energy radiatively. Should an electron pass close to a nucleus, the highly concentrated charge of the nucleus will cause the electron to be deflected significantly. This deceleration causes the electron to emit X-rays as a radiative loss. The name given to this type of radiation is *Bremsstrahlung*, from the German word for *braking radiation*. The amount of energy the electron radiates depends on the impact parameter, the charge of the nucleus and the energy of the electron. For this reason when a stream of electrons collides with a target, a whole spectrum of energies is produced ranging from almost zero energy, up to the maximum energy of the incident electrons. The proportion of energy an electron radiates via bremsstrahlung is proportional to the energy of the electron. At diagnostic energies the bremsstrahlung efficiencies are very low, for example at 100 kVp electrons striking the target lose over 99% of their energy as ionisational losses that lead eventually to heat. For comparison, at high energies such as those produced in a linear accelerator only approximately 5% of the electron's energy is lost via ionisation, the rest appearing as bremsstrahlung [26].

2.2 Dosimetric Quantities

The International Commission of Radiological Units (ICRU) has defined the following quantities and units in ICRU report 33 (1980) [29].

***Exposure(X)*:** Exposure is a measure of a radiation's ability to ionise air.

$$X = \frac{dQ}{dm} \tag{2.1}$$

where dQ is the absolute value of the total charge of the ions of one sign produced in air when all the electrons liberated by photons in air of mass dm are completely stopped in air.

The original unit of exposure is the Roentgen, where $1R = 2.58 \times 10^{-4}$ C/kg. Exposure is difficult to measure above a few MeV and below a few keV making it of little use for radiotherapy but still quite useful in diagnostic radiology.

***KERMA*:** Kinetic Energy Released per unit MAss. This quantity refers to the average *energy transferred to kinetic energy of charged particles* in small mass and is applicable for indirectly ionising radiations. Mathematically it is dE/dm where dE is the kinetic energy transferred from photons to electrons in a mass dm with units of J/kg. Of the initial energy imparted to the charged particles not all will be deposited in the surroundings. Some of these charged particles may radiate energy via bremsstrahlung. For this reason kerma is often split into two principal components; a radiative, and a collisional kerma. The collisional kerma can be expressed as:

$$K_{col} = \Psi\left(\frac{\mu_{en}}{\rho}\right)_{E,Z} \tag{2.2}$$

where Ψ is the photon fluence and $(\mu_{en}/\rho)_{E,Z}$ is the mass energy absorption coefficient at an energy E in a material with atomic number Z.

***Absorbed Dose*:** Collisional Kerma is closely related to absorbed dose which makes it a highly useful quantity. It is important to note however that kerma and absorbed dose do not occur at the same place. Kerma is defined in a particular volume whereas absorbed dose will be deposited by the ion track in another volume further 'downstream'. While kerma can be calculated from photon fluence via Eq.(2.2), dose cannot be unless some sort of equilibrium exists between the two. As a beam passes through a material electrons will be set in motion and a dose will be deposited. An equilibrium between dose and kerma is reached when for every electron that terminates in a small volume, another electron is created and exits the same volume. This condition is called Charged Particle Equilibrium (CPE). The depth at which this occurs depends on the material and the energy of the beam. Under CPE, the absorbed dose is equal to the kerma minus energy lost via bremsstrahlung (Figure 2.3). Exposure can be calculated from collisional kerma by calculating the charge produced per unit of energy deposited. The mean energy required to produce an ion pair in dry air is $\overline{W}$ =33.97 eV/ion pair [27]. $\overline{W}/e$ is then the average energy per unit charge required to produce an ionisation. Thus:

$$D_{air} \overset{CPE}{=} (K_{col})_{air} = X \cdot \left(\frac{\overline{W}}{e}\right)_{air} \tag{2.3}$$

Realistically, CPE can be achieved in air for energies below that of ^{60}Co (~1.25 MeV) [26]. In mediums denser than air CPE is never achieved due to stronger attenuation. Instead a condition of transient CPE (TCPE) exists, see Figure 2.3. Under these conditions the absorbed dose is given by:

$$D = \beta \cdot \Psi \left(\frac{\mu_{en}}{\rho} \right) \tag{2.4}$$

Where $\beta = D/K_{col}$. The dose to one medium can be calculated from another by:

$$\frac{D_1}{D_2} = \frac{(\beta \cdot \mu_{en} / \rho)_1 \Psi_1}{(\beta \cdot \mu_{en} / \rho)_2 \Psi_2} \tag{2.5}$$

Further details on calculating absorbed dose can be found elsewhere [30].

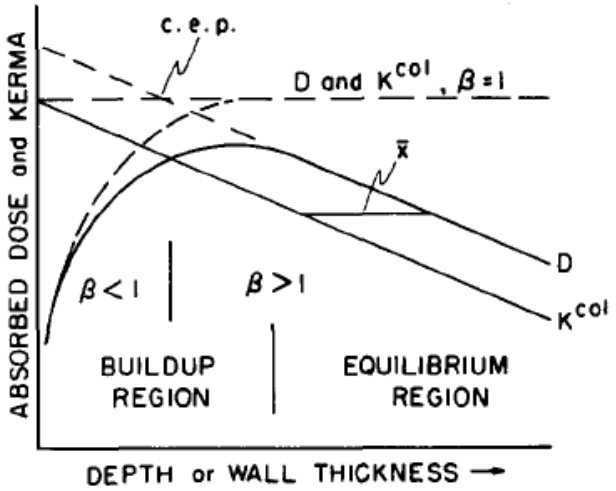

Figure 2.3. Relationship between kerma and dose [30]. The collision kerma decreases with depth as the photon beam is attenuated. As the electrons produced deposit energy the dose increases until the number of electrons produced and stopped reaches an equilibrium. Due to attenuation of the medium this state is called Transient Charged Particle Equilibrium (TCPE).

2.3 Dose Area Product

The dose area product, henceforth denoted as DAP, is a common radiation measurement quantity in the diagnostic world and is referred to repeatedly in this thesis. As its name implies, DAP is the dose of a beam multiplied by its area:

$$DAP = Dose \times Area\,.$$

The SI units for DAP would be Gym^2 however it is most commonly expressed in units which give the most appropriate number of significant figures, for example $Gycm^2$ is the most common unit for DAP measurements. The reason this is a useful metric is that the dose decreases as the square of the distance from the source while the area increases as the square of the distance, thus DAP is independent of distance from the source as illustrated in Figure 2.4. Provided the beam area is known at a particular distance then the dose can be calculated at any distance as well. In addition the DAP provides a more intuitive estimate of risk since radiation burden to the patient is not only a function of dose, but also of area, i.e., greater exposed area results in more cells being irradiated.

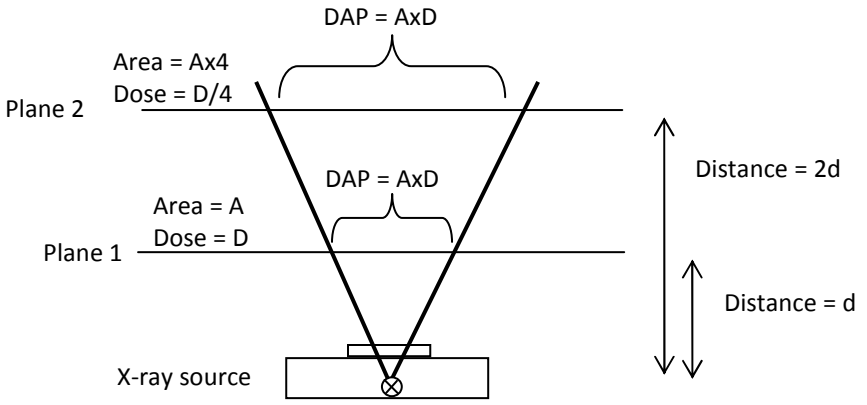

Figure 2.4. Illustration of the DAP principle.

To measure the DAP being output by a machine, a special DAP meter is usually used. The DAP meter is fitted just beyond the X-ray collimators and is positioned to fully intersect the beam much like the monitor chamber used in radiotherapy (Figure 2.5). It is essentially an ion chamber which measures the ionisation produced in its sensitive volume and then reports the product of dose and area.

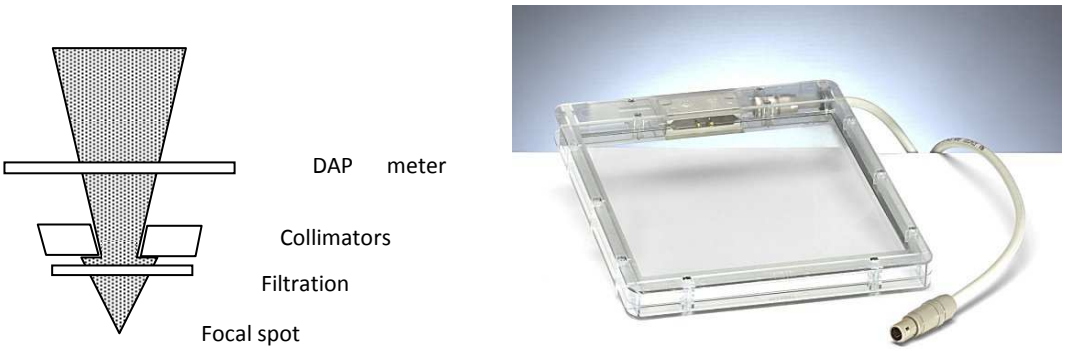

Figure 2.5. Left: The DAP chamber is usually positioned just after the collimators and always after added filtration. Right: A Diamentor® DAP chamber (PTW, Freiburg, Germany).

Limitations

As mentioned in Chapter 1, the DAP and fluoroscopic time are the only two pieces of dosimetric information available to the operator. And while it is a very useful metric as described above, it does have limitations. One such limitation is when trying to use DAP as a risk estimate for unknown table heights. As the table height is lowered the patient moves closer to the X-ray source and the dose rate increases with the inverse square law, the DAP however remains unchanged as illustrated in Figure 2.6. A patient closer to the X-ray tube therefore has a much greater risk of skin damage and this is not reflected by the DAP.

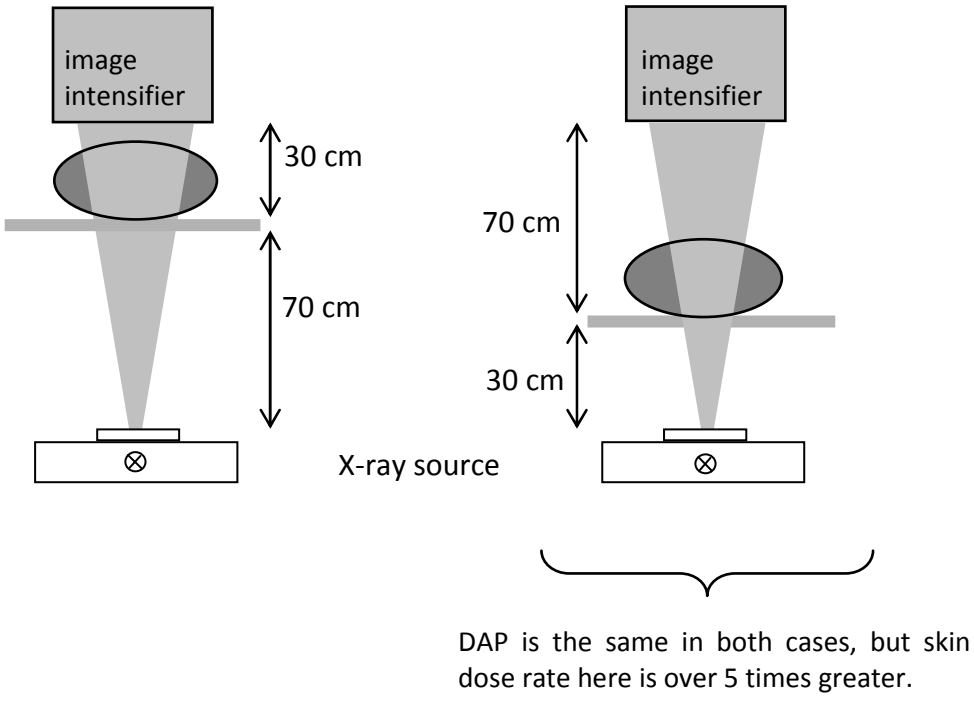

Figure 2.6. Demonstration of how dose and DAP are affected by table height.

Likewise, when the tube rotates around the patient at some angle, the intensity of the X-rays on the patient's skin varies, parts of the skin are closer to the tube and receive a higher dose than more distant skin as illustrated in Figure 2.7. As the DAP meter is fixed to the tube it does not take account of any angulations effects.

The final limitation is that the DAP contains no spatial information, it is only a measure of total dose output from the X-ray tube.

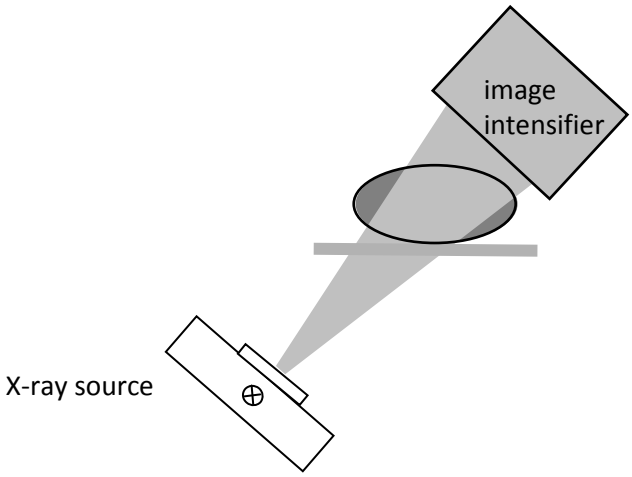

Figure 2.7. Effect of changing beam area with angle.

2.4 Radiobiology and Tissue Interactions

2.4.1 Mechanisms of Damage

As radiation passes through tissue it induces ionisations and excitations in the molecules that make up the tissue. Tissue damage may then occur via two mechanisms as illustrated in Figure 2.8 [31]:

- Direct action. Under direct action a free electron is created from the incident radiation. The free electron may then interact with a DNA molecule and alter it in some way.
- Indirect action. As with direct action a free electron is produced, however the electron then interacts with water molecules and produces a free radical. This free radical then goes on to damage the DNA. For sparsely ionising radiation such as X-rays, indirect action is the dominant mechanism [31].

When a DNA molecule is damaged it may either repair, die, or mutate. A paradigm for radiation injury from initial ionisation is shown in Figure 2.9 from Hall and Giaccia [31]. Of particular importance is the time scale. While the initial ionisation takes merely a second, the after effects can present anywhere from days to years and even generations later. In this thesis it is the *early* and *late effects* occurring from cell death which are of the most concern. From this paradigm it can be seen that these effects can manifest between days and months, perhaps even a few years post exposure.

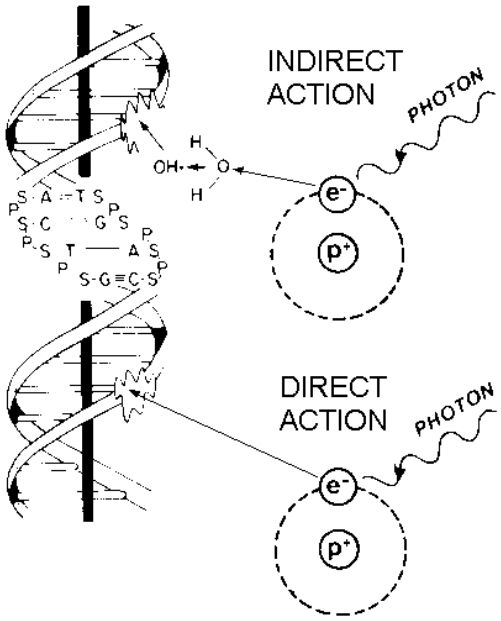

Figure 2.8. Direct and Indirect mechanisms of tissue damage [31].

A word of caution however, the paradigm is constantly changing to reflect the most up to date scientific evidence as many of these principles are poorly understood. For example, there is much evidence to suggest that cells in the vicinity of radiation, although not actually irradiated, will undergo death or mutations as if they were irradiated [32]. This effect is known as the *bystander effect* and could alter the paradigm presented in Figure 2.9.

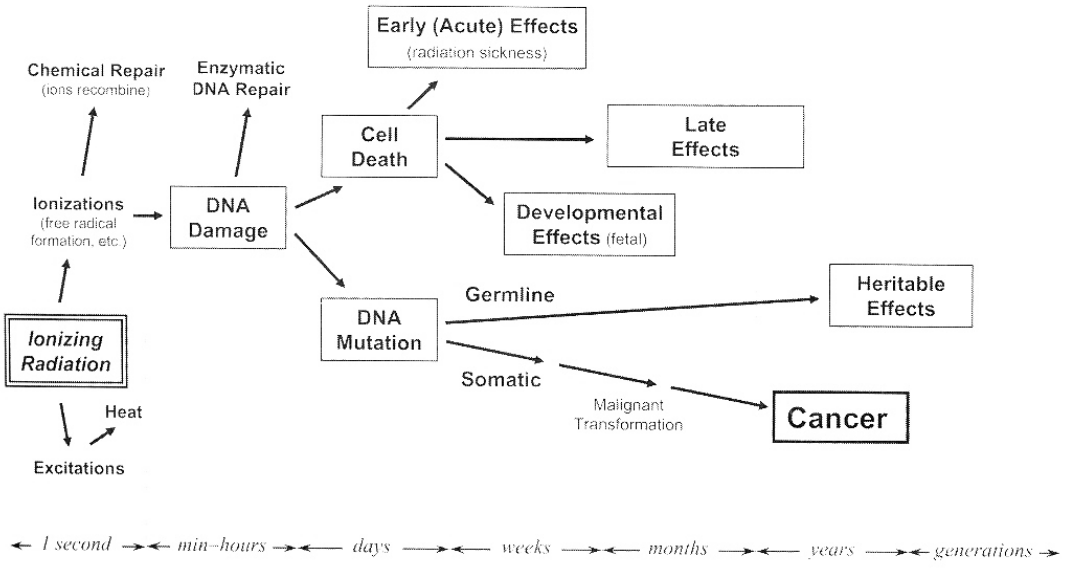

Figure 2.9. Classic paradigm of radiation injury [31].

2.4.2 Stochastic and Deterministic Risks

To continue from the previous section the outcome of DNA damage is discussed here. A DNA molecule that fails to successfully repair may die via apoptosis (programmed death) or the cell itself may produce nonviable offspring, alternatively it may not die but instead produce viable but modified offspring. The impact of these two outcomes have vastly different effects on the person irradiated. Most tissues in the body can sustain the unexpected loss of a few cells. Eventually however the loss of cells will become great enough that the organ begins to lose function and as more cells are lost the function worsens. This type of effects is called a *deterministic effect*. Deterministic effects have a *threshold* below which the organ is able to fully function. Once this threshold is exceeded the effect becomes more severe with increased dose. Radiation skin burns are such an example. Deterministic effects are of most interest to this work as it is the extent and location of skin damage that we seek to predict.

On the other hand, if the cell were to survive the irradiation but produce altered offspring then the outcome will be very different. The altered offspring may at some time give rise to carcinogenesis in somatic cells or hereditary defects in germ cells. The chance that a defect will be induced is proportional to the dose delivered to a cell, however the severity of the mutation is not. These type of effects are termed *stochastic effects*. Stochastic effects are assumed to have no threshold and their incidence increases with dose while the severity does not. Cancer induction is an example of a stochastic effect.

2.4.3 Skin Damage

As discussed previously, skin damage is an example of a deterministic effect that occurs due to cell death via radiation. Due to exponential attenuation for kilovoltage energies the skin usually receives the highest radiation dose of all the organs for external beam sources. It is not surprising that the first indication that X-rays may have harmful effects on human tissues were discovered through skin injuries of early users [8].

Different forms of skin damage will manifest depending on the magnitude of dose delivered. The forms of skin damage are outlined in Table 2-I including the dose threshold and onset time, adapted from [33]. The mildest effect is a transient erythema reaction with a minimum dose of 2 Gy. It manifests as a reddening of the skin. At around 3 Gy a temporary epilation (hair loss) may be noticed. Beyond this a main erythema occurs and has symptoms very much like sunburn however the mechanism is different and the onset time is much greater (~2 weeks) (Figure 2.10, a). Above 10 Gy a telangiectasia may be noticed with an onset time of around one year. Telangiectasia is a condition where small superficial veins dilate and become visible on the skins surface, similar to varicose veins (Figure 2.10, b). Desquamation can occur above 14 Gy and refers to when the layers of skin begin to shed (Figure 2.10, d). At

18 Gy and above the injuries become debilitating and result in a serious wound. Ischemic dermal necrosis occurs when the underlying blood supply to the dermis is damaged to a point where the skin cannot be sufficiently oxygenated. With time the skin slowly suffocates leaving patches of necrotic skin (Figure 2.10 e). With even greater dose the dermis and epidermis may be damaged outright beyond repair leading to permanent ulceration within weeks (Figure 2.10 f).

All of these types of skin damage have been observed on patients who have under gone cardiac catheterisations as illustrated in Figure 2.10.

Table 2-I. Dose thresholds for skin damage [33].

Threshold (Gy)	Effect	Time till onset
2	Early erythema	hours
3	Temporary epilation	~ 3 weeks
6	Main erythema	~ 2 weeks
7	Permanent epilation	~ 3 weeks
10	Telangiectasia	> 52 weeks
14	Dry desquamation	~ 4 weeks
18	Moist desquamation	~ 4 weeks
18	Ischemic necrosis	> 10 weeks
24	Secondary ulceration	> 6 weeks

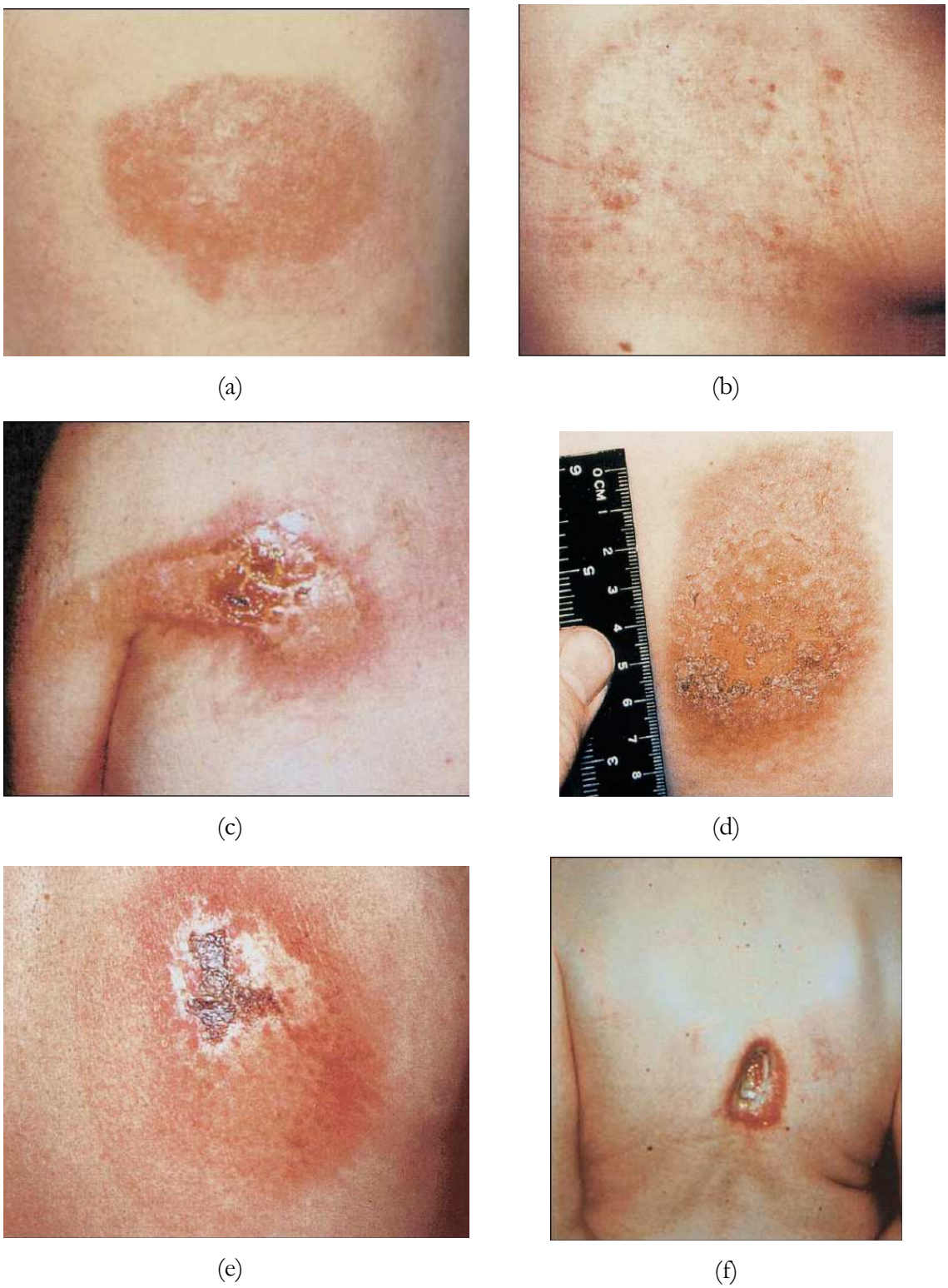

Figure 2.10. Examples of skin damage from fluoroscopic procedures. a) Main erythema. b) Telangiectasia, note the square radiation field is clearly visible. c) Ulceration over the scapula resulting from two overlapped fields. d) Erythema with desquamation. e) Necrosis with surrounding erythema. f) Severe ulceration, photo was taken 17 months post exposure. Source: Koenig et al 2001 [34].

2.5 The Cardiac Lab

2.5.1 Overview

The aim of a cath lab is to diagnose and treat a range of heart conditions without open heart surgery. To operate a cath lab requires a group of skilled personal. A typical team will consist of:

- 1-2 Cardiologists.
- 1-2 Radiographers.
- 1-2 Scrub nurses.
- 1 Cardiac technician.

The cath lab used in this study is shown in Figure 2.11 with the key features identified.

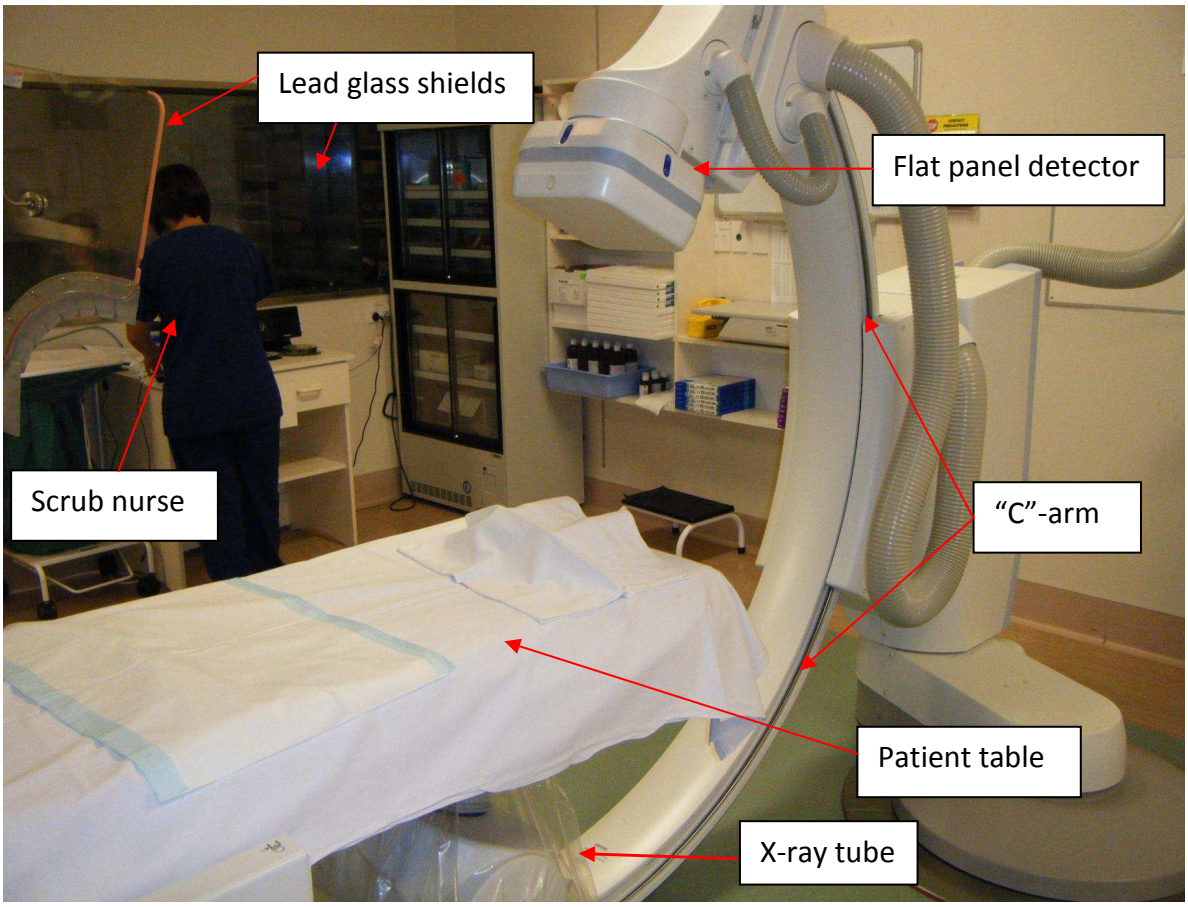

Figure 2.11. Layout of a typical Cath lab.

The most standard procedure performed is an angiogram. This is where the vessels of the heart are imaged in order to locate blockages or valve deficiencies etc. To perform an angiogram the following procedure takes place:

1. A catheter guide wire is inserted into the patient's peripheral artery, the femoral or axial artery are the most common.
2. A hollow tube capable of injecting contrast agent is slid down the catheter.
3. The wire is guided intravenously to the heart under fluoroscopy with the aid of contrast agent if necessary.
4. Contrast agent is injected in large quantities and the flow is recorded using high dose, high frame rate cinematography (CINE).
5. The C-arm is rotated through various angles and further cine runs are acquired until the cardiologist is satisfied that enough information has been collected.

In addition to the coronary angiography and angioplasty procedures studied in this thesis, the cath lab is capable of performing a great number of different operations, including: Electrophysiology studies, correction of congenital defects and pacemaker implants. An example of the types of images acquired for an angioplasty are shown in Figure 2.12.

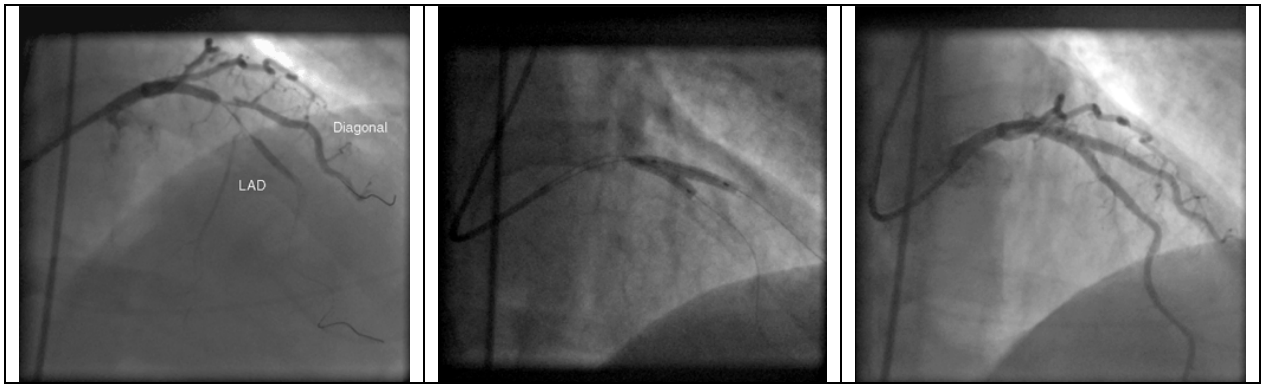

(a) (b) (c)

Figure 2.12. a) Acute narrowing in the Left Anterior Descending (LAD) and Diagonal coronary arteries identified via contrast agent injected into arteries. b) Inflated balloons (angioplasty) attempting to clear blocked arteries. c) Subsequent angiogram shows the blockages have been successfully cleared. Source: *British Medical Journal.*

2.5.2 The C-Arm System

The central piece in any cardiology lab is the C-arm system. This piece of equipment generates X-rays, acquires the images and supports the patient. Cardiology C-arm systems are almost invariably set up with the X-ray tube located under the patient table. The reason being that the backscatter from the entrance surface is much greater than the scatter radiating from

the exit surface. Therefore the effective dose to personnel in the room is much lower when the entrance surface is under the table where less sensitive organs are exposed and shielding is easier. The imaging chain is shown schematically in Figure 2.13 as well as radiochromic film placement used in this study.

The X-rays exit the tube and pass through the patient's posterior; they then exit the patient from their anterior and are detected by the image intensifier or flat panel detector. The cath lab used in this study is a Siemens Axiom ARTIS with a flat panel amorphous silicon detector. Because these systems are under-couch design it should be obvious that the patient's back will receive a far greater dose than their anterior. For this reason the radiochromic films used in this study are placed between the table and the patient's back.

In this chapter the following background information has been described: radiation and how it causes damage to human tissue, the outcomes of such damage, and the environment in which this study takes place. In the next chapter the characteristics of the radiochromic film used to measure skin dose is investigated.

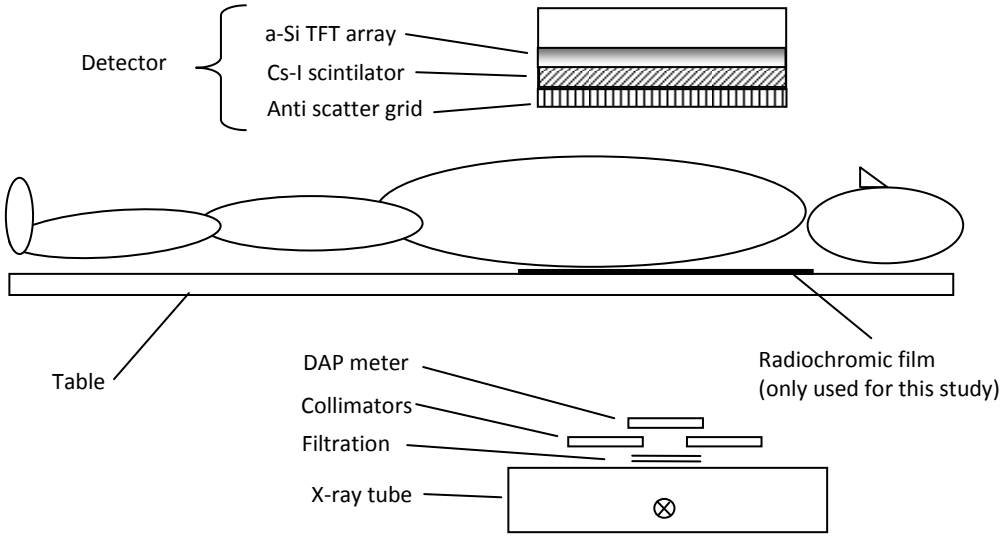

Figure 2.13. Components of the C-arm imaging chain.

3. Radiochromic Film Dosimetry

3.1 Radiochromic Film Overview

Films have a wide range of applications in diagnostic radiology, radiotherapy and radiation protection. They can be used as radiation detectors, for qualitative and quantitative dosimetry, as a display device and archival medium. The most widely used film has traditionally been radiographic film, which requires a film processor to make the latent image visible [35]. Recently, a new type of film, namely radiochromic film, has become more widely available.

Gafchromic® films are a type of radiochromic film developed at ISP corp (International Specialty Products, Wayne, NJ, USA). A radiochromic film consists of a layer of radiosensitive gel sandwiched between protective sheets. When the film is irradiated the gel will undergo polymerisation and produce a visible darkening. The amount of darkening is proportional to the dose delivered to the gel and is relatively unaffected by visible light. These properties offer greatly simplified handling over conventional radiographic films. Specific Gafchromic® film types also possess many other advantageous dosimetric properties, including one or more of the following: tissue equivalence, energy independence, high sensitivity or wide dose range and excellent 2D resolution [36-38]. The type of film can be chosen to meet particular needs.

Radiochromic reactions have been known for some time. Some of the earliest demonstrations of the effect go back to 1826 when Niepce [39] demonstrated "an unsaturated hydrocarbon polymeric mixture based on bitumen that cross links upon irradiation, leaving a light-scattering pattern" [36]. Around the late 1980's Dr David Lewis et al. demonstrated a type of film based on polydiacetylene that would become commercially known as Gafchromic® [40]. "The Gafchromic® reaction is a solid-state polymerisation, whereby the films turn deep blue proportionately to radiation dose, due to progressive 1,4-trans additions which lead to coloured polyconjugated, ladder-like polymer chains"[36] [40].

Despite having a number of advantages over other dosimetry systems, radiochromic films do have drawbacks. Many of them exhibit one or more of the following; energy dependence, local sheet non-uniformity, post exposure density changes and polarisation effects [37,38,41-44].

Over the past two decades the film has evolved through a number of different products including HD-810, MD-55 and the most recent EBT with dose sensitivities of 10-400 Gy, 2-100 Gy and 0.1-800 cGy, respectively [45]. The characteristics of radiotherapy Gafchromic® films MD-55 and EBT are well known and have been extensively investigated [36,44,46-50]. To be useful for diagnostic radiology applications requires greater sensitivity to low energies. There are now models of Gafchromic® film tailored more towards diagnostic needs such as the discontinued Gafchromic® XR-R and XR-T [42,43,51-55]. Its replacement, the XR-RV2 boasts an increased dose range and comes in large 14"x17" sheets.

The radiochromic film to be used for this study is the Gafchromic® XR-RV2 (Figure 3.2 & Figure 3.1). It has an opaque paper backing and a transparent yellow-dyed polyester covering to improve visual contrast and to reduce ultraviolet exposure of the radiosensitive dye. The active and surface layers are made up of low atomic number elements H, C, O, N (96.4% and 94% respectively) but also contain traces of lithium and chlorine. The proprietary high Z material present in this film is actually 4.5% barium mixed into the opaque polyester backing (personal communication with ISP). Presumably this is to aid in stopping power and increase photoelectron and scatter production. These factors give the XR-RV2 film far greater sensitivity to low energy at the expense of losing their tissue equivalence.

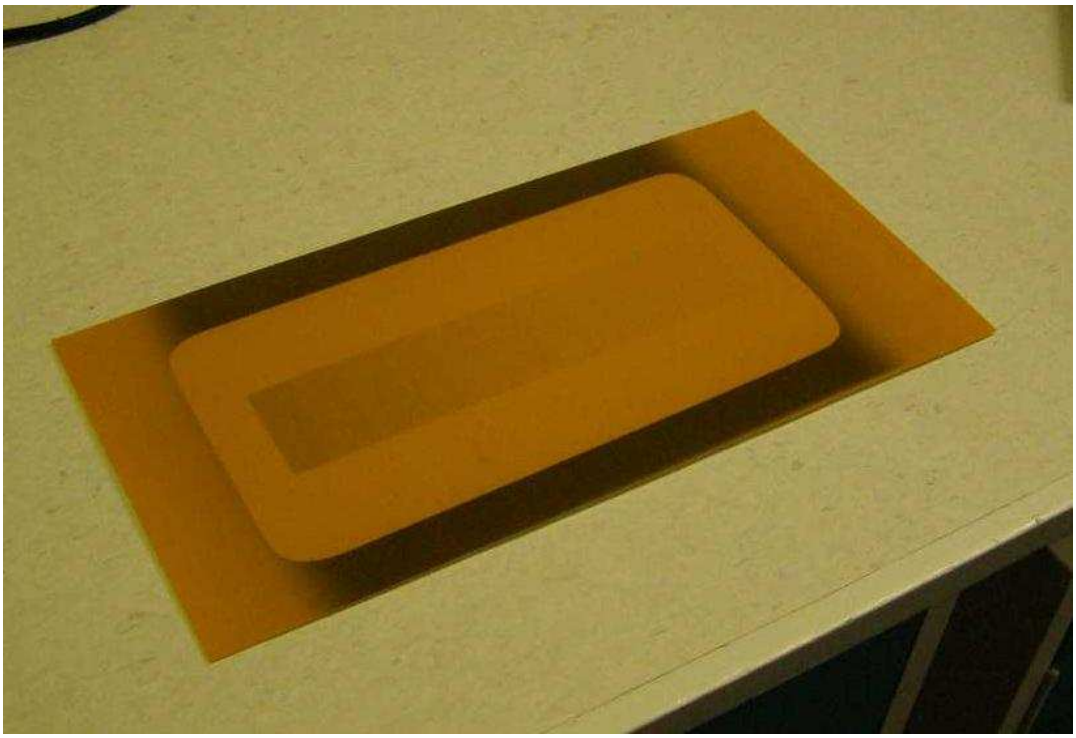

Figure 3.1. Photo of Gafchromic® XR-RV2 film exposed with a step wedge.

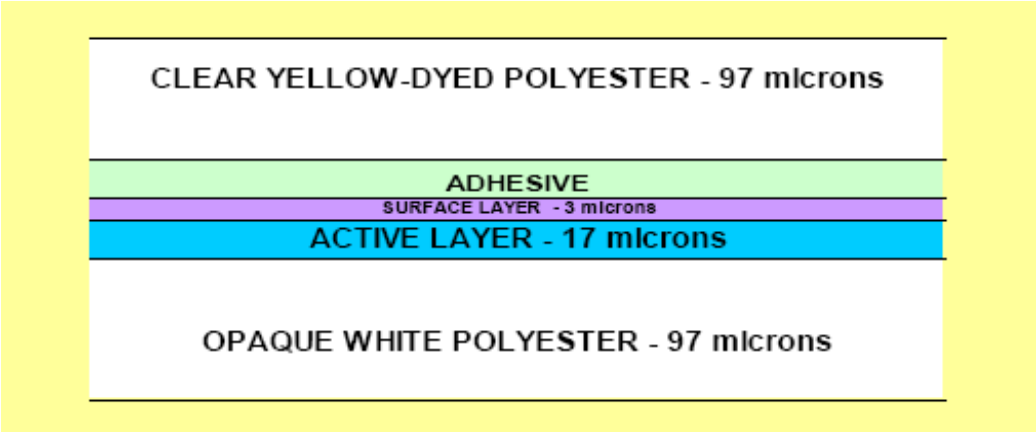

Figure 3.2 Structure of Gafchromic® XR-RV2 film.

3.2 Scanner Characterisation

Film dosimetry is a two part system consisting of both the film and some method of reading the film. It was decided to scan the films using a colour flat-bed document scanner as many authors have had great success with such scanners [50,56,57]. A good document scanner offers many advantages such as low cost, good stability, high precision and full 2D resolution. However each scanner has a unique response [42,55] and many have undesirable properties e.g. field non-uniformities, instability, uneven response etc, therefore the scanner should be chosen carefully. Two document scanners were used in this study. An HP Scanjet IIcx (Hewlett-Packard, Palo Alto, California, USA) and later an Epson Expression 10000 XL (Seiko Epson Corporation, Suwa, Nagano, Japan). The Expression 10000 XL has an A3 sized scanning bed and therefore would be used for patient film scanning. For comparison, the response was also measured on an X-Rite model 301 spot densitometer (X-Rite Incorporated, Grand Rapids, MI, USA).

Film digitisers such as Vidar® Scanners may also be used. The main issues with these types of scanners are the field non-uniformities and film bending during transportation through the reader [58,59] as well as accessibility. The light source in Vidar® and flatbed scanners is a long fluorescent or cold cathode lamp. In the case of the Vidar scanner a light diffusion plate is also used to create a diffuse source. Since the tube is a finite length the amount of off axis scatter produced by the film and diffuser will be greater at the centre of the CCD than the edges. This effect is shown in Figure 3.3. For a diffuse source the scattering effect is accentuated as the source is moved further from the CCD. In a flatbed scanner the source is usually located closer to the film therefore the effect is weaker. On the flatbed scanners tested for this study the effect was not observed. The film is passed through the digitiser between a series of rollers. In the older Vidar® models the film is unsupported for the final part of the scan causing it to move slightly with respect to the CCD creating a band in the resulting image.

The digitiser available in the department is an older Diagnostic Pro model which shares some of the known deficiencies in scanning radiochromic film as the Vidar VXR-16 mentioned in previous papers. The digitiser was tested and found to exhibit significant field non-uniformity however banding was not able to be confirmed.

While these are relatively easy to correct for, a flat bed scanner was chosen for practicality and accessibility along with positive results from other authors with document scanners. When testing scanner and film characteristics a standard 24 bit depth RGB and 150 dots per inch (DPI) resolution were used unless otherwise stated.

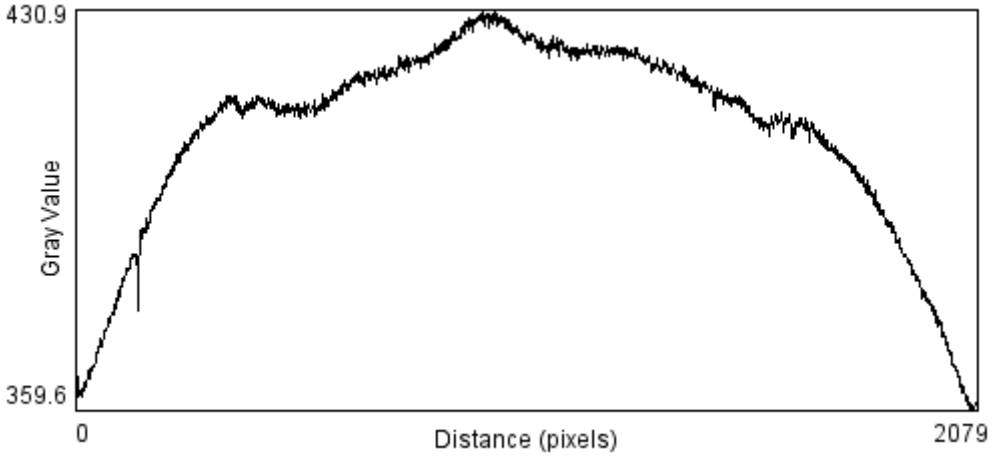

Figure 3.3. Profile across Unexposed EBT film on a Vidar® Diagnostic Pro plus®.

3.2.1 Scanner warm up time

A scanner's response will change as it warms up. In particular the light source will increase in brightness and the electronics may take some time to reach equilibrium. To allow the electronic components to reach thermal equilibrium the scanner should always be turned on at least 30 minutes prior to scanning. To test the warm up response a 5 x 5 cm square of film was scanned in rapid succession at a fixed location on the HP Scanjet.

After four scans the response had stabilised to within one pixel value of the long term stable response as shown in Figure 3.4. Therefore as part of our scanning protocol it was decided that four warm-up scans should be performed before taking any measurements.

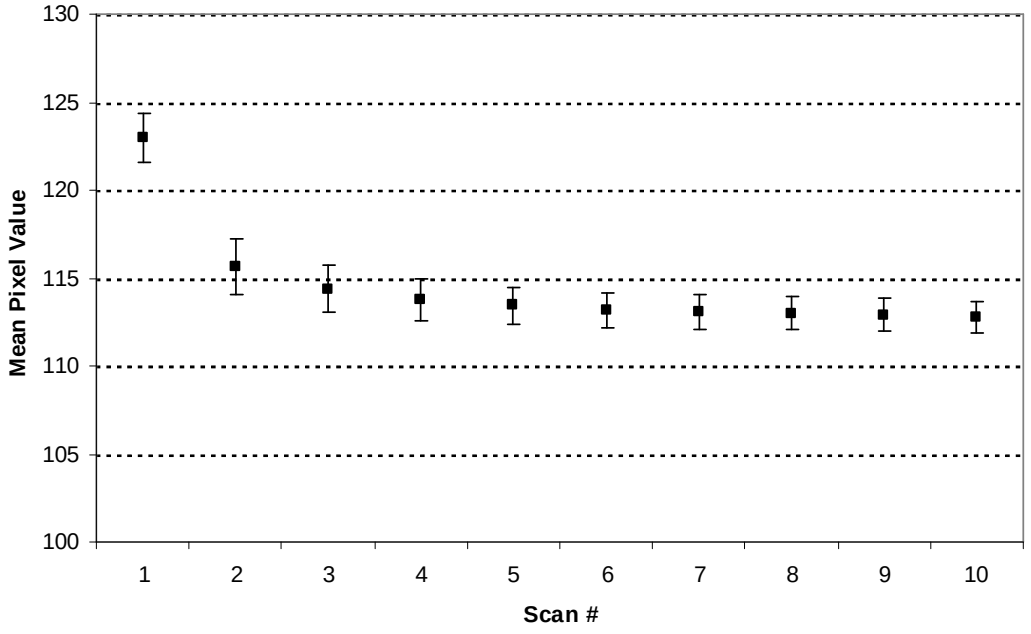

Figure 3.4. Scanner response changes as a function of warm-up scans on an HP Scanjet.

3.2.2 Scanner non-uniformities

Scanner non-uniformities can pose a significant problem to scanned images necessitating the removal of the background. For example the standard deviation of pixel values over a flat field image of unexposed film was 6.6 with a range of 43 when scanned on the HP Scanjet as illustrated in the flat field image shown in Figure 3.5. The very edges of scanned images tend to have erroneous values and should be ignored.

Several background masks were investigated including; white paper, various other paper colours and a sheet of unexposed film. White paper was deemed inappropriate due to saturation of pixels. Although many backgrounds could be used it was concluded that a sheet of film was the most relevant background. In order to separate film non-uniformities from scanner non-uniformities, three background images were acquired with three different sheets of film, each rotated at a different angle. A 3x3 pixel median filter was used on each image to remove spurious noise. These images were then averaged to form a final background image.

In scanning film one cannot easily separate the scanner from the film non-uniformities. This is where the double exposure technique can be useful. It is discussed in detail by Zhu et al [60] but to summarise, it involves uniformly exposing each film then scanning before and after actual irradiation. This way the "background" image includes both the scanner and film non-uniformities. The obvious downside to this method is the time it requires and the additional complication of using partially exposed films. It was decided not to use the double exposure technique since the increased accuracy (less than 5% based on ISP specifications) did not warrant the extra time and difficulty in uniformly irradiating large films.

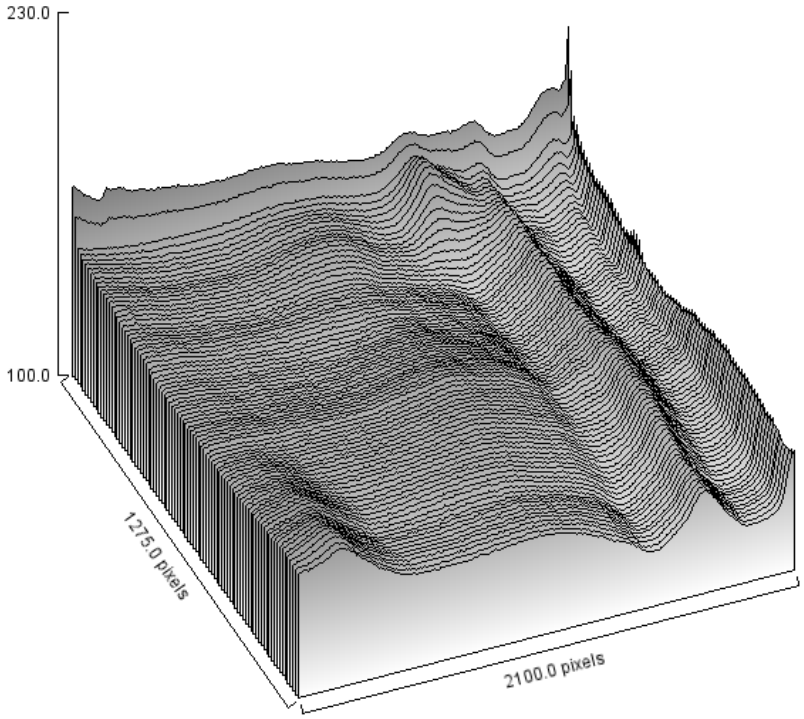

Figure 3.5. A scan of unexposed film showing the magnitude of variation over the scanned area on the HP Scanjet.

To correct the image for non-uniformities the following approach was used:

$$P_{corrected}(i,j) = \left(\frac{P(i,j)}{B(i,j)} \right) \cdot \overline{B(i,j)}, \qquad (3.1)$$

where $P(i,j)$ is the original image, $B(i,j)$ is the scanner background image and $\overline{B(i,j)}$ is the global pixel mean of the background image.

The results were analysed subjectively using a 3D surface plot. To do this a known image was created (Figure 3.6a) and scanner noise from one film scan was added (Figure 3.6b). The background correction was then applied according to Eq.(3.1) to produce the final corrected image shown in Figure 3.7. The same technique was then applied to a clinically exposed film as shown in Figure 3.8 & Figure 3.9. It can be seen in the real example that although the correction is not perfect, it is still a large improvement.

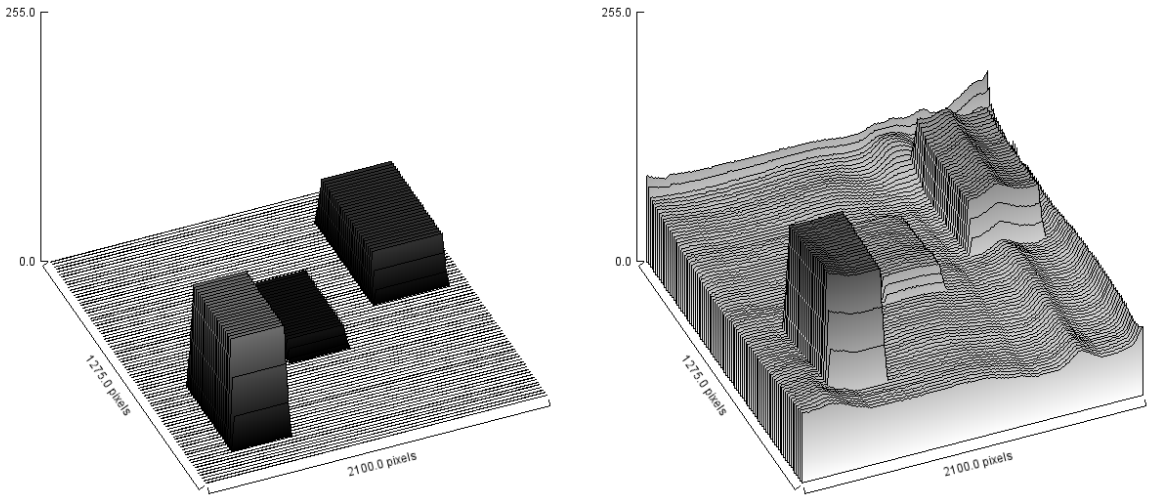

(a) (b)

Figure 3.6 a) Original image. b) Image with scanner noise added.

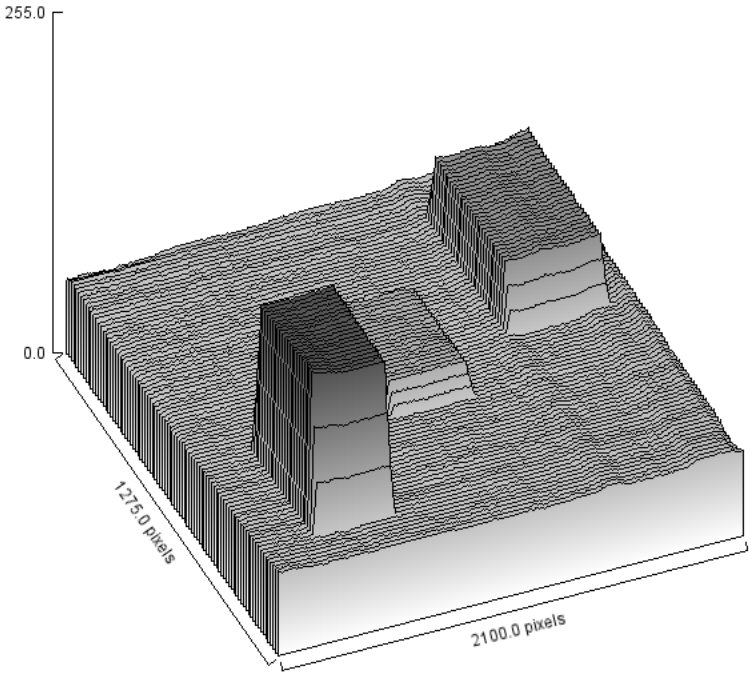

Figure 3.7 Corrected image showing significant improvement.

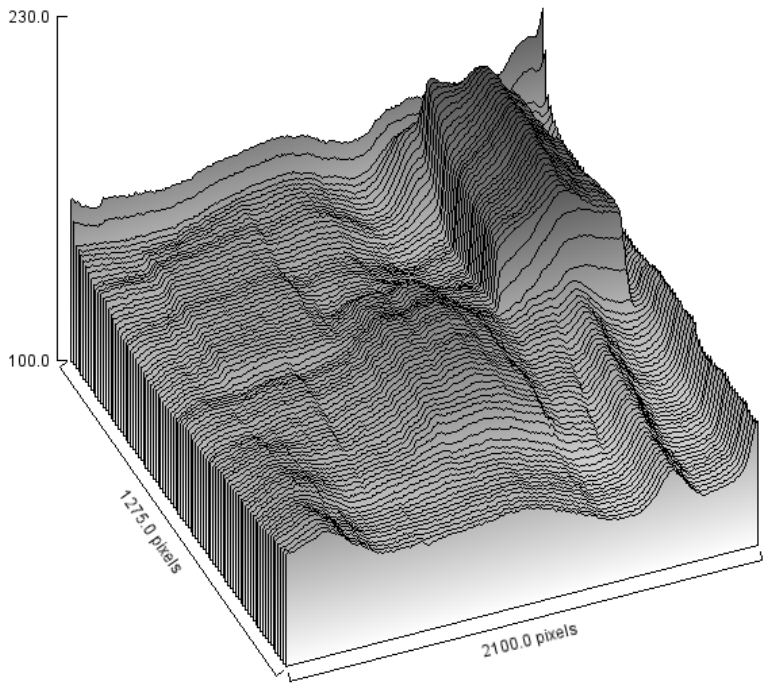

Figure 3.8. A clinically exposed film with several fields scanned on an HP Scanjet. It can be seen that the scanner non-uniformities are significant compared to the data.

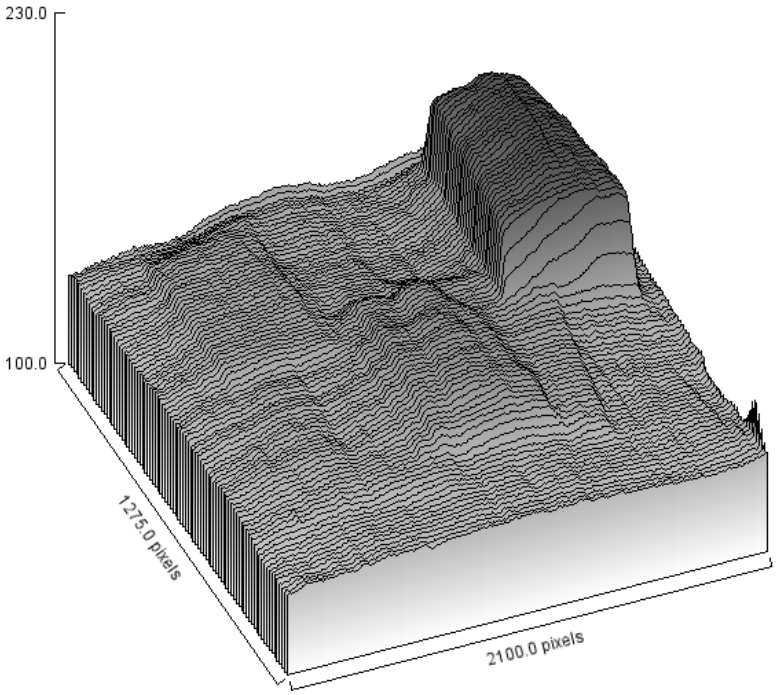

Figure 3.9. The same film sample corrected for scanner background non-uniformity.

3.3 Gafchromic® XR-RV2 Characterisation

3.3.1 Dose response function

To test the dose response of this film a set of nineteen, 5 x 5 cm squares were exposed to doses from 1 – 2000 cGy at 96 kVp using a high frequency Philips Optimus 50 radiographic unit with light beam diaphragm (LBD) removed as shown in Figure 3.10. This machine was tested to have an HVL of 3.27 mmAl at 96 kVp and an estimated total filtration of 2.35mm Al with the LBD removed. The coefficient's of linearity and variation for this machine were 1.7 % and 0.4 %, respectively. The Unfors Xi (Unfors Instruments, Billdal, Sweden) meter was used to perform dose measurements. This meter was factory calibrated. Dose measurements were made in air in terms of air kerma [$(K_{air})^{air}$] since the dosimeter was calibrated in this manner. Films were exposed in stacks of three as suggested in the manufacturers calibration instructions. The impact of this time saving method was investigated and revealed <3% difference between the top and bottom of the film stack. This was corrected for in this study.

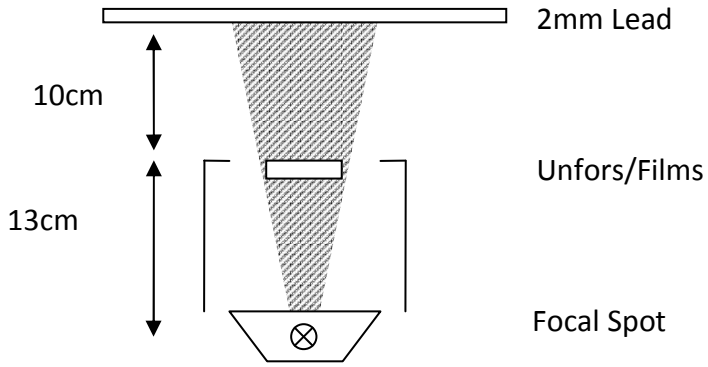

Figure 3.10 Test setup for film exposures.

Films were scanned on an EPSON Expression 10000XL in contrast to the previous scanner investigations which were carried out on the HP Scanjet. The reason for this being that the Epson Expression scanner was not purchased until part way through this study. All calibration squares were scanned simultaneously in a central uniform section of the scanner bed. The films were then randomly rearranged and scanned again. This was repeated and the three scan sets were averaged to reduce errors. Scanner non-uniformity correction was not made since the uniformity of this particular scanner was excellent. In fact, the uniformity of the scan area was measured to be within 0.6% to 1σ. No attempt was made to correct for any film non-uniformities which may be present. A 3x3 pixel median filter was then applied to all scans to remove spurious pixels. Pixel measurements were performed in a central 10 x 10 mm region of interest (ROI). The net pixel value was calculated as

$$PV_{net} = (255\text{-}PV)\text{-}(255\text{-}PV_{unexposed}),$$

where the background pixel value was found by including unexposed films in the scanning of the calibration squares.

Net pixel values were calculated and plotted against kerma. Curve fitting was performed using Curve Expert (Hixson, TN, USA). It is well known that Gafchromic® film response is wavelength dependent [44,56,61] therefore RGB colour channel responses were also investigated. Image manipulation was performed using the free image processing software ImageJ (National Institutes of Health, Maryland, USA) [62].

Figure 3.11 shows the dose response of the film measured on the Epson Expression in RGB mode. A fit was found using a saturation growth-rate model of the form:

$$\text{net PV} = \frac{a \cdot K_{air}}{b + K_{air}},$$

where a and b are fitting parameters.

This fit was chosen because as the name suggests, it describes a physical situation and it is also a simple two parameter equation. Other more complex fits provided only marginal improvements.

It can be seen that the film is sensitive to doses as low as 10 mGy and up to at least 10 Gy. Although the primary channel for dosimetry is the red channel, green and blue channels for the same scans are also shown. ISP mentions that the film can easily handle doses beyond 50 Gy using the green and blue colour channels. This could not be verified as the dose was beyond the scope of our investigation however the green channel response is of a similar shape as the red channel. Very little sensitivity was observed in the blue channel even at 20 Gy.

For comparison, the dose response on a densitometer is show in Figure 3.12. One can immediately see that the shape of the response is slightly different to that of the document scanner (Figure 3.11). The document scanner shows good sensitivity to low doses while the densitometer does not respond appreciably until around 100 mGy compared to around 10 mGy for the document scanner. In the 100 – 4000 mGy region the document scanner shows approximately logarithmic response. Beyond that the scanner begins to lose sensitivity and plateaus, while the densitometer continues it's logarithmic response right up to the dose limit of this investigation (20 Gy).

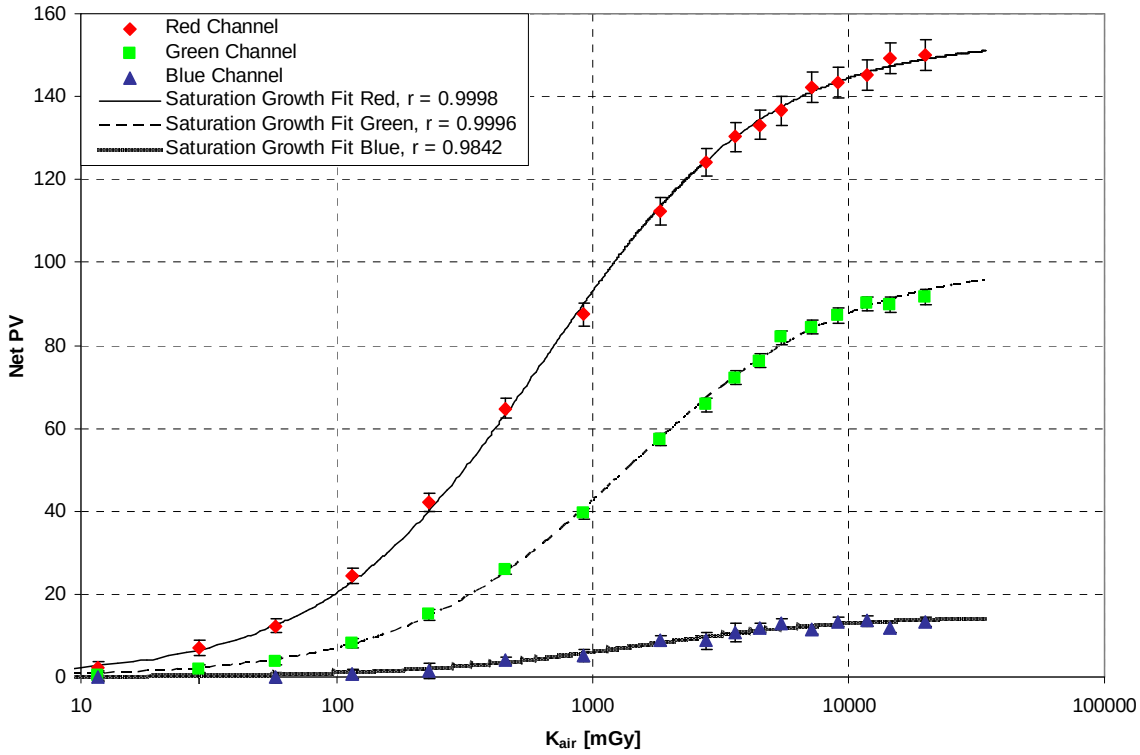

Figure 3.11. Dose response of Gafchromic® XR-RV2 measured on an Epson Expression 10000XL. RGB channels fitted using saturation growth-rate models.

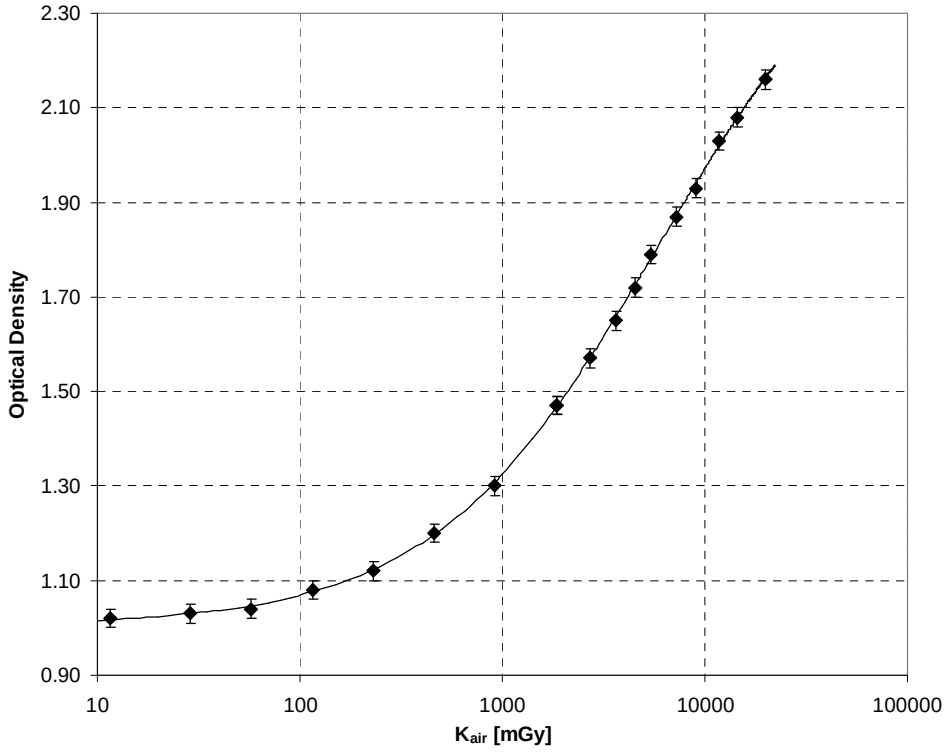

Figure 3.12. Dose response of Gafchromic® XR-RV2 measured on an X-Rite spot densitometer.

3.3.2 Energy dependence

Four energy data sets were generated by exposing films to 60, 73, 96, and 125 kVp over a range of 4 to 270 cGy using the same method as described for the dose response, with the exception that stacking was not used. The dosimeter was calibrated by the National Radiation Laboratory (Christchurch, NZ) and found to be within 2% energy variation over 50 to 150 kVp. A dose response curve was generated for each energy (not shown). The absolute and relative variation in net pixel values was calculated as a function of dose, by fitting a saturation growth-rate curve to each energy data set, and comparing each of the curves to find the variation with energy.

Figure 3.13 shows the variation in dose response between 60 and 125 kVp. The plots were obtained by fitting a saturation growth-rate curve to each energy set and using interpolated data for analysis. Both the absolute variation and relative variation are shown. The relative variation is quite high at doses below 1 Gy. This is in part due to division by a small number as the absolute variation in pixel values is quite small. The relative variation decreases with dose approximately exponentially to steady out at ~6.5% at 5 Gy. An increased response was observed for increasing energies up to 125 kVp (56 keV) while the greatest variation is response occurred at the lower energies.

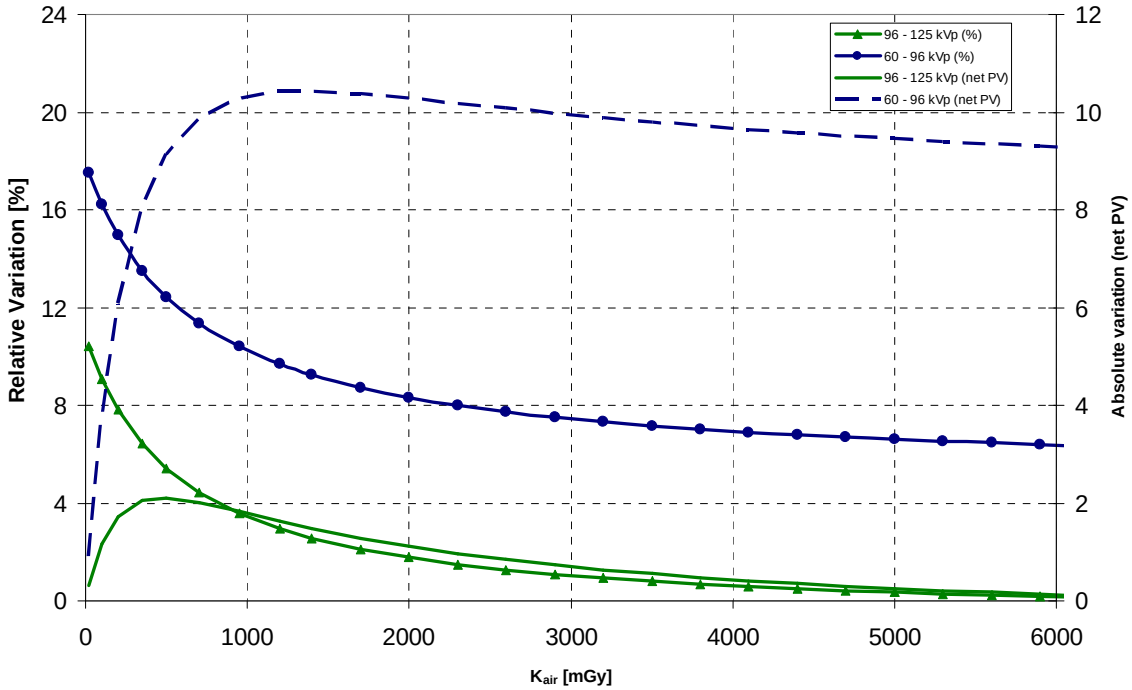

Figure 3.13. Variations in pixel value as a function of dose between 60-125 kVp.

3.3.3 Post-exposure growth

While the initial polymerisation reaction takes place within a few milliseconds [61], it has been known for some time that the OD of Gafchromic® film continues to increases on a much larger time scale [63]. It is also well known that ambient light has some effect on this colouration [64]. To investigate this effect, two squares of 5 x 5 cm film were exposed to 50 cGy air kerma. One film was left under typical office fluorescent lighting and the other was stored in a light tight container. The films were then scanned on an HP Scanjet in a reproducible manner at various times post exposure for a period of 75 days.

Figure 3.14 shows the post exposure growth of two films exposed side by side. One film was kept in a dark environment (dark) the other was kept under standard fluorescent office lighting (light). The dark set was adjusted by approximately 1.8 pixel values so that both sets measured the same pixel value when the films were first scanned. Two effects were observed. Firstly there is a definite exposure growth in both films, which is approximately logarithmic. Secondly the effect is more pronounced for films exposed to ambient light. Films left exposed to ambient light continue to darken for some time post irradiation, whereas films stored away from light sources seem to stabilise after ~24 hr. Table 3-I shows film density changes at various times of interest based on the logarithmic fit. It can be seen that there is significant exposure growth within the first 24 hr for films left under ambient light.

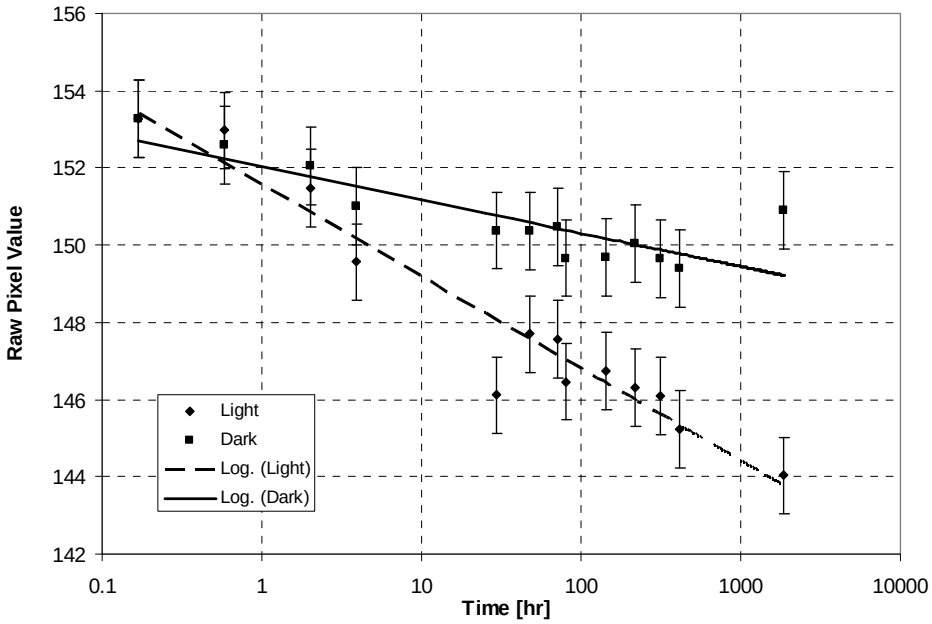

Figure 3.14. Plot showing exposure growth with time over a period of ~75 days with logarithm fits.

Table 3-I. Exposure growth at certain times post exposure

Time	*Light* %	*Dark* %
First 8hrs	3.8	2.1
First 24hrs	5.0	2.6
Subsequent 24hrs	0.8	0.4
Subsequent 72hrs	0.8	0.4
0-78 days	10.1	4.1

3.3.4 Polarisation effects

Radiochromic films are often subject to polarisation effects due to the multiple layers of film and the crystalline structure of the dye [44,65]. Polarisation can have a dramatic effect on film measurements making film orientation a critical parameter. This was investigated with an X-Rite model 301 spot densitometer and an additional polarising filter to improve the sensitivity of the measurements. The polariser was a BVO 32 film (Boulder Vision Optik, Boulder, Colorado, USA). The polariser was placed over the densitometer light source in order to produce a polarised source. The film was rotated through 360° in 30° increments and tested with opaque side facing towards and away from the light source

The magnitude of polarisation was found to be proportional to the absorbed dose in the film as shown in Figure 3.15. It is strongest for higher doses and reduces to negligible amount for unexposed film. This indicates that the polymerised active layer is the principal polariser. With no polarising filter in place, polarisation effects were noticed with the opaque side facing away from the light source, however no effect was observed in the opposite orientation with the opaque side facing the source. The introduction of a polarising filter accentuated the effect with the opaque side facing away from the light source and no significant effect was noticed in the opposite orientation. This would indicate that the active layer, and possibly the transparent polyester layer have polarising properties while the opaque layer acts to scatter the light in random planes of oscillation and depolarise the light.

In order to investigate the polarisation of the two polyester layers the suggestions of Klassen et al. [44] were followed. First the film was soaked in water for three days until the yellow polyester layer was able to be peeled from the opaque layer and gel. The gel appeared a bluish-grey colour. Next the gel was wiped from the opaque layer using water and a fine cloth while the adhesive required isopropyl alcohol to remove from the yellow polyester. When studied using a spot densitometer with a polarising filter neither the opaque nor the yellow layer produced any noticeable polarisation. This confirms that the gel is essentially the sole polariser in the film.

Next a film was rotated and scanned in the HP Scanjet with the results shown in Figure 3.16. Some small polarisation effect can be seen by the two peaks and troughs though the effect is much weaker than with the spot densitometer. This shows however that polarisation effects can be seen in document scanner and therefore one should pay particular attention to film orientation during scanning.

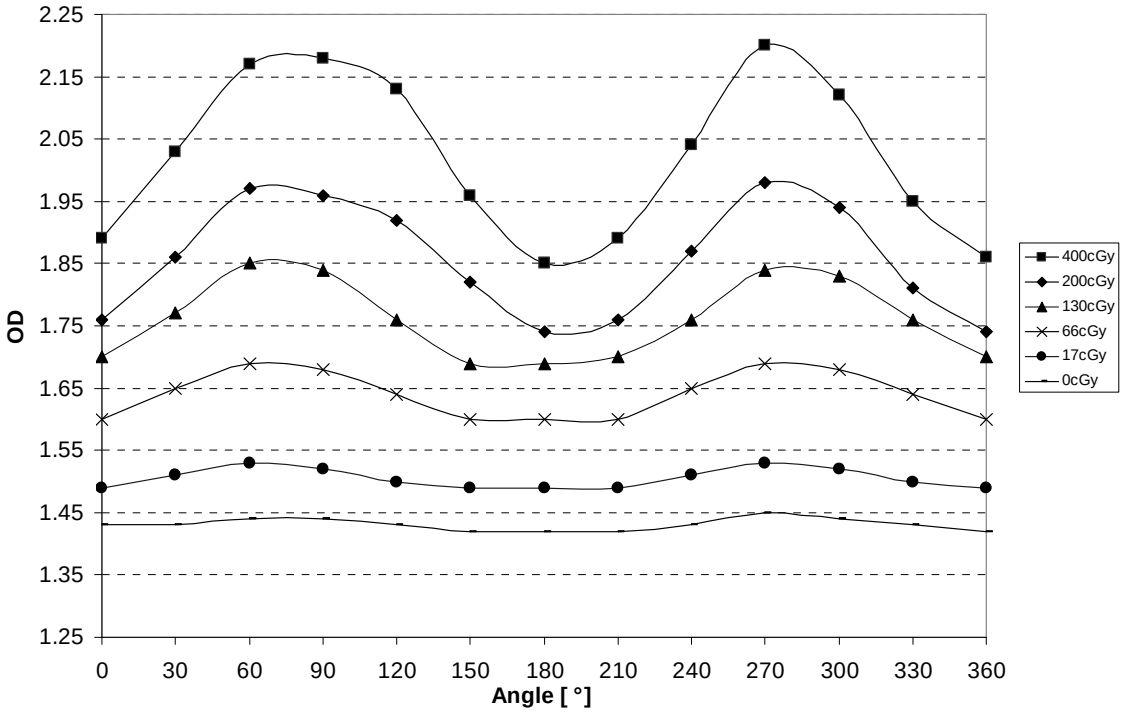

Figure 3.15. OD variation as the film orientation is rotated though 360° on a spot densitometer.

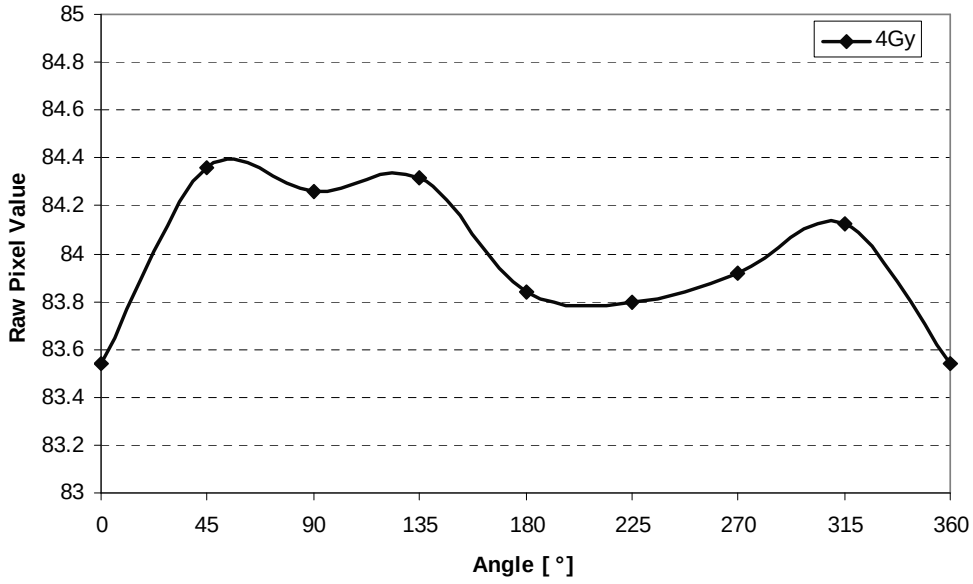

Figure 3.16. Pixel value variations as the film is rotated thought 360° in an HP Scanjet IIcx 24 bit scanner.

3.3.5 Film non-uniformities

This effect could not be investigated owing film and time constraints. It was decided to use the manufacturers specifications of < 5%.

3.4 Scanning Protocol

As a result of the investigations carried out, a scanning protocol was developed to minimise uncertainties whilst remaining time efficient and practical to use on an ongoing basis. Note that this protocol is valid only for the scanners tested in this study. Some scanners may have more significant variability between scans and require multiple scans to average. The protocol for scanning films follows in Figure 3.17:

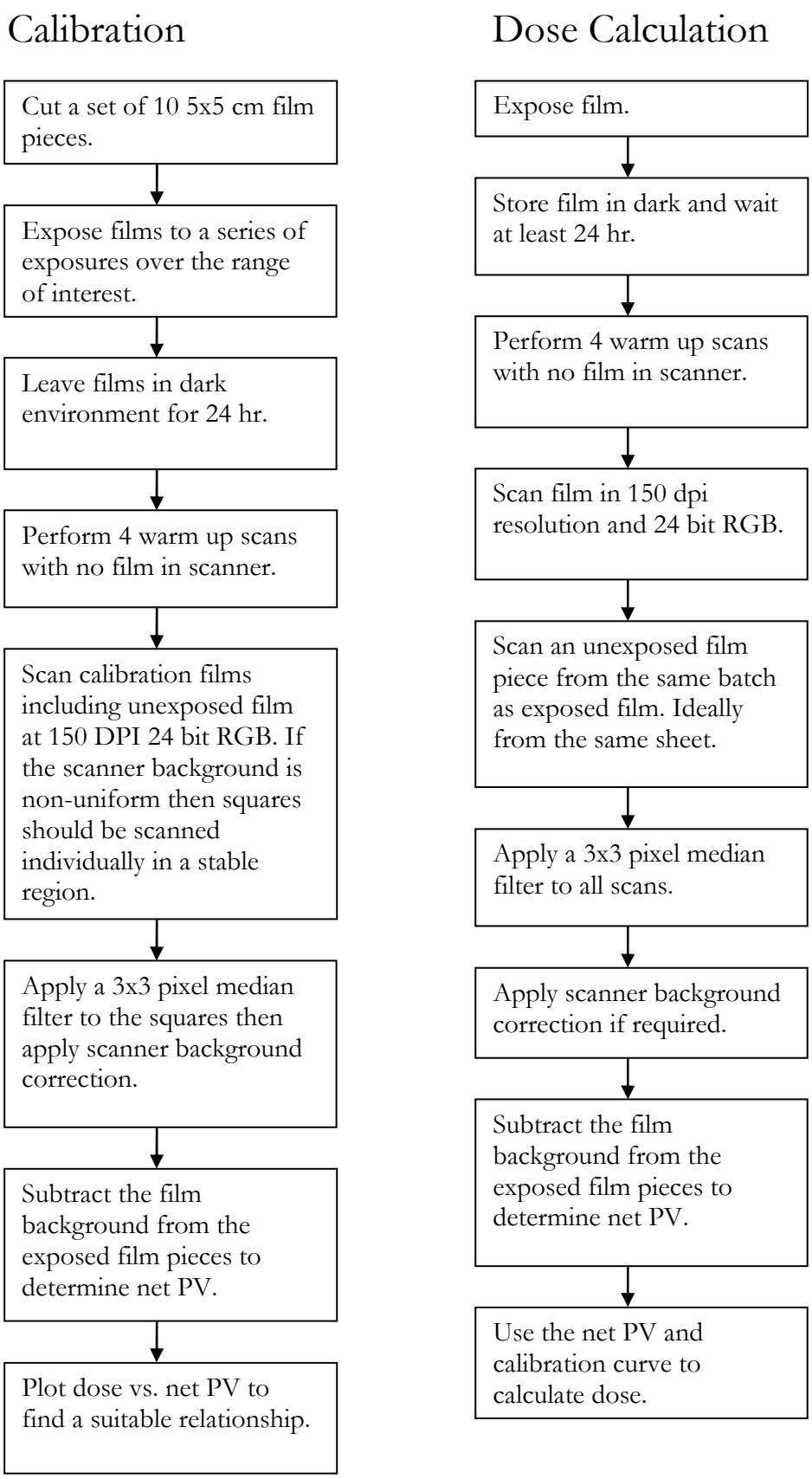

Figure 3.17. Protocol developed for creating a calibration set and for scanning films.

3.5 Uncertainties

In a study with many sources of error, a detailed uncertainty analysis is useful and can help determine the greatest sources of error. A Gaussian propagation of errors (without cross correlation terms) approach was used since this has been successfully demonstrated by previous authors for similar experiments [55]. The variance in a measured dose is given by:

$$\sigma_D^2 = \sum_i \left(\frac{\partial D}{\partial x_i} \right)^2 \cdot \sigma_{xi}^2 ,$$

where i is the number of parameters (x) in the dose equation (D) with each parameter having a variance of σ_{xi}^2.

It is then possible to separate the uncertainties into those associated with the fitting process and those associated with experimental uncertainties.

Therefore, given a dose response of

$$D = \frac{ax}{b+x} ,$$

where x is dose, the Gaussian propagation yields:

$$\sigma_D{}^2 = \left(\frac{\partial D}{\partial a} \right)^2 \sigma_a^2 + \left(\frac{\partial D}{\partial b} \right)^2 \sigma_b^2 + \left(\frac{\partial D}{\partial x} \right)^2 \sigma_x^2 ,$$

$$\sigma_D{}^2 = \left(\frac{x}{b+x} \right)^2 \sigma_a^2 + \left(-\frac{ax}{(b+x)^2} \right)^2 \sigma_b^2 + \left(\frac{ab}{(b+x)^2} \right)^2 \sigma_x^2 .$$

This equation can then be split into components based on the nature of each σ. Therefore the uncertainties associated with the fitting procedure are:

$$\sigma_{fit}(\%) = \frac{\sqrt{\left(\frac{x}{b+x} \right)^2 \sigma_a^2 + \left(\frac{ax}{(b+x)^2} \right)^2 \sigma_b^2}}{\frac{ax}{b+x}} 100 ,$$

$$= \sqrt{\left(\frac{x}{b+x}\frac{b+x}{ax}\right)^2 \sigma_a^2 + \left(\frac{ax}{(b+x)^2}\frac{b+x}{ax}\right)^2 \sigma_b^2} \times 100\,,$$

$$= \sqrt{\left(\frac{\sigma_a}{a}\right)^2 + \left(\frac{\sigma_b}{b+x}\right)^2} \times 100\,.$$

Likewise the uncertainties associated with measurement of pixel values are:

$$\sigma_{experimental}(\%) = \frac{\sqrt{\left(\frac{ab}{(b+x)^2}\right)^2 \sigma_x^2}}{\frac{ax}{b+x}} \times 100,$$

$$= \sqrt{\left(\frac{b}{x\cdot(b+x)}\right)^2} \sigma_x \times 100.$$

The uncertainty in σ_x is itself a combination of many uncertainties which can be summed in quadrature:

$$\sigma_x = \sqrt{\sigma_{\text{scanner}}^2 + \sigma_{\text{film nonuniformity}}^2 + \sigma_{\text{energy dependance}}^2}\,.$$

There are other sources of uncertainty such as scanner warm up time, post exposure density growth, and polarisation effects. However these are minimised by following the scanning protocol presented earlier so that they become negligible by comparison. The energy dependence was estimated from section 3.3.2. It was found that beam energy varied by a maximum of 20 kVp during any single procedure. Therefore as an estimate, the variation between the 73 and 96 kVp data sets was used to model the energy dependence as a function of dose.

Figure 3.18 shows the uncertainty associated with the fitting procedure. There was approximately 3% uncertainty across most of the dose range of interest, and increasing rapidly above 3 Gy. Uncertainties are expressed to 1σ unless otherwise stated.

Figure 3.19 shows the combined fit and experimental uncertainties (Gaussian Propagation) including the dose response of the film for reference. It can be seen that the fit uncertainty is negligible compared to the experimental contribution. As expected there is an asymptotic increase in relative uncertainty as the dose approaches zero. The relative uncertainties are lowest between approximately 500-1500 mGy then begin to rise as the dose increases. Theoretically the lowest achievable uncertainty was 9.5% (1σ).

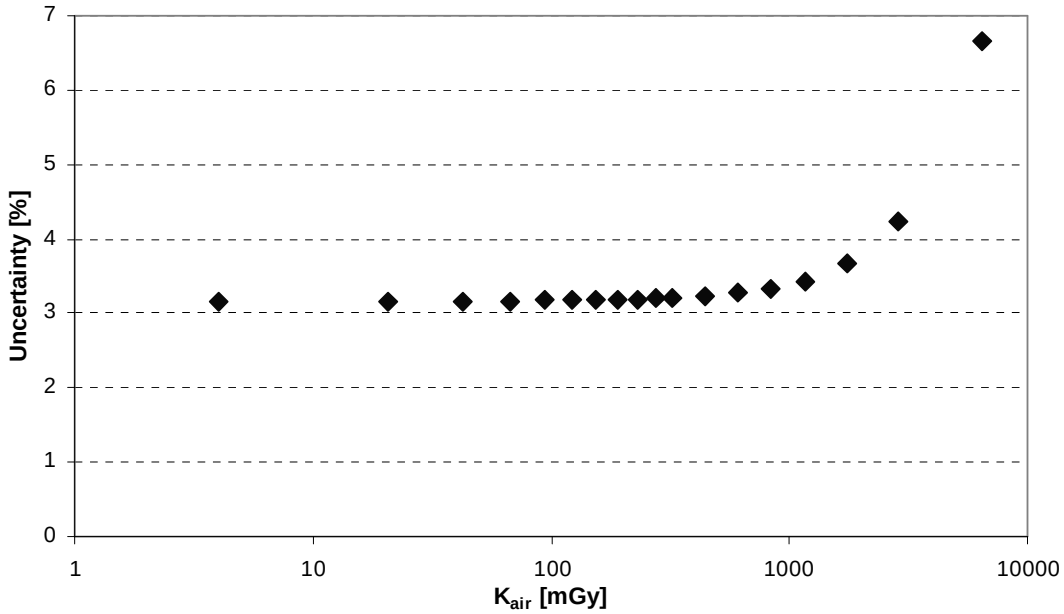

Figure 3.18. Uncertainty arising from fitting procedure.

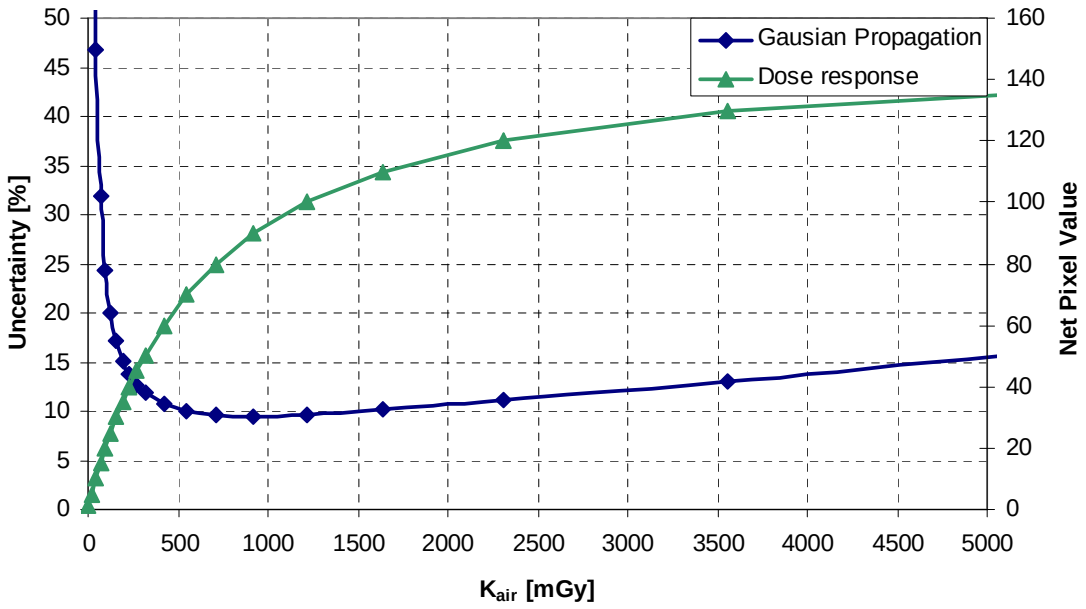

Figure 3.19. Combined uncertainty from fitting process and measuring process by a Gaussian propagation approach. Dose response is also shown for reference.

3.5.1 Verification

In order to verify the uncertainty model several film squares from an assortment of film sheets were exposed to a range of doses between 20 and 2000 mGy. Films were stored in a dark environment and left for 48 hours before scanning on the Epson Expression scanner. Net pixel value was calculated following the protocol detailed previously. The deviation

between measurements and the fit model is shown in Figure 3.20. It can be seen that all measurements lie within 14% of the model and two thirds lie within 10%. Thus the magnitude of predicted uncertainties appears to closely match the observed uncertainties. It would be unreliable to make any certain conclusions based on such a small sample size. However an observation can be made that the minimum uncertainties occur in the 500 – 1000 mGy region, and increase outside this region, similar to Figure 3.19.

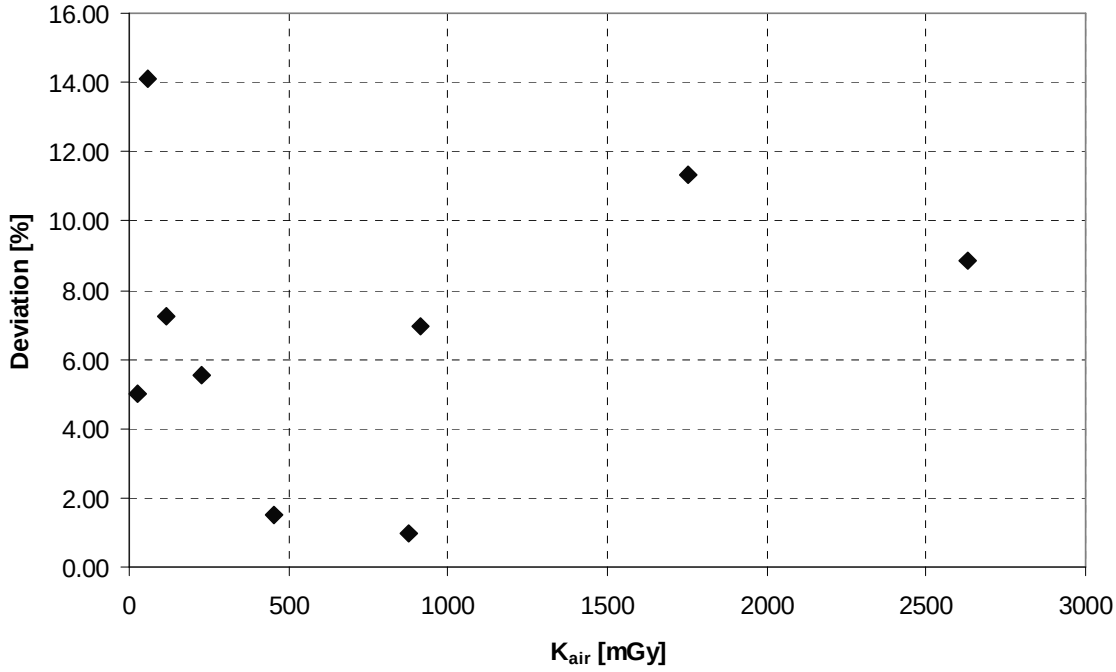

Figure 3.20. Deviation between measurements and fit model.

3.6 Discussion

3.6.1 Energy Dependence

The energy dependence of the film in the diagnostic rage of energies is much greater than that of conventional radiotherapy Gafchromic® films. This is due to the added high atomic number components used to boost the films sensitivity to low energy photons. This energy dependence has implications for the dosimetry of fluoroscopy beams to be conducted later in this work. In a typical fluoroscopic system the beam energy is automatically modulated to achieve sufficient patient penetration based on patient attenuation. As a consequence any single film may be exposed to a range of energies typically varying by around 20 kVp. This gives rise to an uncertainty that cannot be avoided and makes up a large portion of the uncertainty shown in Figure 3.19.

3.6.2 Polarisation

The response of the film to polarised light deserves special attention as it is a significant and interesting effect. It is clear that one must be careful to use consistent orientation between calibration and scanning of films. The angular dependence will vary between scanners since nearly all light sources are polarised to some extent. Looking at Figure 3.15 it becomes evident that polarisation could be used to improve the sensitivity of measurements. For example, measurements made at 0 and 180° show much smaller changes in optical density when compared to measurements made at 90 and 270°. In practice, the difference between an unexposed film and a film exposed to 4.7 Gy was 0.75 OD and 0.63 OD with and without a polarising filter respectively. This equates to an 18% increase in sensitivity.

3.6.3 Scanner Characteristics and Dose Response

From Figure 3.11 it can be seen that the scanned pixel values begin to plateau at higher kerma. However, recall that the OD when measured on a spot densitometer continued to increase logarithmically in this region (Figure 3.12). This indicate that is may not be the film which is saturating but in fact the scanner. In order to fully test the limits of scanner response, a step wedge was exposed onto X-Omat mammography film and scanned with the results shown in Figure 3.21. Upon reaching an OD of 1.6 all colour channels had converged to a single value indicating that the scanner's CCDs had reached their lower limit. That is, despite an increase in optical density, no change is registered in pixel values. Figure 3.22 shows the 96 kVp calibration data set expressed in raw pixel values. Two things become apparent:

- The threshold pixel value for the X-Omat mammography film is not the same as for the Gafchromic® film owing to different chromatic absorption. All channels approach a pixel value of ~20 for the mammography film, whereas the blue channel for the Gafchromic® film reaches a minimum of ~10.

- All the colour channels for the Gafchromic® film are levelling out to a value close to that of the mammography film.

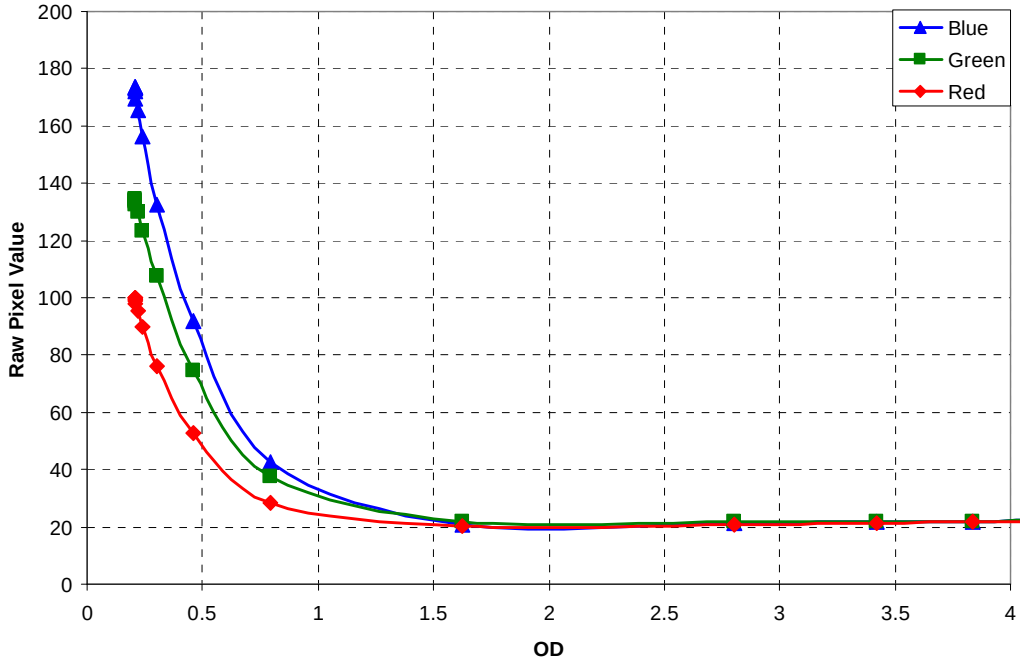

Figure 3.21. Response of X-Omat film when scanned on Epson Expression XL

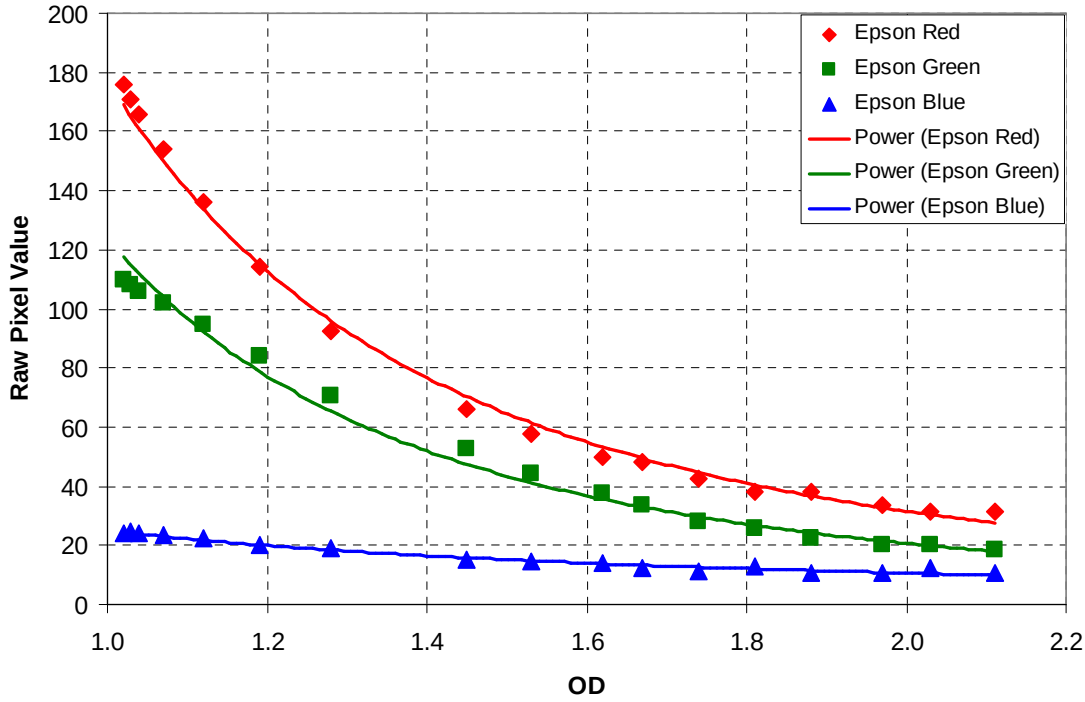

Figure 3.22. Calibration data set expressed in terms of raw pixel values.

A raw pixel value of 10 – 20 indicates somewhat of a noise floor for the CCDs of this scanner. ISP mention that the film can be used up to and beyond 50 Gy by using the green and blue channels of the document scanner [66]. From what has been discussed in this section it seems highly unlikely that this would be the case for the scanners used in this study. For

example the blue channel (Figure 3.22) for an unexposed film begins with a pixel value of ~25 which is already very close to the noise floor and as such the data is noticeably noisy. Like wise, the green channel drops to pixel values of ~20 above 10 Gy despite having greater sensitivity than the blue channel. Thus scanner sensitivity is the limiting factor for dosimetry using this flat bed document scanner for doses greater than 10 Gy. It is not that the film has saturated, as it has been shown that the OD continues to increase, but the scanner which is at its limit.

The effect of bit depth on sensitivity was also investigated. Bit depth and it's relation to dynamic range is often poorly understood. The point will be made that dynamic range and bit depth are entirely separate quantities. The dynamic range of a scanner represents the range of intensities from maximum to minimum that can be measured and this is primarily limited by the largest and smallest signal that the CCD can measure. As absorption from the scanned media increases the signal reaching the CCD becomes weaker until the electrical noise in the system completely masks the signal. At this point any further darkening in the media will not change the output signal from the CCD.

Once the analog signal has been output from the CCD it will eventually go through an analog to digital (A/D) converter where it will be converted to a discrete digital value. With the availability of cheap A/D converters most modern scanners can achieve 48 bit depths (16 bits per channel). Therefore bit depth alone is a very poor indicator of scanner quality and performance. The real question is: is a 48 bit scan superior to a 24 bit scan? And the answer depends on the noise present in the system.

The smallest measurable signal is limited by the electrical noise in the scanner, that is, one cannot distinguish light levels which give a lower signal than the noise of the scanner. For a 24 bit image (8 bits per channel) the range of values will lie somewhere between 0 and 255. If the scanner noise on that same scale was less than 1 then more information could be gained by using a greater bit depth to give finer sampling. If the noise was greater than 1 then a 24 bit scan would be more than sufficient.

To demonstrate this point a data set of Gaussian noise was simulated and the data binned according to various bit depths. Figure 3.23a shows the histograms of a noisy data set for different bit depths where the sample size was n = 1600. If no noise were present in the system the histogram would be a single bar. From the 8 bit histogram a range of values can be seen and the distribution appears bell shaped. The fact that there is more than one bar in the histogram indicates that the extra bars represent the noise. As the bit depth is increased the histogram simply becomes a more refined Gaussian shape and adds no further useful information. Therefore, for the data set shown in Figure 3.23a, an 8 bit scan would more than suffice. Compare this to the 8 bit histogram for a much less noisy data set (Figure 3.23a). Only two peaks are present which is common in any real system where signals will likely lie somewhere between two bin values. In this case the noise is less than a bin width and thus one

would be justified in increasing the bit depth of the scan. Even at 10 bits the noise is only just creeping out of the two main bins. In this case a 12 bit scan would be optimal.

It was decided to try scanning the films in 48 bit mode to see if any increase in sensitivity could be gained particularly in the high dose region where small signals were present. Scans were repeated using 48 bit depth with no increase in sensitivity and essentially identical response. To determine the amount of noise present in the scanner a series of three identical 24 bit scans were performed at 600 DPI resolution. A ROI was placed over exactly the same area in each scan and histograms generated with the results shown in Figure 3.24. The noise in the scanner is seen as the variation in counts between each bin. As the variation only occurs across three bins it can be concluded that the noise is on the order of 1 pixel value from the mean. Therefore in our case, a 12 bit scan was quite appropriate and bit depth was not the limiting factor. This is the case for most modern document scanners, where cheap A/D converters enable nearly all scanners to scan at 30 bits or greater. The real limitation is the dynamic range of the system where the quality of the CCD and filters are the major factors.

Using the histogram method described it is possible to determine an optimal bit depth by analysing the histogram of several small identical ROIs for a 24 bit scan(8 per channel). If the histogram is more than a few bins wide and variation is seen between scans then there is little to be gained from increasing bit depth. Choosing the appropriate bit depth saves on storage space as well as the working memory required to do image processing.

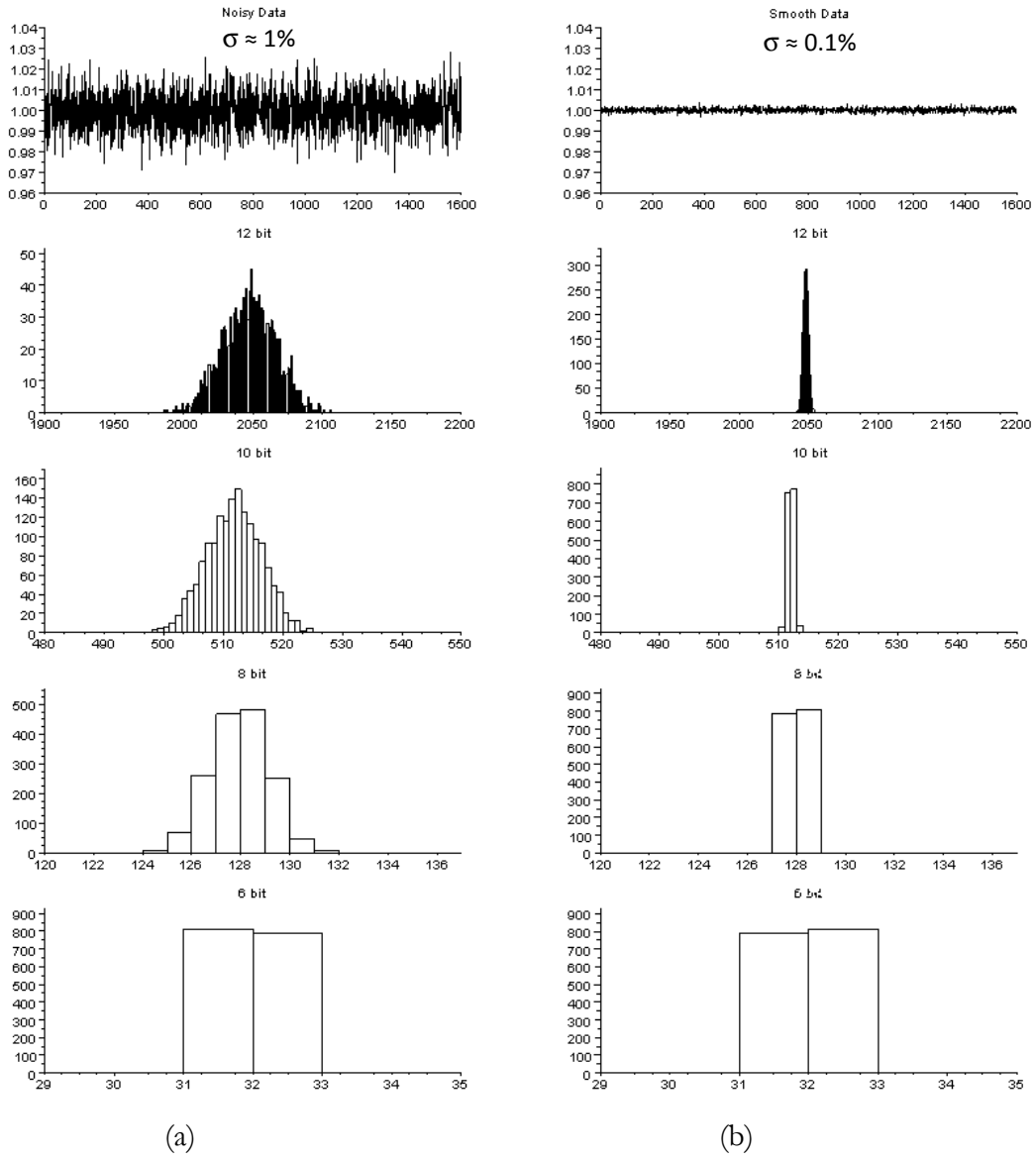

Figure 3.23. Noisy (a) and smoothed (b) data sets with histograms for various bit depths per channel.

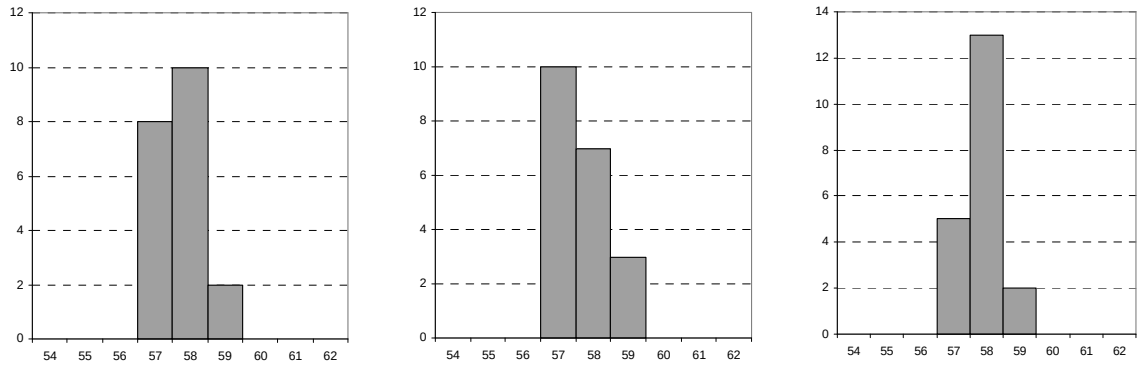

Figure 3.24. Histograms of pixel values for identical ROIs for 3 separate scans.

3.7 Conclusion

In this chapter the characteristics of Gafchromic® XR-RV2 have been investigated as well as protocols for scanning such films on a document scanner. The film was found to have a dose range ideally suited to this work. It is sensitive to doses as low as 20 mGy and up to at least 20000 mGy when read using the red channel. For doses above ~15000 mGy the scanner channels begin to saturate resulting in decreased sensitivity. The effect of bit depth on sensitivity of measurements was also investigated. Theoretically a 48 bit scan will provide greater sensitivity than a 24 bits, however due to electrical noise in the scanner, 24 bits was shown to be sufficient. Using the lower bit depth halves the required storage and working memory required and speeds up image processing tasks. The energy dependence of this film was also quantified as it has been identified as a potential limitation for this study. The total variation between 60 – 125 kVp was found to be ~14% at 1000 mGy. This introduces an uncertainty into the dose calculation which was modelled from a 96 kVp data set. A dose uncertainty analysis was performed and verified. A 1σ uncertainty of ~9% was predicted at 1000 mGy with uncertainties increasing above and below 1000 mGy.

The scanning protocol and dose response curve can now be used to calculate dose from a clinically exposed sheet of Gafchromic® film. The patient film results are presented later in Chapter 5.

4. DICOM Simulations

This chapter covers the methods used to simulate radiation field geometries and doses. The information required to reconstruct the radiation fields is stored within the acquisition files and encoded according to the DICOM standard. First an introduction to the DICOM standard will be given including file structure and encoding. The reconstruction process using the information contained within the DICOM files will be described in detail beginning with the geometry reconstructions followed by the dose calculations. Finally the program structure of the software will be described with examples of the user interface.

4.1 Introduction to DICOM

With the increased use of CT, MRI and other digital modalities in the 1970's and 80's problems began to arise where files could often only be decoded by the machine on which they were produced. This was quickly identified by clinicians, who for example wanted to use a CT scan for treatment planning but were unable to decode the vendors proprietary file format. It quickly became apparent that a standard was required to facilitate interconnectivity and functionality [67].

In 1983 the American College of Radiology (ACR) and the National Electrical Manufacturers Association (NEMA) formed a joint committee to develop a standard with an aim to:

- Promote communication of digital image information, regardless of device manufacturer.
- Facilitate the development and expansion of picture archiving and communication systems (PACS) that can also interface with other systems of hospital information
- Allow the creation of diagnostic information data bases that can be interrogated by a wide variety of devices distributed geographically. [67]

The first ACR-NEMA standard was published in 1985. The initial standard required significant improvements and further revisions were released in 1986 and 1988 with the 1988 standard being designated version 2.0. Each revision added support for more modalities and more sophisticated structure. By 1988 the standard was gathering acceptance among manufacturers. In 1993 the third major revision was released, V3.0, and the standard was renamed to the DICOM Standard (Digital Imaging and Communications in Medicine) in order to improve international acceptance. Officially 3.0 is still the most recent release. However the standard is under constant revision therefore one usually refers to DICOM

Standard and mentions the latest publication date. The DICOM standard also makes use of mature standards where possible such as JPEG and TCP/IP.

The DICOM standard is now almost universally accepted by medical device manufacturers and defines:

- How to encode a file and what information must be stored.
- How to transfer files between modalities and servers.

4.2 File Structure and Encoding

While the DICOM standard defines both file structure and communication, only the file structure is relevant in this work. The parts of the standard relevant to file structure and encoding are:

- PS 3.5: Data Structures and Encoding [68].
- PS 3.10: Media Storage and File Format for Media Interchange [69].

4.2.1 File Structure

A DICOM file consists of two parts; a *Meta Information* section and a *Data Set* section as shown schematically in Figure 4.1. The *Meta Information* section contains indentifying information about the encapsulated *Data Set*.

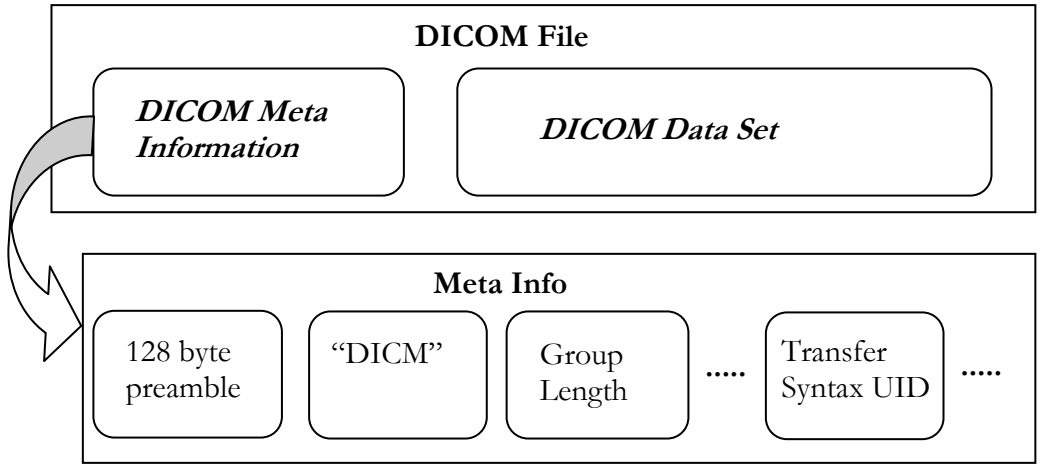

Figure 4.1 DICOM file structure.

The file begins with 128 bytes reserved for preamble. These bytes may be used for application specific use and have no requirements for formatting. The next four bytes contain the upper case character string "DICM". This is intended as a simple way to tell if a file is or is not a DICOM file. The Group length *Data Element* then follows which gives the length of the remaining Meta section enabling a program to skip directly to the data if desired. The last *Data Element* of use to us is the Transfer Syntax UID that defines the transfer syntax of the following *Data Set*.

When transferring data the byte stream may be transmitted with either the most or the least significant bit first. These two variations in byte ordering are referred to as little-endian and big-endian respectively. The DICOM standard allows for both methods of transfer and is defined by the *Transfer Syntax UID*. The Meta Information however is required to be encoded as Explicit Value Representation(VR) and little-endian. Explicit VR and data encoding are discussed below.

4.2.2 Data Encoding

A DICOM *Data Set* is made up of information which is encoded into *Data Elements*. Each Data Element is encoded as shown in Figure 4.2.

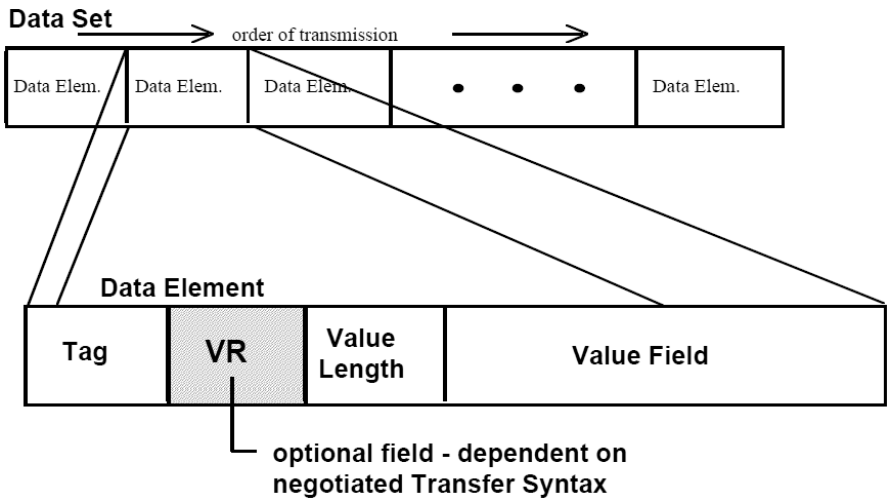

Figure 4.2 A *Data Element* (Source: PS 3.5 Fig 7.1-1).

Data Element fields:

Attribute Tag	an ordered pair of 16-bit unsigned integers representing the Group Number followed by Element Number. Even Group numbers are reserved for the standard while odd numbers may be used for proprietary tags. Tags are organised into groups of common information. For example the group tag 0x0010 is the Patient group number, therefore all tags starting with the group number 0x0010 will be about the patient in some way. 0x0018 is the acquisition tag and is of the most interest to this study.
VR	Value Representation. A two Byte character string describing the data type of the Value Field. This tag is only required if the transfer syntax calls for Explicit VR.
Value Length	a 16 or 32 bit unsigned integer defining the length of the Value Field. It has many conditional options for specification (PS. 3.5.7.1.1)
Value Field	the actual data, encoded as described by the previous fields.

As mentioned previously, the data set may be encoded as Explicit or Implicit VR. For Implicit VR each computer must have a DICOM data dictionary to be able to decode the value fields correctly.

The inclusion of implicit/explicit VR and little/big-endian encoding, combined with different *Data Element* structures for certain VR values requires a program be robust enough to handle and successfully decode all these variants.

An example of the Transfer Syntax UID Data Element from a cardiac study is shown in Table 4-I.

Table 4-I. Transfer Syntax UID Data Element encoded as Explicit VR Little-endian.

Tag		**VR**	**VL**	**Value Field**
Group 0x0002 16 bit unsigned integer	Element 0x0010 16 bit unsigned integer	UI 2 byte character string	22 16 bit unsigned integer	1.2.840.10008.1.2.4.70
2 bytes	2 bytes	2 bytes	2 bytes	VL bytes (22)

4.3 Reconstructions

The aim of this thesis has been to perform a reconstruction of radiation fields that closely resembles how the patient was actually exposed. To perform the reconstruction requires specific geometrical and exposure information. Each acquisition series that is saved should contain information regarding the exposure in its DICOM file structure. The information required and corresponding tags are listed in Table 4-II. Details of the geometrical reconstructions and dose estimations are described separately below.

Table 4-II. List of tags for reconstruction

Tag	*Description*
0x0018,0x0040	Cine rate, frames per second.
0x0018,0x0060	KVp, peak kilo voltage.
0x0018,0x1110	Distance source to detector
0x0018,0x1111	Distance source to patient
0x0018,0x1150	Exposure time in ms.
0x0018,0x1151	Tube current in mA.
0x0018,0x1154	Average pulse width in ms
0x0018,0x115E	Dose Area Product in $dGycm^2$.
0x0018,0x1162	Intensifier size
0x0018 0x1510	Positioner primary angle
0x0018 0x1511	Positioner secondary angle
0x0018,0x1602	Shutter left vertical edge
0x0018,0x1603	Shutter right vertical edge
0x0018,0x1606	Shutter upper horizontal edge
0x0018,0x1607	Shutter lower horizontal edge

4.3.1 Geometry

The aim is to reconstruct the shape and location of the radiation fields at the patients skin based on the above information. This can be achieved if the detector angle and table height are known. Unfortunately the table height was not recorded by the machine used in this study and the source to patient distance (SPD) turned out to be incorrectly calibrated by the

manufacturer. Nevertheless, a good estimate can be made based on a standard table height. The simulations used two table height methods. The first was a simple fixed height of -12 cm from the isocentre as this is the most common table height used by the operator. The second method involved using the incorrectly calibrated SPD and an approximate correction factor based on observed discrepancies.

The approach used to calculate the fields at the patients skin is as follows:

1. Find focal spot position.
2. Locate each corner of the square detector.
3. Fit parametric lines between focal spot and each corner.
4. Find intersection of each line with table plane.
5. Connect the four table intersections to form field.

Since the X-ray tube and detector are mechanically fixed opposite each other in a C-arm only the detector angulations are required to calculate the tube position as well. Firstly a coordinate system is assumed with an origin at the isocentre of the C-arm where the x direction is along the Left to Right orientation, y direction is Cranial/Caudal and z direction is the vertical as illustrated in Figure 4.3.

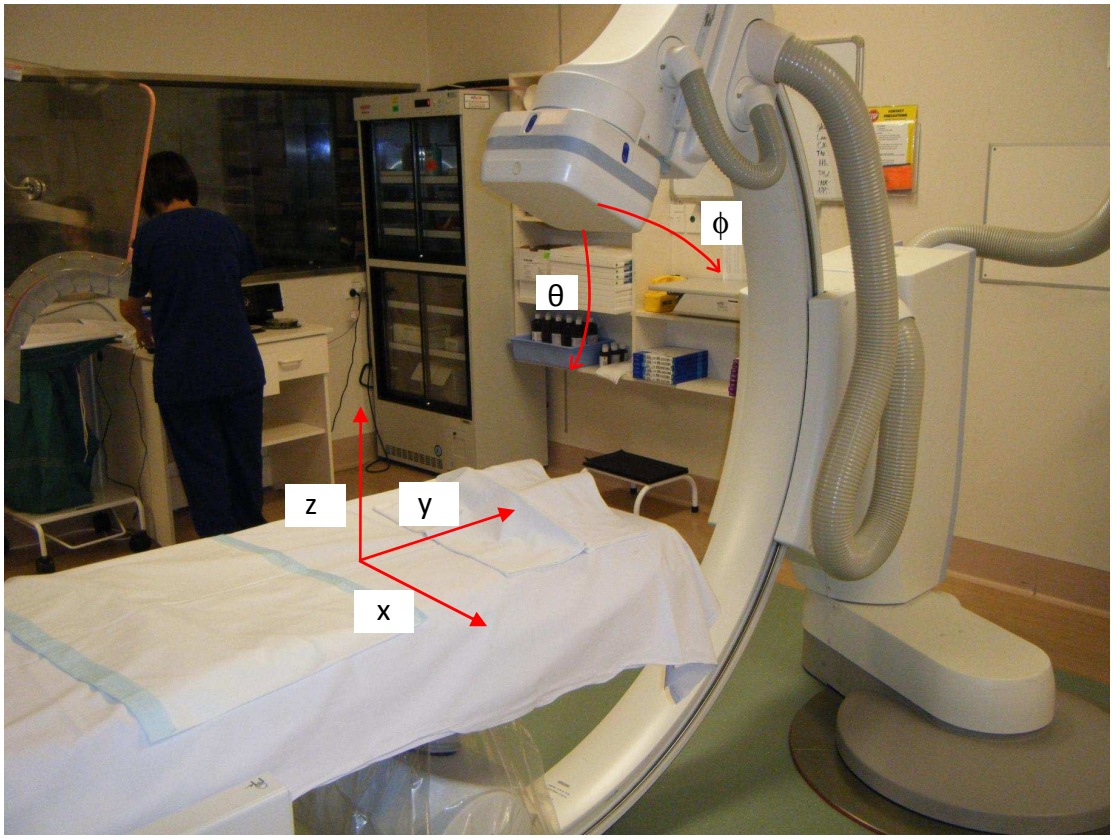

Figure 4.3. C-Arm system showing orientations used for simulation.

The position of the focal spot is then given by

$$\begin{aligned} x_{spot} &= -r\sin(\theta)\cos(\phi), \\ y_{spot} &= -r\sin(\phi), \\ z_{spot} &= -r\cos(\theta)\cos(\phi), \end{aligned}$$

where r is the distance from the spot to the isocentre (fixed), and ϕ and θ are the primary and secondary angles respectively.

The following equations define the x, y and z coordinates at the centre point of the detector as well as an approximation of the four sides.

$$\begin{aligned} x_c &= r_d\sin(\theta)\cos(\phi), \\ y_c &= r_d\sin(\phi), \\ z_c &= r_d\cos(\theta)\cos(\phi), \end{aligned} \tag{4.1}$$

$$d\theta = d\phi = \tan^{-1}\left(\frac{\text{field size}/2}{r_d}\right), \tag{4.2}$$

$$\begin{aligned} x'_{side1} &= r_d\sin(\theta)\cos(\phi + d\phi), \\ x'_{side2} &= r_d\sin(\theta)\cos(\phi - d\phi), \\ x'_{side3} &= r_d\sin(\theta + d\theta)\cos(\phi), \\ x'_{side4} &= r_d\sin(\theta - d\theta)\cos(\phi), \end{aligned} \tag{4.3}$$

$$\begin{aligned} y'_{side1} &= r_d\sin(\phi + d\phi), \\ y'_{side2} &= r_d\sin(\phi - d\phi), \\ y'_{side3} &= r_d\sin(\phi), \\ y'_{side4} &= y_{side3}, \end{aligned} \tag{4.4}$$

$$
\begin{aligned}
z'_{side1} &= r_d \cos(\theta)\cos(\phi + d\phi), \\
z'_{side2} &= r_d \cos(\theta)\cos(\phi - d\phi), \\
z'_{side3} &= r_d \cos(\theta + d\theta)\cos(\phi), \\
z'_{side4} &= r_d \cos(\theta - d\theta)\cos(\phi),
\end{aligned}
\tag{4.5}
$$

where r_d is the distance from the isocentre to the detector face.

The sides previously calculated in Eq.(4.3), (4.4) and (4.5) are actually an approximation; to calculate the true sides requires an extra step. Because the sides of the detector lie in a flat plane they do not rotate in the same manner as the centre of the detector and are slightly further away from the focal spot than the detector centre as seen in Figure 4.4.

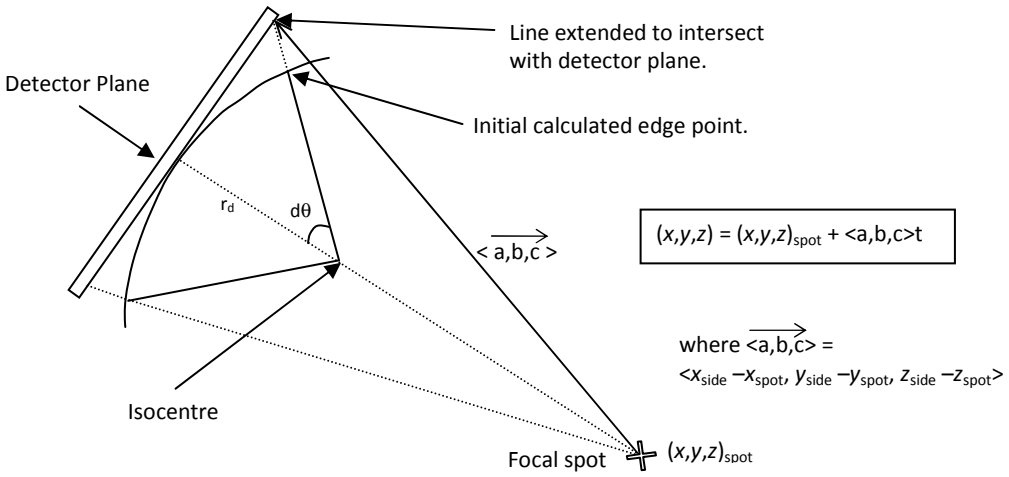

Figure 4.4. Initial calculated edges inaccurate due to the detector being flat and not curved.

To correct for this the following steps were necessary. First a detector plane is defined by a normal vector and the centre point. Then a line is defined between the focal spot and the approximate points and extended to find the intersection with the detector plane. This is only performed for two sides in the ± secondary angle direction, the other two sides are found from the first two by using a cross product method to save on computation time.

The general equation of a plane is given by:

$$ax + by + cz + d = 0,$$

where $\langle a, b, c \rangle$ is a vector normal to the plane. The parameter *d* can be found by solving for a known point x_0 y_0 z_0. For the detector plane this yields:

$$x_c x + y_c y + z_c z = x_c^2 + y_c^2 + z_c^2 . \tag{4.6}$$

The parametric equation for a line from the isocentre to a side can be expressed as:

$$\begin{aligned} x &= x_{iso} + \overrightarrow{(x_{side} - x_{iso})} \cdot t , \\ y &= y_{iso} + \overrightarrow{(x_{side} - x_{iso})} \cdot t , \\ z &= z_{iso} + \overrightarrow{(x_{side} - x_{iso})} \cdot t . \end{aligned} \tag{4.7}$$

Inserting Eq.(4.7) into Eq.(4.6) and solving for *t* will give the intercept for these lines with the plane of the detector thus giving the true coordinates for each side:

$$x_c x_{iso} + x_c (x_{side} - x_{iso}) \cdot t + y_c y_{iso} + y_c (y_{side} - y_{iso}) \cdot t + z_c z_{iso} + z_c (z_{side} - z_{iso}) \cdot t = x_c^2 + y_c^2 + z_c^2$$

$$x_c (x_{side}) \cdot t + y_c (y_{side}) \cdot t + z_c (z_{side}) \cdot t = x_c^2 + y_c^2 + z_c^2$$

$$t = \frac{x_c^2 + y_c^2 + z_c^2}{x_c (x_{side}) + y_c (y_{side}) + z_c (z_{side})} .$$

Now the true coordinates for the sides of the detector have been found. Note that an alternative, more elegant solution to this problem would be to simply define r_d as the radius of a sphere passing through the sides of the detector and not simply the radius to the centre of the detector as assumed in Eq.(4.1).

Using the true coordinates for the sides the corners of the detector are found by adding two side vectors:

$$\begin{aligned} x_{corner1} &= (x_{side1} - x_c) + (x_{side3} - x_c) , \\ y_{corner1} &= (y_{side1} - y_c) + (y_{side3} - y_c) , \\ z_{corner1} &= (z_{side1} - z_c) + (z_{side3} - z_c) , \end{aligned}$$

$$\begin{aligned} x_{corner2} &= (x_{side1} - x_c) + (x_{side4} - x_c) , \\ y_{corner2} &= (y_{side1} - y_c) + (y_{side4} - y_c) , \\ z_{corner2} &= (z_{side1} - z_c) + (z_{side4} - z_c) , \end{aligned}$$

... etc.

Next a parametric line is drawn between the focal spot and each corner described by:

$$\begin{aligned} x &= x_{spot} + \left(x_{corner} - x_{spot}\right)\cdot t\,, \\ y &= y_{spot} + \left(y_{corner} - y_{spot}\right)\cdot t\,, \\ z &= z_{spot} + \left(z_{corner} - z_{spot}\right)\cdot t\,. \end{aligned} \tag{4.8}$$

Solving the z component of Eq.(4.8) for the *t* value by setting z equal to the table height gives the *x* and *y* coordinates in the table plane:

$$t = \frac{z_{\text{table height}} - z_{spot}}{\left(z_{corner} - z_{spot}\right)}\,,$$

Thus:

$$\begin{aligned} x_{table} &= x_{spot} + \left(x_{corner} - x_{spot}\right)\cdot \frac{z_{\text{table height}} - z_{spot}}{\left(z_{corner} - z_{spot}\right)}\,, \\ y_{table} &= y_{spot} + \left(y_{corner} - y_{spot}\right)\cdot \frac{z_{\text{table height}} - z_{spot}}{\left(z_{corner} - z_{spot}\right)}\,. \end{aligned} \tag{4.9}$$

With the four corners of the field at the table top defined using Eq.(4.9) it is simply a matter of defining the edges between them. One must take care when joining the points so as to connect them in the correct way, see Figure 4.5. In order to get the points to be automatically joined correctly a "centre of mass" method was used. In this method the centre of mass for the points is calculated for both *x* and *y* by simply averaging the four corners:

$$x_{\text{centre of mass}} = \frac{1}{4}\sum_{i=1}^{4} x_i\,, \qquad y_{\text{centre of mass}} = \frac{1}{4}\sum_{i=1}^{4} y_i\,.$$

The angle is then calculated between the centre of mass and each point. The points are then sorted according to angle and joined in that order.

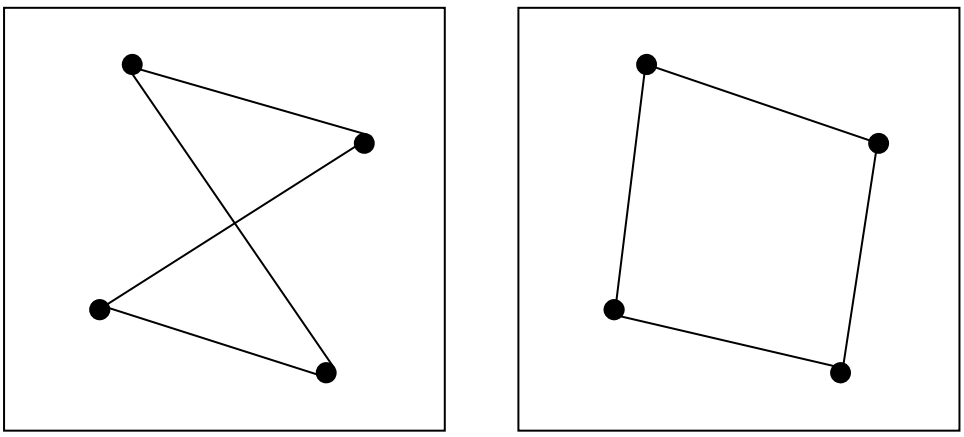

Figure 4.5. a) Points joined erroneously. b) Points joined using centre of mass method.

4.3.2 Verification

During the coding process various known parameters were calculated and checked on the fly to ensure correct reconstruction. These included field size checking by calculating vector lengths and heights of intersection etc. The final verification was achieved by using a computed radiography (CR) cassette positioned on the table and exposed at various angles. The acquisition runs were kept and analysed using the program and output at the same scale and resolution. As can be seen in Figure 4.6 the simulation provided strong visual agreement in the real trial.

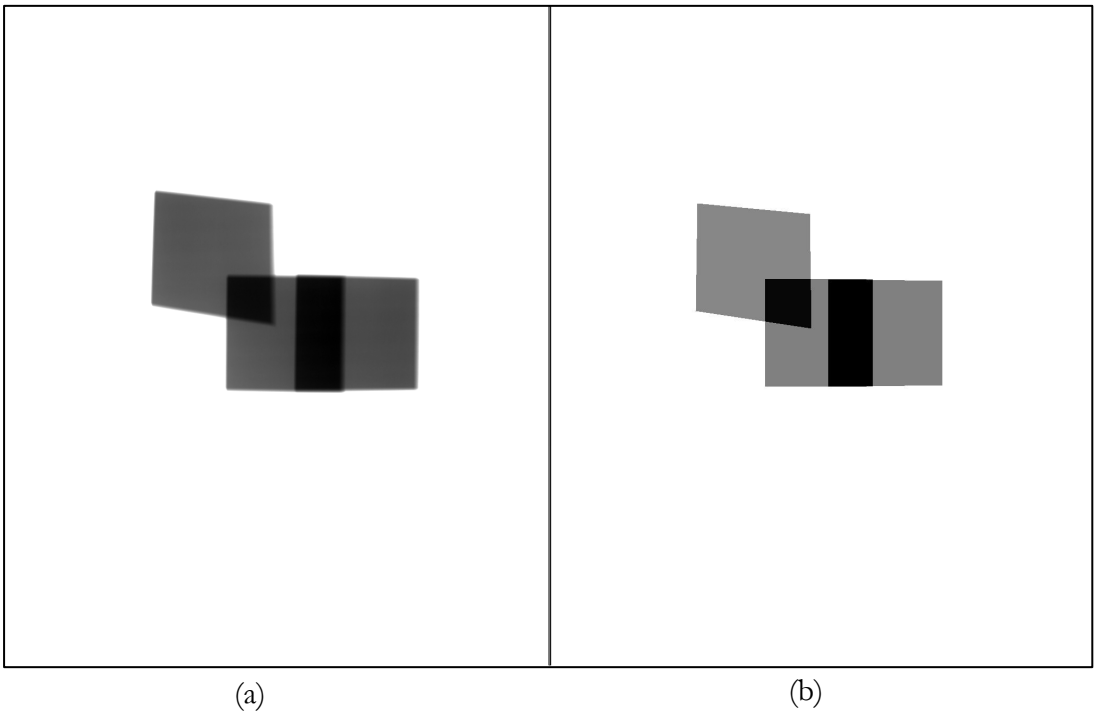

Figure 4.6. Verification of geometries. a) CR plate image. b) simulation result.

4.3.3 Dose calculation

After the size and shape of the fields is known a dose must be calculated for each field. There are a few ways to do this [70]. Morrell and Rogers [25] used the kVp, mA and time information by measuring the doses directly and calculating charts to compute doses for any kVp and mAs setting. The same approach was attempted here on the Siemens C-arm. A dose chamber was set up with supports for added tube loading material approximately 20 cm above the dose chamber so as to avoid backscatter as shown in Figure 4.7. Copper attenuation was steadily added to push the machine through a range of kVp and all information was recorded. Using this approach the dose can be normalised to mAs, and kVp response can be graphed as shown in Figure 4.8.

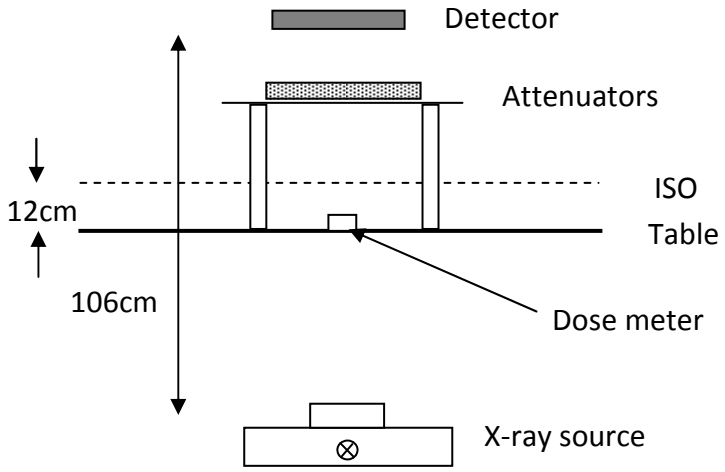

Figure 4.7. Test setup for dose measurements of acquisition runs.

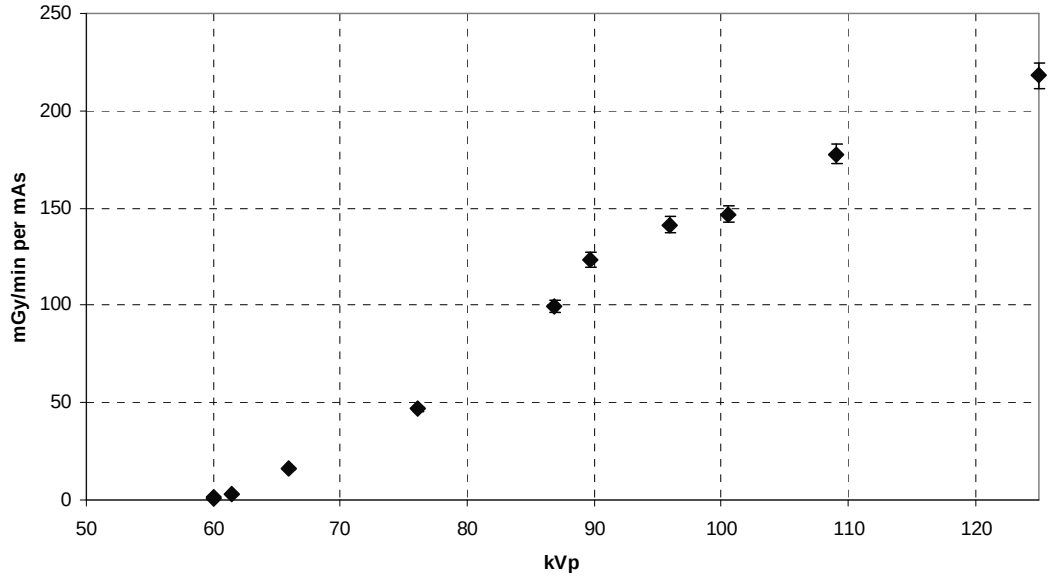

Figure 4.8. Dose rate per mAs response curve for the Siemens Axiom Artis.

Unfortunately this method was unsuitable for this machine due to its automatic filtration algorithms. Filtration is used in nearly all diagnostic X-ray equipment to attenuate low energy photons before they reach the patient. Filtration provides a saving on patient dose at the expense of tube loading and sometimes image quality. Angiographic machines such as the Axiom Artis used in this study often contain high amounts of filtration to reduce skin dose. The Axiom Artis has an intelligent filtration algorithm which modulates additional copper filtration to compromise between tube loading, kVp and patient dose.

The machine is set up to provide approximately 70 kVp. For low patient loading the machine will add its maximum filtration, 0.6 mmCu. As the loading increases the extra Cu filtration is gradually removed to increase photon flux while slowly increasing the kVp. Once all the filtration has been removed the machine must rely on increasing kVp to provide the required dose to the detector. Further reading on this technology can be found elsewhere [71].

In practice this swapping of filtration does not occur at predictable kVp therefore variation in mA was significant and lead to gross under and over estimations of dose.

An alternative method for dose estimation is to use the built-in dose area product (DAP) meter. Many older machines do not store this information, which is presumably why Morrell et al did not use it. The Axiom Artis does however, and this was the metric chosen for this study. The DAP should give a more accurate result since it is a direct measurement of the dose exiting the X-ray tube, see Chapter 2.

After some investigation and discussion with service engineers it was found that the DAP was not calibrated to include tabletop attenuation. For undercouch X-ray systems such as this it means that the DAP reported is always higher than the DAP reaching the patient due to table attenuation. In order to use the stored DAP values they must first be corrected for table attenuation.

To find this correction the data from the previous kVp, mA and dose measurements was used. The difference between reported dose and measured dose was calculated and plotted to find a function of best fit. Differences in reported and measured dose arise almost entirely from table attenuation but may also be caused by variation in DAP meter respose with kVp and backscatter. From Figure 4.9 it can be seen that the error decreases with kVp. At low kVps where the table absorbs more strongly the difference is ~30% and decreases as a power law to under 10% above 110 kVp.

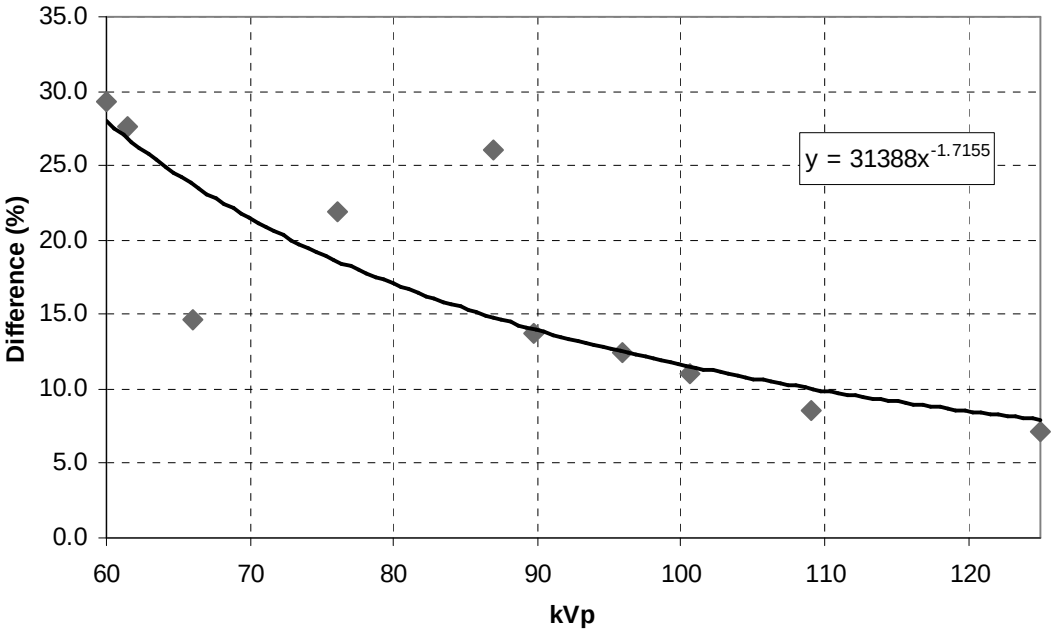

Figure 4.9. Difference between reported and measured dose showing the effect of kVp on table attenuation.

The dose to the patients skin can now be calculated by:

$$\text{Dose} = \frac{DAP_{reported}}{Area} \times \frac{(\mu_{en}/\rho)_{tissue}}{(\mu_{en}/\rho)_{air}} \times AttenuationCorrection \times BSF \ ,$$

where BSF is the backscatter factor.

The area of the beam at the patients skin is calculated from the field size at the detector using the inverse square law ratio of the source to patient distance and the source to intensifier distance (SID).

$$\text{Area} = \text{Field Size}^2 \left(\frac{\text{SPD}}{\text{SID}} \right)^2 .$$

The ratio of mass attenuation coefficients were found using XMUDAT [28] and ICRU44 soft tissue [72]. The ratio of mass attenuation coefficients varies by 6 - 10% between 20 and 80 keV respectively. A fixed 8% correction was used in this study relating to a 40 keV beam.

$$\frac{(\mu_{en}/\rho)_{tissue}}{(\mu_{en}/\rho)_{air}} \approx 8\% \text{ at 40 keV.} \qquad (4.10)$$

The back scatter factor was interpolated from results by Petoussi et al [73] for a 10 x 10 cm field using ICRU tissue. Below 70 kVp the BSF was a constant 1.32 and above 100 kVp was a constant 1.42. Between 70 and 100 kVp the BSF was calculated through linear interpolation:

$$BSF = 0.001 \times kVp + 1.32 \text{ for kVp between 70 and 100 kVp.}$$

4.3.4 Fluoroscopy estimation

The DICOM acquisition files contain no information about the contribution of dose from fluoroscopy. These parameters must be estimated and input manually into the simulation.

Three methods were used to estimate the dose contribution from fluoroscopy:

1. Fluoroscopy time: Fluoroscopy time is a unit that most cardiac labs will make effort to manually record as it is displayed clearly on the machine. The dose rate for different patient loadings was measured using the setup shown in Figure 4.10. Polymethyl methacrylate (PMMA) was added in 7.5 cm slabs to simulate patient thickness up to a total of 30 cm, each slab resulting in increased kVp. Measured dose rates varied from 1.07 to 54.7 mGy/min. The dose rate for each patient was then estimated by using the average CINE kVp to select the most likely patient thickness and applying the appropriate dose rate based on PMMA measurements. Finally the dose rate was multiplied by the total fluoroscopy time to give dose.

2. Difference between Cine DAP and total DAP: Another commonly recorded metric is the total DAP for a procedure. The fluoro DAP can be calculated by summing the DAP for each acquisition and subtracting from the total DAP. As with the CINE dose calculation, the fluoro DAP must be corrected for table attenuation and backscatter. This was achieved using the same corrections as the CINE runs. The corrected DAP is then divided among the fields in either an even or weighted fashion and finally divided by the area of each field to give a dose.

3. Reported fluoroscopic dose. This is simply the machine's estimate of skin dose based on its own DAP and internal knowledge of beam area. It is not found on most older systems. As with the DAP, the reported dose requires correcting in the same manner as the CINE runs.

In addition, two methods were used for distributing the fluoroscopic dose:

1. Even distribution - all fields were allocated an equal distribution of dose.

2. Weighted distribution - fields with higher CINE doses were allocated a greater proportion of the fluoroscopic dose. Perhaps to indicate the interventionalists increased interest in that particular view.

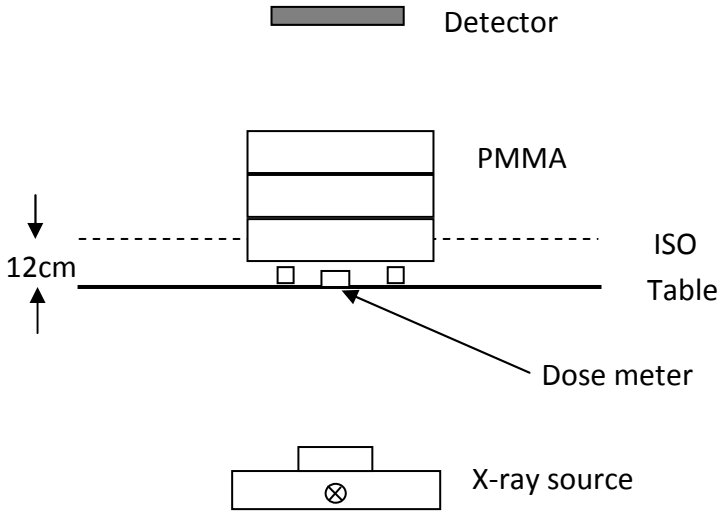

Figure 4.10. Test setup for fluoroscopic dose measurements.

4.3.5 Program Structure and Function

All code was written in the Java™ programming language and developed using BlueJ [74]. The program was designed to be able to work within ImageJ [62] and therefore makes use of several ImageJ methods for creating, modifying and saving images. The program structure is shown in Figure 4.11.

In addition the following classes were taken from David Clunie's *PixelMed Java DICOM Toolkit* [75]:

- DicomDictionary and DicomDictionaryBase.
- TagFromName.
- AttributeTag.
- ValueRepresentation.
- TransferSyntax.

The toolkit is made freely available for both non-commercial and commercial use.
When the scripter class is run, the following happens:

1. The Scripter passes the patient file directory and all fluoroscopic parameters for that patient to the MainMenue_ class.
2. The MainMenue class then calls File_Reader to analyse all the files in the directory and store those which are DICOM compliant.
3. MainMenue_ calls DrawFields with a specific fluoroscopic parameter.
4. DrawFields calculates doses and geometries. Then prints results to a text file and returns an image to MainMenue_ where the pixel values represent dose in mGy.
5. MainMenue_ scales and saves the image.
6. MainMenue_ calls DrawFields with different sets of fluoroscopic parameters and table heights repeating steps 4 -5.
7. When all possible iterations of fluoroscopic estimations and table heights are complete the Scripter calls MainMenue_ again with a new patient directory and fluoroscopic parameters.

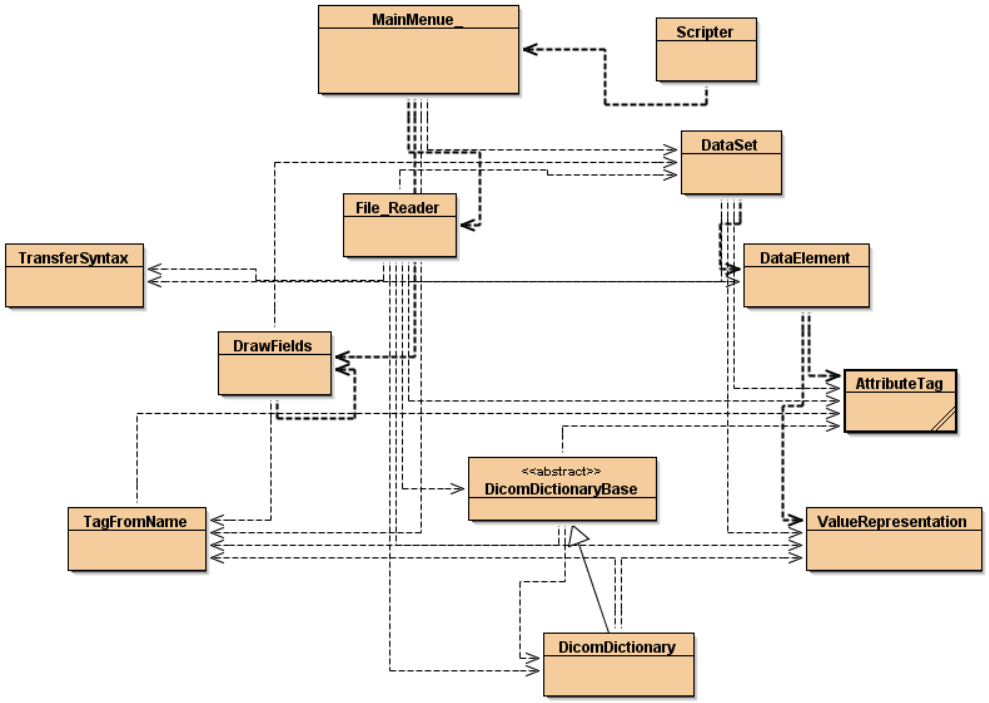

Figure 4.11. Program structure showing class dependencies and associations.

Main classes

MainMenue_

This is the central class of the program. It serves as a graphical user interface (GUI), obtains fluoroscopic estimation parameters from user input, stores DICOM data temporarily, saves images to disk and makes calls to the other main classes. The GUI is shown in Figure 4.12.

File_Reader

This class scans a given directory for DICOM files then reads all the DICOM information from them and stores it into a hash table. It can also be specified to analyse subdirectories.

DrawFields

This is the main "work horse" class. It not only calculates and draws the radiation fields but also calculates doses for each field. The class receives an array of DataSets, each DataSet representing a single acquisition run. It also requires fluoroscopic information which is passed in along with the DataSets by the MainMenue_ class. Once completed, it prints out the results of the simulation to an output window as well as a text file and returns the image to the MainMenue_ class. An example of the dose summary is shown in Figure 4.13.

Other classes are utility classes for storage, sorting and decoding.

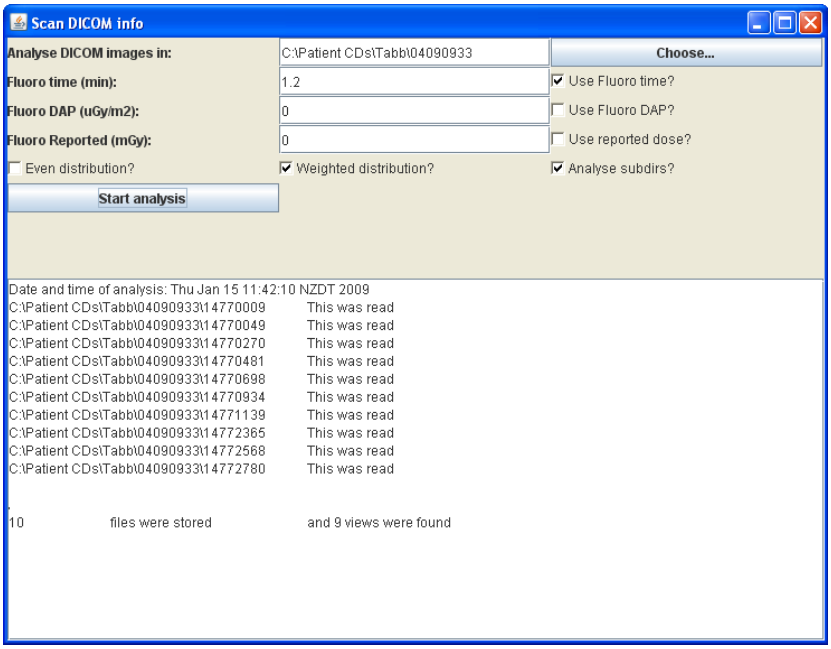

Figure 4.12. GUI for the MainMenue_ class. Required parameters are input through this screen.

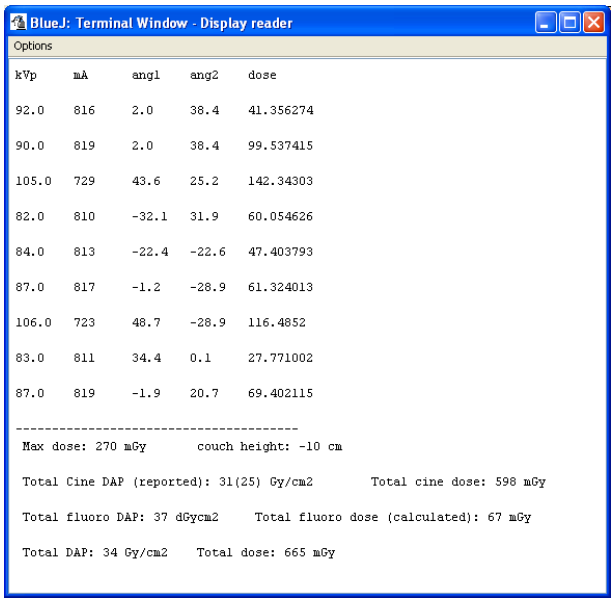

Figure 4.13. Example of the output from the DrawFields class after simulations are complete.

4.4 Results

The result of a simulation performed on real patient data is shown in Figure 4.14. The darkening of the fields is proportional to the dose of that field and the region of highest dose is clearly identified on the medial inferior aspect. Image orientation is shown as if looking directly at the patients back from behind, i.e., the left of the image is the patients left. Due to time constraints it was not possible to add reference patient anatomy to this image for localisation. In the mean time the film could easily be aligned by realising that the heart is always in the isocentre of the image, therefore the centre of the image could be aligned with the patients heart. Comparison with the true doses as measured with film are presented in the next chapter.

4.5 Discussion

The simulation method presented in this section produced results with a high level of geometrical accuracy. The total time for calculating, drawing and saving an examination is approximately four seconds for an eight view study on a Pentium4 2.66 GHz processor. The level of dose accuracy is investigated in the next chapter where simulations are compared to the film results.

In order to accommodate different computer systems the encoding of files can vary significantly even within the standard. The algorithms to decode a DICOM file need to be fairly complex and robust to handle all the encoding options. Of particular interest is the implicit VR encoding scheme. In this scheme both the sender and receiver must have a

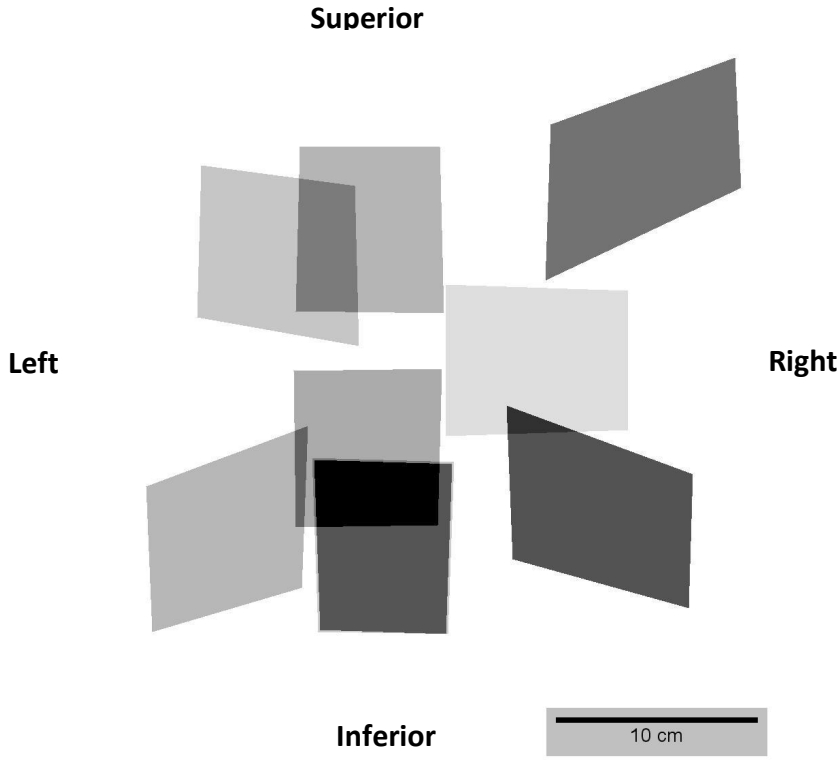

Figure 4.14. Result of patient simulation showing significant field overlap in the inferior region.

dictionary to be able to interpret the file. Problems may arise where newer machines contain new tags that are not present in an older DICOM dictionary. At present the program can handle all transfer syntaxes for the main data set, however, the meta information must be explicit VR little-endian as required by the standard.

An obvious parameter that is missing from the simulations is collimation. On this machine there are two types of collimation. The regular collimation works with lead shutters that cone down along the horizontal and/or vertical side of the image. The position of the lead shutters should be recorded in the DICOM files, however the positions reported by this machine were nonsensical and therefore unusable. The second method of collimation is with a semi-transparent wedge filter. This type of collimation is particularly useful due to the ovoid shape of the heart compared to the square radiation beam. The wedge filter can be used for improving image uniformity around the heart/lung edges and reduces unnecessary patient dose. Wedge filter position is not recorded at all. The impact of not including collimation is uncertain until comparisons are made with the film samples. Certainly it could make a difference to maximum dose where field overlap is highly dependent on field size.

Similarly the horizontal table position is not recorded in any way. During a procedure the table top can be moved in any direction, a technique called *panning*. As such the use of panning would throw out the centre reference points leading to uncertainties in beam location. As with the collimation this could have an impact on maximum dose and location of that dose.

5. Comparison of Experimental Results and Simulations

The word "dose" is used ubiquitously and often ambiguously in medical physics. The first question one must ask is what dose parameters do we wish to compare? One could measure a skin dose for each beam of radiation and report a total dose as the sum of these beams; this is how the Siemens machine defines total dose. However, this method does not make a great deal of sense as can be shown by the following example. Assume a single large field delivering 100 mGy covers a patients back, the total dose would be 100 mGy, see Figure 5.1a. Now imagine the large field is broken up into 4 smaller fields, each delivering 100 mGy to a small area of the skin. The total dose reported is then 4 x 100 mGy = 400 mGy. This is not correct; dose is defined as J/kg, therefore the dose is the same for both scenarios.

Instead the dose area product metric was used. The DAP simply multiplies the dose of each field with the area it covers and is a good measure of total radiation incident on the patient. For more detailed information on DAP refer back to Chapter 2.

The second metric utilised is maximum skin dose. This is perhaps the most important measure as it indicates the risk of a patient developing any deterministic effects. Since the machine is not able to record or estimate maximum dose, comparisons are made directly between film and simulation.

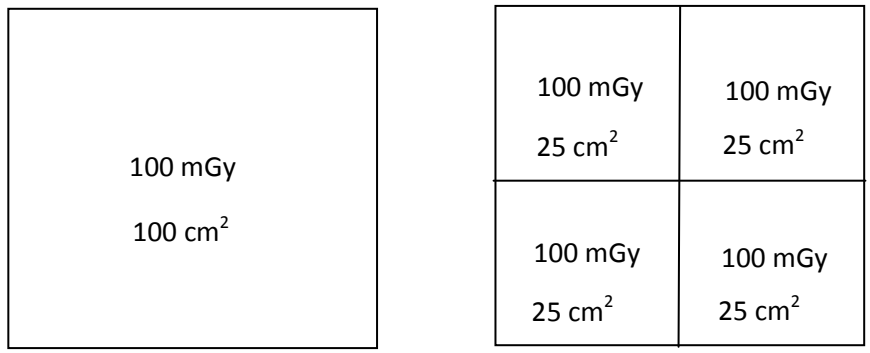

Figure 5.1. Difference between total dose and DAP for different field combinations. a) A single large field with the correct total dose and DAP. b) Four small fields giving and inflated total dose but correct DAP.

5.1 Film results

5.1.1 Dose Calculation

It was decided that kerma measurements were the most appropriate to work with since the dose meters used are calibrated in terms of air kerma. In a real situation, the film would receive a dose contribution not just from the kerma, but also backscatter from the patient. Thus what is measured with clinically exposed films is actually kerma *plus* backscatter.

To turn kerma measurements into a dose they must be multiply by the ratio of mass attenuation coefficients for air and tissue. Recalling from basic radiation dosimetry Eq.(2.5):

$$D_{tissue} = \frac{(\beta \cdot \mu_{en}/\rho)_{tissue}\Psi_{tissue}}{(\beta \cdot \mu_{en}/\rho)_{air}\Psi_{air=}} D_{air} \approx \frac{(\mu_{en}/\rho)_{tissue}}{(\mu_{en}/\rho)_{air}} D_{air}. \qquad (5.1)$$

where (μ_{en}/ρ) is the mass energy absorption coefficient, $\beta = D/K_{col}$ see Figure 2.3 and Ψ is the photon fluence.

Since the area of interest is at the very surface of the tissue, the radiation conditions in air and at the tissue surface are almost identical, thus β and Ψ will cancel. For all intents and purposes the kerma is approximately equal to the dose at diagnostic energies. The final equation for skin dose is then:

$$D_{tissue} \approx \frac{(\mu_{en}/\rho)_{tissue}}{(\mu_{en}/\rho)_{air}} (K_{air})^{tissue}. \qquad (5.2)$$

Which from Eq.(4.10) was found to be ≈ 8% of K_{air}.

Films were scanned according to the protocol presented in the Chapter 3. To calculate doses from the films a custom ImageJ plug-in was programmed.

The plug-in automatically performed the following for each image:

- Obtained the pixel matrix for the Red channel.
- Run a 3x3 pixel median filter.
- Invert the pixel values of an image and subtract background pixel value.
- Move to a pixel and calculate dose based on net pixel value, then multiply by the pixel area to give a DAP.

- Move through each pixel adding DAP in a cumulative fashion whilst keeping a record of the highest dose.

For a 150 DPI scan pixel size was calculated to be 0.169 x 0.169 mm. In addition, certain pixels were excluded from the dose calculation. Any pixels that were within 10 pixels of the image edge were excluded due to scanner non-uniformity at the very edge of the scanner bed. Pixels with a net value of less than 2.0 were excluded as the uncertainty for dose calculations at this low level would likely introduce large errors, see section 3.5.

5.1.2 Dose Area Product

To check the consistency of film measurements the total calculated DAP was plotted against machine reported DAP with the results shown in Figure 5.2. The y axis error bars represent a 15% uncertainty based on calculations made in section 3.5. A linear fit was found with a forced intercept through zero. The relationship between film and reported DAP was consistent with an R^2 value of 0.984. The slope of the fit was 1.49 indicating that the film DAP measurements were 49% higher than the reported DAP. There are numerous factors affecting the relationship between film and reported DAP such as:

- Table attenuation.
- DAP meter calibration.
- Backscatter into the film.
- Minimum film dose thresholds.
- Film energy dependence.

Of these factors it is known that the DAP meter on this machine is not calibrated for table attenuation meaning that the reported DAP will be greater than the DAP that actually reaches the patients skin. On the other hand, the reported DAP does not include back scatter from the patient. If say 20% table attenuation is assumed and 40% back scatter as found in Chapter 4, that leaves an expected 20% increase in film DAP from these two factors alone. It should be noted that the backscatter factor only accounts for scattered radiation back into the radiation field. In reality radiation will also be scattered around the periphery of the field and thus develop the film in an area around the beam. This leads to increased dose when measured on film compared to a DAP meter. In an effort to reduce this effect, a pixel threshold of 2.0 was used as mentioned in section 5.1.1. This was originally introduced to reduce dose calculation errors at very low doses, however it was also found to restrict the inclusion of scattered radiation. As the threshold is lowered more pixels are included and the DAP

increased, likewise when the threshold was increased the DAP decreased. The setting of a pixel threshold is somewhat arbitrary and it was noticed that some primary radiation fields actually had exposures similar to that of the background scatter. For this reason the threshold was left at 2.0 for final calculations. This possibly explains why the film is closer to the reported DAP for low dose procedures where the scattered radiation is likely to be very low and thus excluded (Figure 5.2). For films where all fields were distinguishable from background a decrease in film DAP of ~10% was possible by excluding extra-field scattered radiation.

At this point it should become clear that there is no such thing as a "true DAP". Both methods are in fact estimates and neither measurement could be called "correct" as they are measuring DAP in a different ways.

Figure 5.3 shows the residual of film DAP from the linear fit shown in Figure 5.2 with a σ of 15%. It can be seen that above 50 Gycm^2 the deviation is somewhat random and generally within ± 15%. Below 50 Gycm^2 the deviation becomes increasingly negative indicating that the film DAP becomes closer to the reported DAP, most likely due to the decreased scatter mentioned previously.

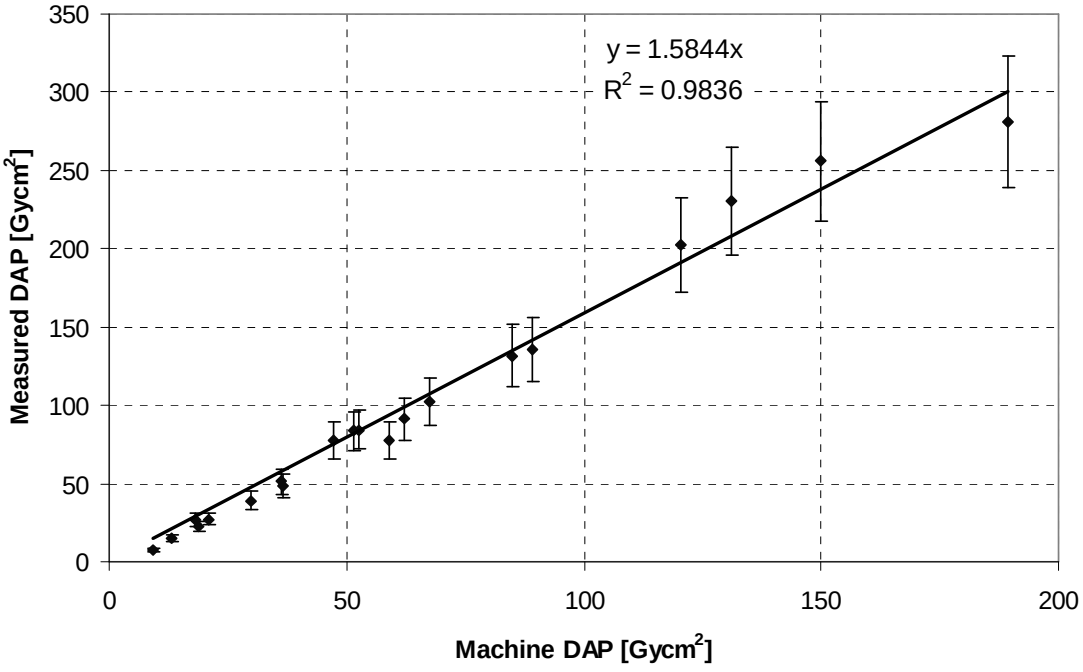

Figure 5.2. Machine DAP vs. Measured film DAP.

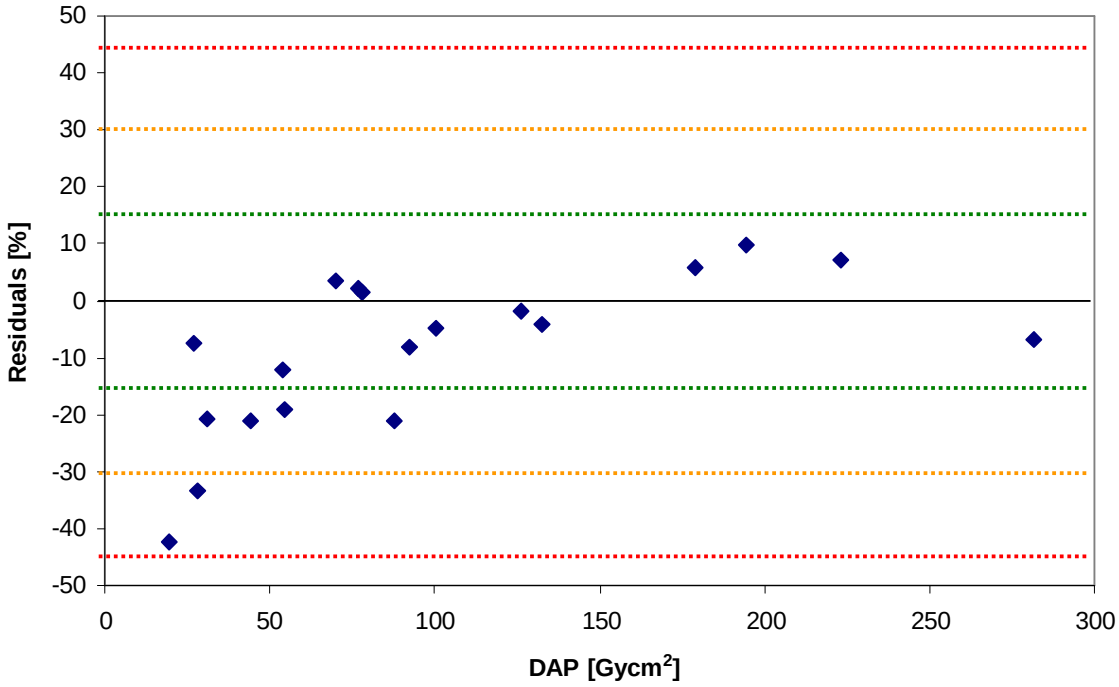

Figure 5.3. Film DAP deviations from the linear fit, where dashed lines indicate 1σ = 15%.

5.1.3 Maximum Dose

The maximum skin dose for all twenty patient's included in this study is shown in Figure 5.4. It can be seen that maximum skin dose was below 1000 mGy for the vast majority of patient's with a mode of 200 – 400 mGy. The highest dose a patient received was 2564 mGy, high enough for a transient erythematic reaction.

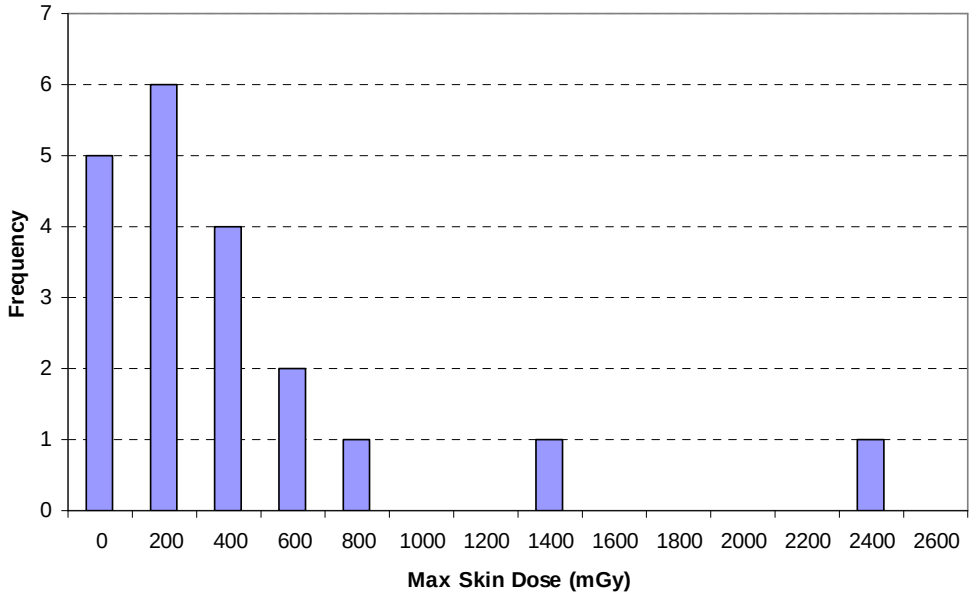

Figure 5.4. Histogram of maximum skin doses for all patient's.

5.2 Comparison with simulations

5.2.1 Determination of optimal parameters

Recalling Chapter 3 there were a number of different parameters to vary when simulating patient doses. In all there were twelve different permutations to simulate.

- Three different methods of fluoroscopic dose estimation.
- Two weighting schemes for fluoroscopic dose.
- Two methods of couch height estimation.

From the simulations the maximum dose and DAP were recorded for each permutation and plotted against the film measurements. A linear best fit through the origin was found and slope and R^2 values recorded in Table 5-I and Table 5-II.

All of the simulations provided sensible estimations for DAP and maximum skin dose. From these tables the best estimation was determined. Specific discussion of these tables is given in the relevant sections to follow.

Table 5-I. Simulation results for Dose Area Product.

Metric	*Weighting*	*Table*	*Slope*	R^2
Time	Even	auto	0.73	0.964
	Even	fixed	0.73	0.954
	Weighted	auto	0.73	0.964
	Weighted	fixed	0.73	0.955
DAP	Even	auto	0.75	0.990
	Even	fixed	0.75	0.990
	Weighted	auto	0.75	0.990
	Weighted	fixed	0.75	0.990
Dose	Even	auto	0.75	0.987
	Even	fixed	0.75	0.986
	Weighted	auto	0.75	0.987
	Weighted	fixed	0.74	0.986

Table 5-II. Simulation results for maximum dose.

Metric	*Weighting*	*Table*	*Slope*	R^2
Time	Even	auto	1.002	0.867
	Even	fixed	0.93	0.806
	Weighted	auto	0.95	0.833
	Weighted	fixed	0.87	0.706
DAP	Even	auto	1.06	0.939
	Even	fixed	1.01	0.899
	Weighted	auto	1.00	0.909
	Weighted	fixed	0.94	0.815
Dose	Even	auto	1.07	0.937
	Even	fixed	0.99	0.893
	Weighted	auto	1.01	0.917
	Weighted	fixed	0.92	0.806

5.2.2 Dose Area Product

Dose area product was fairly invariant on the choice of parameters used (Table 5-I). However the DAP based estimation produced the best results, regardless of table height and weighting. This is a positive result as it is expected that table height and weighting distribution should have no effect on the DAP. Estimation based on fluoro time was the least precise. The chosen model was based on DAP fluoroscopic estimation with automatic table height calculation and even weighting. The comparison with film measurements is shown in Figure 5.5 with ± 15% error bars based on uncertainty estimations detailed in Chapter 3. The results show a high correlation between simulation and films (R^2 = 0.990). The slope of the fit is 0.754 meaning that on average the simulated DAP was 24.6% lower than the film DAP.

5.2.3 Maximum Dose

Maximum dose plots showed slopes of 0.87 – 1.07 and a best slope of 1.0 indicating that simulations provided estimates that on average were well matched to film measurements. Having already chosen the DAP based metric based on the above results the search was narrowed down to the DAP metric for maximum dose also. It was decided that R^2 was a more important parameter than slope as the best correlation possible between film and simulation was sought. As a result of these considerations the DAP metric with even distribution and automatic table height calculation were used. Simulations versus film measurements for maximum skin dose are shown in Figure 5.6 with ± 15% error bars. Estimated maximum skin dose was highly correlated with film measurements (R^2 = 0.939) with a slope of 1.06. Maximum skin dose was predicted to within 50% for all patient's and within 30% for 65% of patient's.

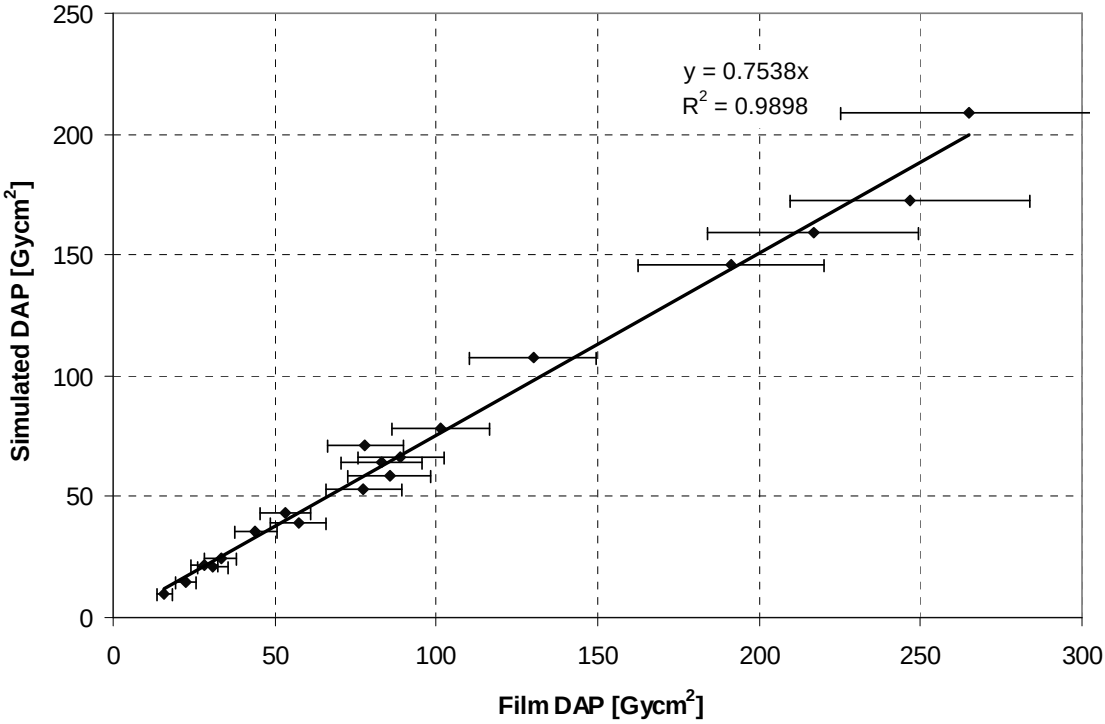

Figure 5.5. Simulated versus film results for Dose Area Product based on DAP fluoroscopic estimation with even weighting and automatic table height.

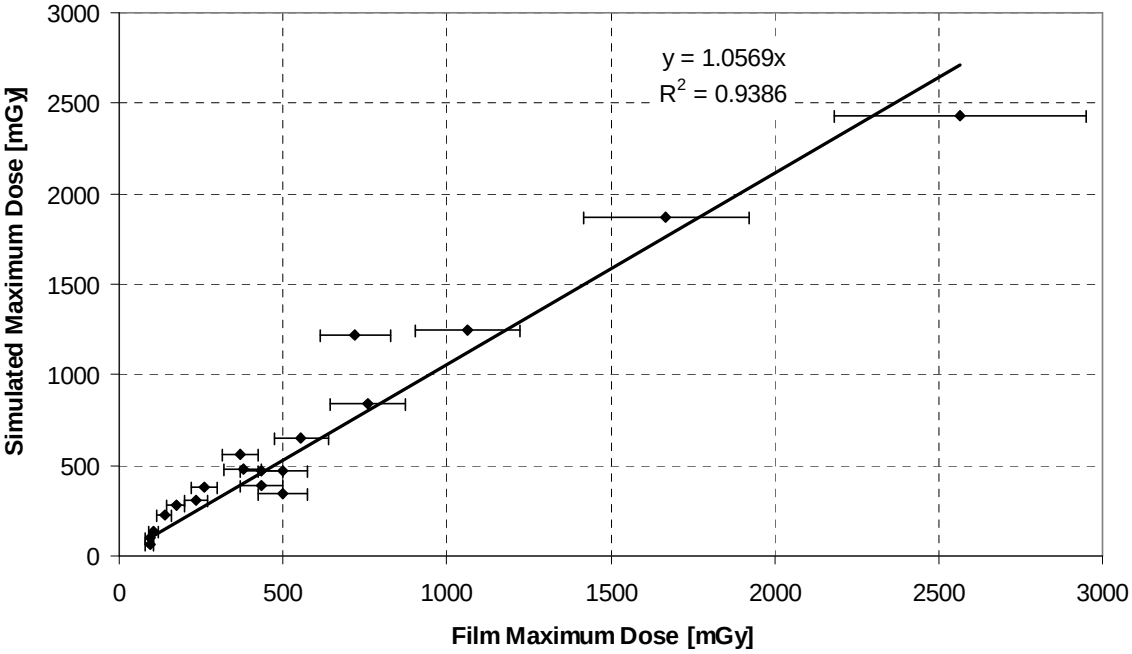

Figure 5.6. Film versus simulation results for maximum skin dose based on DAP fluoroscopic estimation with even weighting and automatic table height.

5.2.4 Geometrical Accuracy

From section 5.2.3 it is known that the model is capable of predicting the magnitude of maximum dose with reasonable accuracy. Equally important is the ability to localise the region of high dose. Simulations and corresponding films were visually inspected for comparison. If the region of highest dose in the simulation was within an arbitrary 5 cm of the highest dose on the film, then the simulation was scored as a success. Results where the maximum dose was ~5 cm or perhaps within 5 cm but for the wrong reason e.g. field overlap was not the same, were scored as marginal. The results of this scoring are shown in Table 5-III. One film had insufficient exposure to be accurately inspected and was scored N/A.

Table 5-III. Geometrical accuracy of simulations.

Yes	*Marginal*	*No*	*N/A*
9	6	3	1

The total number of definitively located doses was 9/18 = 50%. If the standards were relaxed to include marginal results then 83% of simulations were able to locate the region of maximum dose to some degree. This leaves 17% of studies where the localisation was incorrect. Possible reasons for this discrepancy are considered in the discussion section.

Of particular interest is the patient who received a maximum skin dose of 2564 mGy. Their film and simulation geometries are shown in Figure 5.7. It can be seen that the area of maximum dose is well predicted for this patient. Also of note is the small offset of the region of maximum dose in the film. This is a good example where panning was used and the table position modified slightly during the procedure. The simulated maximum dose was 2431 mGy, 5.2% less than the film measurement. Some other examples of successful localisations are shown inFigure 5.8.

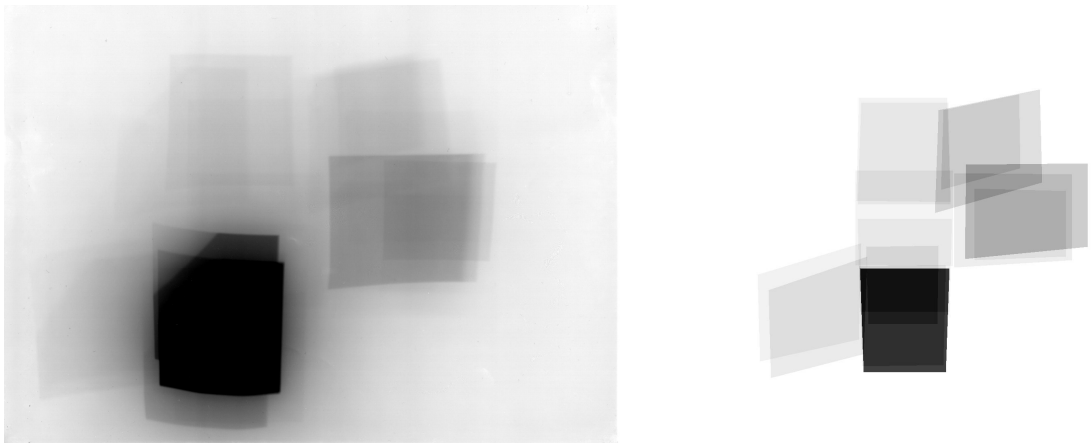

(a) (b)

Figure 5.7. Patient who received 2,400 mGy. a) Film. b) Simulations.

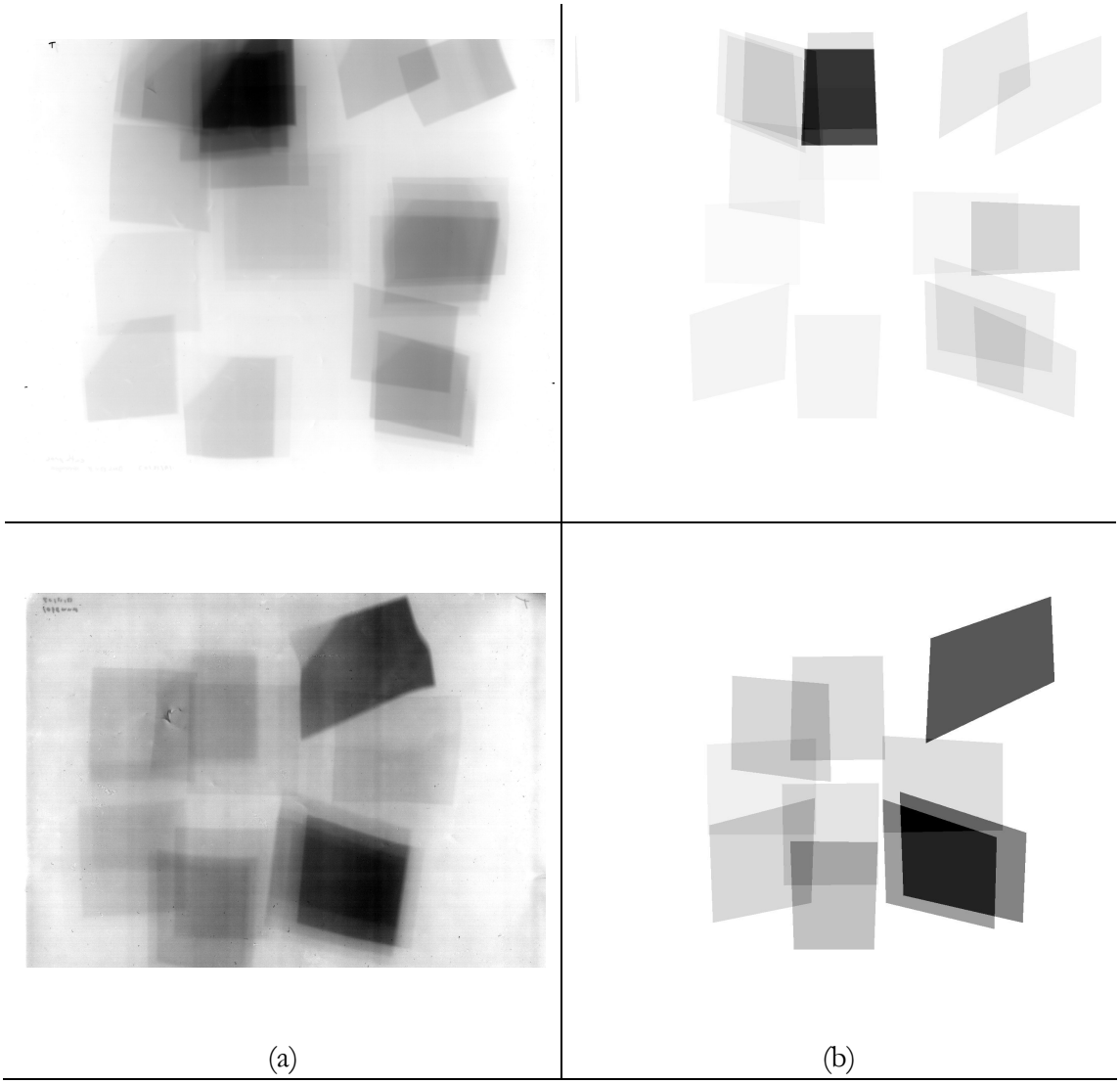

Figure 5.8. Successful localisation of maximum doses for two patient's, a) Films. b) Simulations.

5.3 Trends

The collection of maximum dose measurements that are otherwise unavailable enables some useful analysis. Here some comparisons are presented which may be of particular use to the clinician and physicist alike.

5.3.1 Maximum dose and DAP

The relationship between DAP and maximum skin dose is of great interest as the machine only reports DAP while the maximum skin dose is often the quantity of greater importance. From the scatter plot shown in Figure 5.9 it can be seen that there is a positive trend relating DAP to maximum dose, i.e., a higher DAP will generally result in a higher maximum skin dose. The Pearson correlation R between them is R = 0.76. Note however the final two data

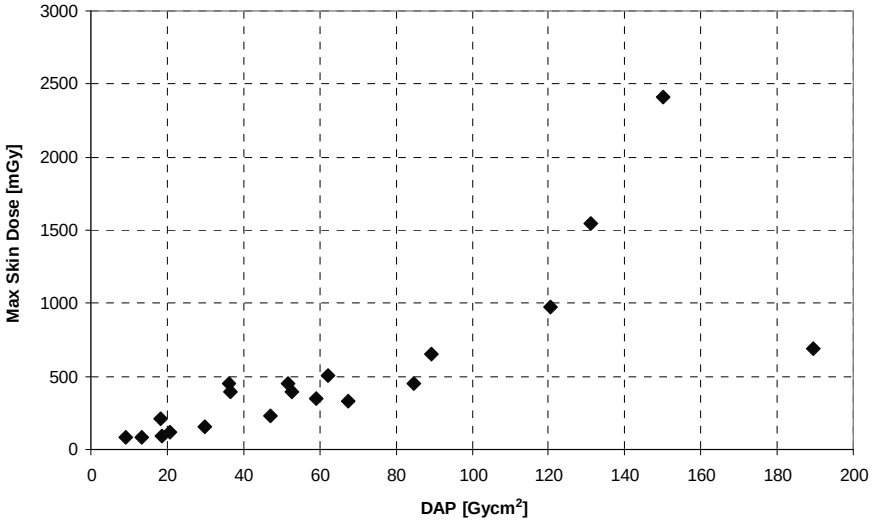

Figure 5.9. Maximum skin dose versus reported dose area product.

points where one has a greater DAP but a much lower maximum dose than the other. Therefore while DAP has some relation to maximum skin dose, it is by no means a consistent and reliable relationship.

5.3.2 Fluoroscopic time and maximum dose

More complex procedures inevitably end up with longer fluoroscopic times. In addition fluoroscopic time can increase dramatically with tortuous vessels and less experienced cardiologists. It should be expected that maximum dose and fluoroscopic time will have a strong correlation. Figure 5.10 shows this relationship for the patient's in this study. The Pearson correlation between the two is R = 0.82. As expected an increase in fluoro time on average leads to an increase in maximum dose. However as with DAP, the points vary significantly. Therefore fluoroscopic time is also not a reliable indication of maximum dose.

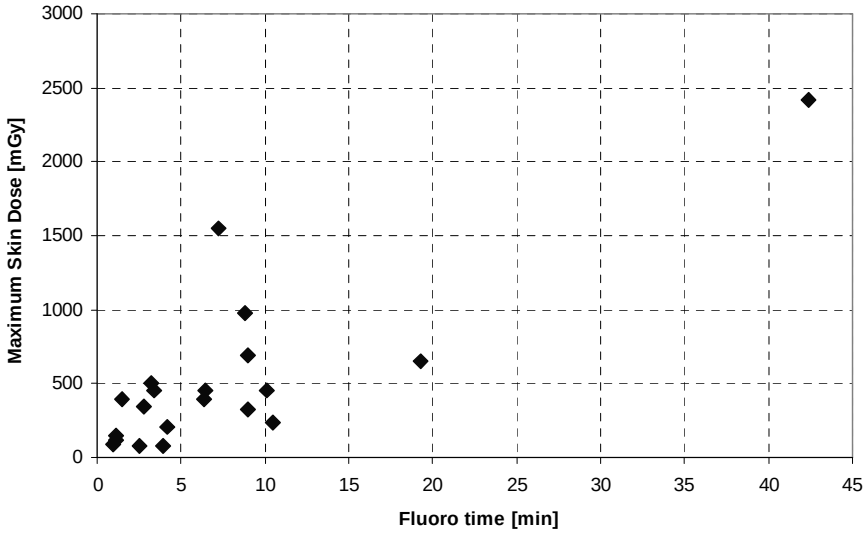

Figure 5.10. Maximum skin dose versus fluoroscopic time.

5.4 Discussion

In this chapter the dose area product and maximum skin dose have been calculated using radiochromic films and compared to simulations based on exposure information. The estimation of maximum skin dose was especially promising with reasonable accuracy and precision. While the dose area product estimation showed high precision ($R^2 = 0.990$), it under predicted doses by ~25% compared with film measurements.

5.4.1 Comparison to other works

These results are significantly better than Morrell and Rogers were able to achieve due to several limitations in their study [25]. It should be noted that in their work only maximum dose was measured, no estimate was made of dose area product. There are three significant differences between their methods and the ones used in this work:

1. *Film*

In their study Morrell and Rogers used Kodak EDR2 (Extended Dose Range) radiographic film. Being a radiographic film its response is vastly different than the Gafchromic® XR-RV2 film used in this study. The EDR2 film saturates at around 1 Gy therefore films which showed saturation had to be excluded from their study. The uncertainties they estimated were -18% + 39% at 160 mGy and increasing uncertainties beyond 160 mGy [76,77]. From the work presented in this thesis it is clear that the Gafchromic® XR-RV2 is a superior film for this application with 1σ uncertainties estimated as ±15% in the dose region of 200 – 5000 mGy (Figure 3.19). It can handle a far greater dose range and by following the scanning protocol presented can also achieve lower uncertainties.

2. *Dose Measurement*

In their study a dose area product meter was not available. Therefore dose calculation was based on kV and mA response curves. This indirect method is inherently less accurate than a direct measurement such as a DAP meter. KV and mA measurements would usually be considered a more universal method as many older machines do not have DAP meters or at least do not include such information in the DICOM files. However, as was discovered in this work, modern machines using adaptive filtering are unsuitable for this method and must rely on the more accurate DAP readings.

In addition, backscatter was measured and included directly by placing Perspex slabs in the beam and dose measurements taken at the entrance surface using an ion chamber. Backscatter was excluded deliberately due to the nature of the solid state dosimeter used. The solid state

detector has a thin lead backing to reduce backscatter and it was thought best to make measurements in the absence of backscatter altogether.

3. *Geometry*

The reconstruction approach used in this work is very similar to that of Morrell and Rogers. It is interesting to note that the example they demonstrated in their paper seems to be missing beam deformation in one direction, indicating a missing degree of freedom. However it is not possible to confirm this from one example only.

To summarise, it was a combination of appropriate films and a more direct dose estimation that lead to better results than Morrell and Rogers.

5.4.2 Fluoroscopic time and its effect on the accuracy of simulations

As the dose contribution from fluoroscopy must be estimated it might be expected that simulation of PTCA procedures would result in greater errors than C/Angio due to the increased use of fluoroscopy for PTCA. To discover if this was true the best simulation results (DAP based, even weighting and auto table height) were split into C/Angio and PTCA groups and plotted against film measurements with a linear fit via a least squares method. Table 5-IV shows the fitting results for DAP and maximum dose. The total DAP is again relatively unaffected by procedure type. The maximum dose however actually shows some small improvement in PTCA estimation over C/Angio. The difference is most likely statistical in nature. However a possible explanation is that this is due to the increased dose resulting in better signals for film measurements and thus more reliable readings. These results indicate that PTCA simulations are likely capable of achieving similar accuracy to C/Angio.

Table 5-IV. Summary of fits for DAP and maximum dose based on procedure type.

Measure	*Exam*	*Slope*	R^2
DAP	C/Angio	1.27	0.993
	PTCA	1.35	0.989
Max dose	C/Angio	0.91	0.880
	PTCA	0.92	0.936

After the above results showed that PTCA simulations were at least comparable to C/Angio it was decided to look directly at how fluoro time affected deviations between film and simulations. Figure 5.11 shows the deviation in maximum dose between film and simulation as a function of fluoroscopic time. It can be seen that the deviations appear to be scattered around –10% and no obvious trend is observed. The -10% offset indicates a systematic error and is consistent with the under-prediction of simulation doses discussed

previously. Thus with the current simulations, fluoro time does not appear to be a limiting factor.

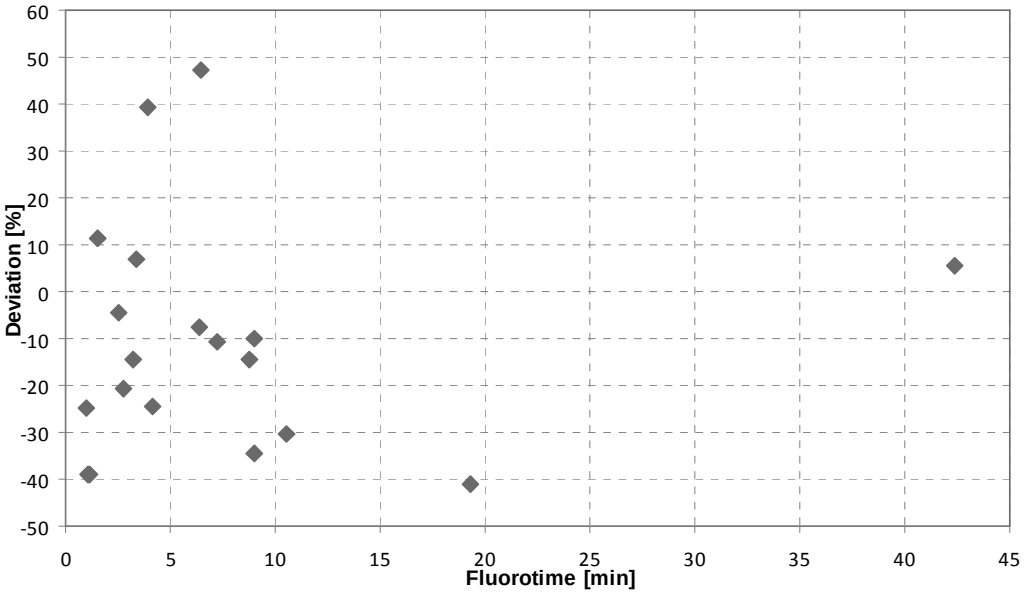

Figure 5.11. Deviation between film and simulation for maximum skin dose measurements as a function of fluoroscopic time.

5.4.3 Limitations

Film Dosimetry

Placement of films such that they intercepted all the beams proved to be a challenging task. Although films were taped to the table, some movement still occurred for a few patients. Attempts were made to align the film with the patients shoulders but were not always successful due to the ill health of some patients. Interception of beams was usually better in one orientation than the other due to the rectangular shape of the film. It was found that the lateral angulations produced the greatest variation in beam position therefore best results were achieved when the film was placed with the long edge running from the patients left to right side.

In addition to film movement and difficulties in placement, the film was occasionally damaged by patients. For example when the patient lay down on their elbows first and indented the film into the soft mattress supporting the film producing large creases in the film. Film exhibiting such damage had to be manually edited before automatic dose calculation to remove erroneous pixel values. Such editing of course obscures the true dose and thus adds uncertainty to the calculated doses.

Simulations

Two significant limitations were identified in this study relating to the reconstruction. The first, collimation, was highlighted as a deficiency under the simulations chapter and is not repeated here. The second severe limitation is table movement. Not only is vertical table movement only indirectly recorded via the SPD, but the horizontal movement is not recorded at all. Horizontal table movement, often referred to as panning, is a significant part of many cardiac catheterisation procedures. While this movement may not affect the DAP, it can have an effect on maximum skin dose and geometrical accuracy of simulations.

It had been assumed that the patients back lies flush with the table over the range of angulations encountered. While this is a valid assumption for the examinations encountered in this thesis, it is obvious that lateral projections cannot be used with the current flat table model. To account for larger angulations would require that the fields be projected back onto a patient shaped 3D surface and not the flat table top used in this study.

6. Conclusions and Future Work

6.1 Conclusions

In this thesis patient exposures have been simulated using stored acquisition information. The results were compared with radiochromic film exposures placed at the patient's back. The results produced greater accuracy than previous work in the field [25]. The results achieved indicate that simulation based on DICOM acquisition files is a valid and reasonably accurate method for predicting maximum skin dose provided sufficient information is available.

Film

The use of radiochromic film for dosimetry is a significant task with numerous papers devoted solely to this topic. In order to get the best results one must fully understand the characteristics of the particular film used. In Chapter 3 these characteristics were investigated for Gafchromic® XR-RV2 film.

The characteristics of Gafchromic® XR-RV2 were investigated as there had been no peer reviewed literature on this film at the time of writing. Its usable dose range was ~20 mGy to < 20000 mGy with an energy dependence of ± 15% between 60 and 125 kVp at 1 Gy. A protocol was developed for scanning Gafchromic® XR-RV2 on a flatbed RGB document scanner. Using this protocol it was possible to achieve uncertainties of ± 10% over a dose range of 500 - 1500 mGy. The Gafchromic® XR-RV2 film turned out to be a highly suitable film for the task. It was capable of measuring the range of doses encountered, from ~20 mGy up to 2564 mGy. Although the films are designed to be especially large, on some patients there were missing or cut-off radiation fields due to either the film still not being large enough to accept all incident beam angles, or the patient displacing the film as they lay down.

Simulations

A software program was created to load in a set of study files in DICOM format, receive additional fluoroscopic parameters from the user, and then provide a visual dose distribution and a summary of dose information. The simulations showed positive results for measurement of dose area product and maximum skin dose. The best fluoroscopic estimation was based on records of dose area product collected from the machine's Diamentor™ DAP meter. With this method maximum skin dose was predicted to within ± 50% for all patients and within ± 30% for 65% of patients. Although this does not appear to be a numerically promising result,

the ability to predict even close to the true maximum dose is valuable and a significant improvement over what is currently available. The Pearson correlation (R) between film and simulations for DAP and maximum skin dose were 0.995 and 0.969 respectively. In addition the location of maximum dose was conclusively predicted in 50% of cases and generally located in 83% of patients. There were still three (17%) patients that the simulation was unable to predict the location of maximum dose for. Limitations with the simulation include incorrectly calibrated collimator positions and table height, as well as the lack of horizontal table movement.

To conclude, a simulation model has been developed capable of predicting maximum skin dose. The model was able to identify the location of maximum skin dose for 83% of patients and provides a significant improvement over what is currently available. As a result this software will be used by the Medical Physics and Bioengineering department and developed so that it can be used by clinicians in the hospital.

6.2 Future work

Due to the success of the simulation model the software will be developed into a standalone program for use by the Medical Physics and Bioengineering department. The hope is that it will develop sufficiently to be used by radiographers and clinicians in cardiology. To turn this into a reality will require the following:

1. Several modifications can be made to streamline the calculations and provide more robust user input. The machine table height and collimator position need to be correctly calibrated by the manufacturer so that this information can be used without the need for corrections.

2. In order to achieve the most accurate simulations the horizontal table position must be known. This information is almost certainly available to the machine and it is incumbent upon the manufacturer to make this information available in the DICOM files. Once this is known, it opens up the possibility of having a 3D patient model capable of simulating lateral exposures. To get around this lack of information an alternative would be to use a tracking device located on the table to provide external table coordinates.

3. Once the table movement was available it would then be useful to have the information available in real time to the operator. This could be achieved by installing the software on the host computer and having it automatically read the acquisition files stored.

References

[1]DeFrances C, Cullen K A, and Kozak L J, Report No. Vital Health statistics 13 (169), National Hospital Discharge Survey: 2005 Annual Summary With Detailed Diagnosis and Procedure Data, 2007. National Center for Health Statistics,

[2]Poloniecki J, Valencia O, and Littlejohns P, "Cumulative risk adjusted mortality chart for detecting changes in death rate: observational study of heart surgery" British Medical Journal. **316**, 1697-1700 (1998).

[3]Chandrasekar B, Doucet S, Bilodeau L et al., "Complications of cardiac catheterization in the current era: A single-center experience" Catheterization and Cardiovascular Interventions. **52**, 289-295 (2001).

[4]Röntgen W C, "On a New Kind of Rays" Würzburg Physical and Medical Society. (1895).

[5]*Nobel Lectures.* (Elsevier Publishing Company, Amsterdam, 1967).

[6]Patton D, "Roentgen and the New Light - Roentgen's Moment. Part 3: The genealogy of Roentgen's Barium Platinocyanide Screen" Investigative Radiology. **28**, 954-961 (1993).

[7]Dam H J W, "The New Marvel in Photography" McClure's Magazine. **6**, 403-415 (1896).

[8]Eisenberg R L, *Radiology: An Illustrated History.* (Mosby Year book, St. Louis, 1992).

[9]APS, American Physical Society, First X-ray, http://pre.aps.org/50years/timeline, Accessed: 23/01/09.

[10]Imaginis, Milestones in Medical Diagnosis and Diagnostic Imaging, http://www.imaginis.com/faq/milestones.asp, Accessed: 23/01/09.

[11]Forssmann W, "Die sondierung des rechten Herzens" Klin Wschr. **78**, 2085-2087 (1929).

[12]ICRP, ICRP Publication 103: Recommendations of the ICRP, 2008. International Commission on Radiological Protection, Ottawa.

[13]Granel F, Barbaud A, Gillet-Terver M N et al., "Radiodermites chroniques après cathétérisme interventionnel cardiaque: quatre observations." Annales de Dermatologie et de Venereologie. **125**, 405–407 (1998).

[14]Dandurand M, Huet P, and Guillot B, "Radiodermites secondaires aux explorations endovasculaires: 5 observations." Annales de Dermatologie et de Venereologie. **126**, 413–417 (1999).

[15]McParland B J, "A study of patient radiation doses in interventional radiological procedures" British Journal of Radiology. **71**, 175-185 (1998).

[16]Vano E, Arranz L, Sastre J M et al., "Dosimetric and radiation protection considerations based on some cases of patient skin injuries in interventional cardiology" British Journal of Radiology. **71**, 510-516 (1998).

[17]Padovani R, Evaluation of the risk of deterministic effects in cardiology, DIMOND Consortium, Europe.

[18]Wagner L K, McNeese M D, Marx M V et al., "Severe Skin Reactions from Interventional Fluoroscopy: Case Report and Review of the Literature" Radiology. **213**, 773-776 (1999).

[19]Wagner L K, Archer B R, and Cohen A M, "Management of Patient Skin Dose in Fluoroscopically Guided Interventional Procedures" Journal of Vascular and Interventional Radiology. **11**, 25-33 (2000).

[20]Padovani R and Quai E, "Patient dosimetry approaches in interventional cardiology and literature dose data review" Radiation Protection Dosimetry. **117**, 217-221 (2005).

[21]Vano E, Goicolea J, Galvan C et al., "Skin radiation injuries in patients following repeated coronary angioplasty procedures" British Journal of Radiology. **74**, 1023-1031 (2001).

[22]Vano E, Prieto C, Fernandez J M et al., "Skin dose and dose-area product values in patients undergoing intracoronary brachytherapy" British Journal of Radiology. **76**, 32-38 (2003).

[23]SKUT, PCXMC Dose Calculations (STUK Radiation and Nuclear Saftey Authority, Helsinki, 2004).

[24]den Boer A, de Feijter P J, Serruys P W et al., "Real-Time Quantification and Display of Skin Radiation During Coronary Angiography and Intervention" Circulation. **104**, 1779-1784 (2001).

[25]Morrell R E and Rogers A T, "A mathematical model for patient skin dose assessment in cardiac catheterization procedures" British Journal of Radiology. **79**, 756-761 (2006).

[26]Johns H E C, John R., *The Physics of Radiology*, Fourth Edition ed. (Charles C Thomas, Springfield, 1983).

[27]Khan F M, *The physics of radiation therapy*, 3rd ed. (Lippincott Williams & Wilkins, Philadelphia, 2003).

[28]Nowotny R, XMuDat: photon attenuation data (Univ. Wien, AKH-4L, Austria).

[29]McNair A, Report No. 1099-1344, ICRU Report 33 - Radiation Quantities and Units Pub: International Commission on Radiation Units and Measurements, Washington D.C. USA issued 15 April 1980, pp.25, 1981.

[30]Loevinger R, "A formalism for calculation of absorbed dose to a medium from photon and electron beams" Medical Physics. **8**, 1-12 (1981).

[31]Hall E J and Giaccia A J, *Radiobiology for the Radiologist*. (Lippincott Williams & Wilkins, Philadelphia 2006).

[32]Brooks A L, "Paradigm shifts in radiation biology: Their impact on intervention for radiation-induced disease" Radiation Research. **164**, 454-461 (2005).

[33]Hopewell J W, "Mechanisms of the Actions of Radiation on Skin and Underlying Tissues" British Journal of Radiology. **19**, 39-51 (1986).

[34]Koenig T R, Wolff D, Mettler F A et al., "Skin Injuries from Fluoroscopically Guided Procedures: Part 1, Characteristics of Radiation Injury" American Journal of Roentgenology. **177**, 3-11 (2001).

[35]Curry T S, Dowdey J E, and Murry R C J, *Christensen's Physics of Diagnostic Radiology*, 4th ed. (Williams & Wilkins, 1990).

[36]Azam N-R, Blackwell C R, Coursey B M et al., "Radiochromic film dosimetry: Recommendations of AAPM Radiation Therapy Committee Task Group 55" Medical Physics. **25**, 2093-2115 (1998).

[37]Butson M J, Yu P K N, Cheung T et al., "Radiochromic film for medical radiation dosimetry" Materials Science and Engineering: Reports. **41**, 61-120 (2003).

[38]Soares C G, "Radiochromic film dosimetry" Radiation Measurements. **41**, S100-S116 (2006).

[39]Kosar J, *Light-Sensitive Systems.* (Wiley, New York, 1965).

[40]Saylor M C, Tamargo T T, McLaughlin W L et al., "A thin film recording medium for use in food irradiation" International journal of radiation Applications and Instrumentation. Part C. Radiation Physics and Chemistry. **31**, 529-536 (1988).

[41]Rampado O, Garelli E, Deagostini S et al., "Dose and energy dependence of response of Gafchromic® XR-QA film for kilovoltage x-ray beams" Physics in Medicine and Biology. **51**, 2871-2881 (2006).

[42]G. Thomas R Y L C, Frank Rabe, "A study of GafChromic XR Type R film response with reflective-type densitometers and economical flatbed scanners" Journal of Applied Clinical Medical Physics. **4**, 307-314 (2003).

[43]Cheung T, Butson M, and Yu P K N, "Experimental energy response verification of XR type T radiochromic film" Physics in Medicine and Biology. **49**, N371-N376 (2004).

[44]Klassen N V, van der Zwan L, and Cygler J, "GafChromic MD-55: Investigated as a precision dosimeter" Medical Physics. **24**, 1924-1934 (1997).

[45]ISP Corp W-N J, USA, ISP Corp, Wayne - New Jersey , USA, Summary of GAFCHROMIC radiotherapy film products, http://online1.ispcorp.com/_layouts/Gafchromic/content/home/radiotherapy.html, Accessed: 08/12/2008.

[46]Rink A, Vitkin I A, and Jaffray D A, "Characterization and real-time optical measurements of the ionizing radiation dose response for a new radiochromic medium" Medical Physics. **32**, 2510-2516 (2005).

[47]Fuss M, Sturtewagen E, Wagter C D et al., "Dosimetric characterization of GafChromic EBT film and its implication on film dosimetry quality assurance" Physics in Medicine and Biology. **52**, 4211-4225 (2007).

[48]Dempsey J F, Low D A, Mutic S et al., "Validation of a precision radiochromic film dosimetry system for quantitative two-dimensional imaging of acute exposure dose distributions." Medical Physics. **27**, 2462-2475 (2000).

[49]Chiu-Tsao S-T, Duckworth T, Zhang C et al., "Dose response characteristics of new models of GAFCHROMIC films: Dependence on densitometer light source and radiation energy" Medical Physics. **31**, 2501-2508 (2004).

[50]Devic S, Jan S, Edwin S et al., "Precise radiochromic film dosimetry using a flat-bed document scanner" Medical Physics. **32**, 2245-2253 (2005).

[51]Giles E R and Murphy P H, "Measuring skin dose with radiochromic dosimetry film in the cardiac catheterization laboratory" Health Physics. **82**, 5 (2002).

[52]Canne S d, Carosi A, Bufacchi A et al., "Use of GAFCHROMIC XR type R films for skin-dose measurements in interventional radiology: Validation of a dosimetric procedure on a sample of patients undergone interventional cardiology" Physica Medica. **22**, 105-110 (2006).

[53]Thomas G, Li Y, Chu R Y L et al., "Measurement of Dose-Area Product with GafChromic XR Type R Film" Journal of Applied Clinical Medical Physics. **6**, 11 (2005).

[54]Dini S A, Meigooni A S, Koona R A et al., "Dosimetric evaluation of GAFCHROMIC® XR type T and XR type R films" Journal of Applied Clinical Medical Physics. **6**, 21 (2005).

[55]Devic S, Seuntjens J, Hegyi G et al., "Dosimetric properties of improved GafChromic films for seven different digitizers" Medical Physics. **31**, 2392-2401 (2004).

[56]Aydarous A S, Darley P J, and Charles M W, "A wide dynamic range, high-spatial-resolution scanning system for radiochromic dye films" Physics in Medicine and Biology. **46**, 1379-1389 (2001).

[57]Alva H, Mercado-Uribe H, Rodriguez-Villafuerte M et al., "The use of a reflective scanner to study radiochromic film response" Physics in Medicine and Biology. **47**, 2925-2933 (2002).

[58]Mersseman B and Wagter C D, "Characteristics of a commercially available film digitizer and their significance for film dosimetry" Physics in Medicine and Biology. **43**, 1803-1812 (1998).

[59]Lewis D F, Performance of the Vidar® Red LED Dosimetry Pro Advantage™: A scanner optimized for use with GAFCHROMIC® EBT Dosimetry Film., International Specialty Products, Wayne, NJ.

[60]Zhu Y, Kirov A S, Mishra V et al., "Quantitative evaluation of radiochromic film response for two-dimensional dosimetry" Medical Physics. **24**, 223-231 (1997).

[61]McLaughlin W L, "A Radiochromic Solid-State Polymerization Reaction" Abstracts of Papers of the American Chemical Society. **208**, (1994).

[62]Rasband W S, ImageJ (U. S. National Institutes of Health, http://rsb.info.nih.gov/ij/, Bethesda, Maryland, USA, 1997-2007).

[63]McLaughlin W L, Yun-Dong C, Soares C G et al., "Sensitometry of the response of a new radiochromic film dosimeter to gamma radiation and electron beams" Nuclear Instruments and Methods in Physics Research Section A: Accelerators, Spectrometers, Detectors and Associated Equipment. **302**, 165-176 (1991).

[64]Meigooni A S, Sanders M F, Ibbott G S et al., "Dosimetric characteristics of an improved radiochromic film" Medical Physics. **23**, 1883-1888 (1996).

[65]Saur S and Frengen J, "GafChromic EBT film dosimetry with flatbed CCD scanner: A novel background correction method and full dose uncertainty analysis" Medical Physics. **35**, 3094-3101 (2008).

[66]ISP Corp, Wayne - New Jersey , USA, http://online1.ispcorp.com/_layouts/Gafchromic/content/home/diagradio.html, Accessed: 4/12/08.

[67]DICOM, Introduction and Overview (National Electrical Manufacturers Association, 2007), Vol. PS 3.1.

[68]DICOM, Data Structures and Encoding (National Electrical Manufacturers Association, 2007), Vol. PS 3.5.

[69]DICOM, Media Storage and File Format for Media Interchange (National Electrical Manufacturers Association, 2007), Vol. PS 3.10.

[70]Fletcher D W, Miller D L, Balter S et al., "Comparison of Four Techniques to Estimate Radiation Dose to Skin During Angiographic and Interventional Radiology Procedures" Journal of Vascular and Interventional Radiology. **13**, 391-397 (2002).

[71]Lin P-J P, "The operation logic of automatic dose control of fluoroscopy system in conjunction with spectral shaping filters" Medical Physics. **34**, 3169-3172 (2007).

[72]ICRU, Report No. 44, Tissue Substitutes in Radiation Dosimetry and Measurement 1989. International Commission on Radiation Units and Measurements, Bethesda.

[73]Petoussi-Henss N, Zankl M, Drexler G et al., "Calculation of backscatter factors for diagnostic radiology using Monte Carlo methods" Physics in Medicine and Biology. **43**, 2237-2250 (1998).

[74]Kölling M, BlueJ - Interactive Java Environment (Deakin University, Melbourne, 2008).

[75]Clunie D, PixelMed Java DICOM Toolkit, www.dclunie.com/pixelmed/software/, Accessed: 12/12/08.

[76]Morrell R E and Rogers A T, "Calibration of Kodak EDR2 film for patient skin dose assessment in cardiac catheterization procedures" Physics in Medicine and Biology. **49**, 5559-5570 (2004).

[77]Morrell R E and Rogers A T, "Kodak EDR2 film for patient skin dose assessment in cardiac catheterization procedures" British Journal of Radiology. **79**, 603-607 (2006).

The following publications and presentations have arisen from this work:

Blair A and Meyer J, "Characteristics of Gafchromic® XR-RV2 Radiochromic Film", Medical Physics (Submitted Feb 2009).

Blair A "Characteristics of Gafchromic® XR-RV2" Poster presentation. EPSM-ABEC 2008.

Blair A. "Skin dose assessment in cardiology" APSEM Conference proceedings, EPSM-ABEC 2007.

Appendix I

Selected Source Code

File reader

```
import java.io.*;
import java.util.Vector;

/**
 * A class for reading DICOM files
 * Will read through a file input stream and pickout attribute tags and store them into a HashTable.
 * @author Andrew Blair
 * @version 1.0 Dec 2008
 */

public class File_Reader extends BufferedInputStream
{
   BufferedInputStream file;
   DataSet dataElements = new DataSet();
   TransferSyntax syntaxToReadMeta = new TransferSyntax("1.2.840.10008.1.2.1"); // Default syntax
   TransferSyntax syntaxToReadData;
   TransferSyntax currentSyntax;
   DicomDictionaryBase myDictionary = new DicomDictionary();
   long metaLength = 0L;
   byte[] buffer4Bytes = new byte[4];
   byte[] buffer2Bytes = new byte[2];


   public File_Reader(String file_name) throws IOException {
   super( new BufferedInputStream(new FileInputStream(file_name)));
}

      public void findDicomDetails() throws IOException {
         byte[] undefinedLength = {-1,-1,-1,-1}; // an FFFF unsigned int in signed form
         String undefinedLengthTest = new String(undefinedLength);
         byte[] groupLengthTest = {0,2,0,0};
         AttributeTag metaLengthTag = new AttributeTag(0x0002,0x0000);
         AttributeTag currentTag;
         DataElement currentElement =null;
         currentSyntax = syntaxToReadMeta;
         boolean completedSearch = false;
         long index = -1;
         skip(128);
         read(buffer4Bytes,0,4);
         if(new String(buffer4Bytes,0,4).equals("DICM")){
            //System.out.println("We found a Dicom file!");
            /**
             * Here we know we have a DICOM file and we want to read the META to find the syntax of * the main  data set.
             For initial version I have assumed Explicit VR little endian to read the   * META.
          */
            while(completedSearch == false){

            if(pos == 16){
             metaLength = unsignedByteToLong ((byte[])(dataElements.getElement(metaLengthTag)).getValueField());
            }
            if(pos < (metaLength+16) ){
               currentSyntax = syntaxToReadMeta;
            }
            if(pos >= (metaLength + 16) && syntaxToReadData ==null){
             syntaxToReadData = new TransferSyntax(new String ((byte[]) (dataElements.getElement(new AttributeTag
             (0x0002,0x0010))).getValueField()));
             if(syntaxToReadData.getDescription().equals(new String("Unrecognized"))){
              int syntaxLength = (int)dataElements.getElement(new AttributeTag(0x0002,0x0010)).getVL();
           syntaxToReadData = new TransferSyntax(new String((byte[])
             (dataElements.getElement(new AttributeTag(0x0002,0x0010))).getValueField(),0,syntaxLength-1));
           }
               currentSyntax = syntaxToReadData;
               dataElements.setTransferSyntax(syntaxToReadData);
```

```
    }

        // Read the first tag (4 bytes) and create an AttributeTag for them
        read(buffer4Bytes,0,4);
        // Check to see that we have gone as far as we want to, in this case the group 0x6000
                if(unsignedByteToSignedByte(reorderBytesTwoWords(currentSyntax,buffer4Bytes),4)[1] > 0x60 ||
      count == 0){
            close();
            completedSearch = true;
            break;
        }
      currentTag =
      makeTag(unsignedByteToSignedByte(reorderBytesTwoWords(currentSyntax,buffer4Bytes),4),syntaxToReadMet
      a);
        // Make a new entry for this tag
        dataElements.putDataElement(currentTag, new DataElement(currentTag));
        currentElement = dataElements.getElement(currentTag);
        currentElement.setName(myDictionary.getNameFromTag(currentTag));

        // Find VR
        if(currentSyntax.isExplicitVR()){
            read(buffer2Bytes,0,2);
            byte[] vRBytes = {buffer2Bytes[0],buffer2Bytes[1]};
            currentElement.setVR(vRBytes);
        }
        else{
            if(currentTag.isPrivate()){
                currentElement.setVR(ValueRepresentation.UN);
            }
            else{
                    currentElement.setVR(myDictionary.getValueRepresentationFromTag(currentTag));
            }
        }

                // If VL is definite and only 2 bytes
                 if( currentSyntax.isExplicitVR() &&
                 ValueRepresentation.isShortValueLengthVR(reorderBytesOneWord(currentSyntax,buffer2Bytes,2))){
                   read(buffer2Bytes,0,2);
                  currentElement.setVL(unsignedByteToInt(reorderBytesOneWord(currentSyntax,buffer2Bytes,2)));
                   byte[] valueField = new byte[(int)currentElement.getVL()];
                   read(valueField,0,(int)currentElement.getVL());
                   currentElement.setValueField(valueField);
                }

                else {  // Else VL is 4 Bytes
                   if(currentSyntax.isExplicitVR()){ // Skip 2 bytes if VR is explicit
                      skip(2);
                   }
                   read(buffer4Bytes,0,4);

                  currentElement.setVL(unsignedByteToLong(reorderBytesOneWord(currentSyntax,buffer4Bytes,4)));

                    // If VL length is given
                            if(! new String(undefinedLengthTest).equals(new
                            String(reorderBytesOneWord(currentSyntax,buffer4Bytes,4)))){
                      byte[] valueField = new byte[(int)currentElement.getVL()];
                      read(valueField,0,(int)currentElement.getVL());
                      currentElement.setValueField(valueField);
                    }
                            else{   // Undefined length, put each byte into a Vector while looking for the Sequence
                            Delmination Item
                      readSequence();
                    }

                } // End of VL 4 Bytes loop
        } // End of While Meta Loop
      } // End of Initial test for finding DICM
    } // End of method


public AttributeTag makeTag(int[] b,TransferSyntax TS){
    int msGroupByte;
    int lsGroupByte;
    int msElementByte;
    int lsElementByte;
    int element;
    int group;
```

```
    if(TS.isLittleEndian()){
        msGroupByte = (int)b[1];
        lsGroupByte = (int)b[0];
        msElementByte = (int)b[3];
        lsElementByte = (int)b[2];
    }
    else{
        msGroupByte = (int)b[0];
        lsGroupByte = (int)b[1];
        msElementByte = (int)b[2];
        lsElementByte = (int)b[3];
    }
    group = (msGroupByte << 8 | lsGroupByte);
    element = (msElementByte << 8 | lsElementByte);

    return new AttributeTag(group,element);
}

public static byte[] reorderBytesOneWord(TransferSyntax TS,byte[] b, int size){
    if(TS.isBigEndian()){
        if(size == 4){
            byte[] tempBuffer = {0,0,0,0};
            tempBuffer[0]=b[3];
            tempBuffer[1]=b[2];
            tempBuffer[2]=b[1];
            tempBuffer[3]=b[0];
            return tempBuffer;
        }
        else{
            byte[] tempBuffer = {0,0};
            tempBuffer[0]=b[1];
            tempBuffer[1]=b[0];
            return tempBuffer;
        }
    }
    else{ return b; }
}

public static byte[] reorderBytesTwoWords(TransferSyntax TS,byte[] b){
    if(TS.isBigEndian()){
        byte[] tempBuffer = {0,0,0,0};
        tempBuffer[0]=b[1];
        tempBuffer[1]=b[0];
        tempBuffer[2]=b[3];
        tempBuffer[3]=b[2];
        return tempBuffer;
    }
    else{ return b; }
}

public static int unsignedByteToInt(byte[] b){
    int firstByte;
    int secondByte;
    int unsignedInt;
    firstByte = (0x000000FF & ((int)b[1]));
    secondByte = (0x000000FF & ((int)b[0]));
    unsignedInt  = (firstByte << 8 | secondByte);
    return unsignedInt;
}

public static long unsignedByteToLong(byte[] b){
    int firstByte;
    int secondByte;
    int thirdByte;
    int fourthByte;
    long unsignedLong;
    firstByte = (0x000000FF & ((int)b[3]));
    secondByte = (0x000000FF & ((int)b[2]));
    thirdByte = (0x000000FF & ((int)b[1]));
    fourthByte = (0x000000FF & ((int)b[0]));
    unsignedLong  = ((long) (firstByte << 24 | secondByte << 16 | thirdByte << 8 | fourthByte)) & 0xFFFFFFFFL;
    return unsignedLong;
}

    public static int[] unsignedByteToSignedByte(byte[] b, int size){
    int[] temp = new int[size];
    if(size == 2){
        temp[0] = (0x000000FF & ((int)b[0]));
```

```
            temp[1] = (0x000000FF & ((int)b[0]));
        }
        else{
            temp[0] = (0x000000FF & ((int)b[0]));
            temp[1] = (0x000000FF & ((int)b[1]));
            temp[2] = (0x000000FF & ((int)b[2]));
            temp[3] = (0x000000FF & ((int)b[3]));
        }
        return temp;
    }

    public void readSequence() throws IOException {
        Vector<byte[]> unknownLengthDataSet = new Vector<byte[]>(200,40);
        boolean endOfSequence = false;
        while(endOfSequence == false){
        read(buffer2Bytes,0,2);
        if(unsignedByteToInt(reorderBytesOneWord(currentSyntax,buffer2Bytes,2)) != 0xFFFE){
            byte[] temp = {buffer2Bytes[0],buffer2Bytes[1]};
            unknownLengthDataSet.add(temp);
        }
        else{
            byte[] temp = {buffer2Bytes[0],buffer2Bytes[1]};
            unknownLengthDataSet.add(temp);
            read(buffer2Bytes,0,2);
            if(unsignedByteToInt(reorderBytesOneWord(currentSyntax,buffer2Bytes,2)) != 0xE0DD){
                byte[] temp2 = {buffer2Bytes[0],buffer2Bytes[1]};
                unknownLengthDataSet.add(temp2);
            }
            else{
                byte[] temp2 = {buffer2Bytes[0],buffer2Bytes[1]};
                unknownLengthDataSet.add(temp2);
                skip(4);
                endOfSequence = true;
            }
        }
    }
    file.close();
  }


  public DataSet getDataSet(){
    if(dataElements!= null){return dataElements;}
    else return null;
  }

}
```

MainMenue_

```
/**
 * A GUI for reading DICOM files
 * @author Andrew Blair
 * @version 2.0 December 2008
 */

import java.awt.*;
import java.io.*;
import java.util.*;
import java.awt.event.*;
import java.awt.SystemColor;
import java.io.*;
import java.lang.*;
import javax.swing.*;
import ij.plugin.frame.*;
import ij.*;
import ij.gui.*;
import ij.process.ImageProcessor;

public class MainMenue_ extends PlugInFrame implements ActionListener
{
  String dir_ana;
  String str;
  String resstr;
  int arrayLength = 0;
```

```
float fluoroMetric = 0;
JPanel panel;
JButton buttonAna,buttonDirAna;
JTextArea TAinfo;
JTextField textDir;
JTextField fluoroTimeField;
JTextField fluoroDAPField;
JTextField fluoroReportedField;
Checkbox checkSD;
Checkbox checkFluoroTime;
Checkbox checkFluoroDAP;
Checkbox checkFluoroReported;
Checkbox methodEven;
Checkbox methodWeighted;
boolean bShow_SD=true;
boolean bFluoroTime = true;
boolean bFluoroDAP = false;
boolean bFluoroReported = false;
boolean bmethodEven = true;
boolean bmethodWeighted = false;
DataSet[] dataSetArray;
int numberOfViews = 0;
int paramChoice = 0;
int methodChoice = 0;

public MainMenue_()
{
   super("Scan DICOM info");
   setBackground(SystemColor.control);
   setLayout(new BorderLayout());
   panel = new JPanel();
   panel.setLayout(new GridLayout(0,3));
   panel.setBackground(SystemColor.control);
   panel.add(new JLabel("Analyse DICOM images in:"));
   textDir=new JTextField("G:\\ ");
   panel.add(textDir);
   buttonDirAna=new JButton("Choose...");
   buttonDirAna.addActionListener(this);
   panel.add(buttonDirAna);

   panel.add(new JLabel("Fluoro time (min):"));
   fluoroTimeField=new JTextField("0");       panel.add(fluoroTimeField);
   checkFluoroTime=new Checkbox("Use Fluoro time?",true);       panel.add(checkFluoroTime);

   panel.add(new JLabel("Fluoro DAP (uGy/m2):"));
   fluoroDAPField=new JTextField("0");       panel.add(fluoroDAPField);
   checkFluoroDAP=new Checkbox("Use Fluoro DAP?",false);       panel.add(checkFluoroDAP);

   panel.add(new JLabel("Fluoro Reported (mGy):"));
   fluoroReportedField=new JTextField("0");       panel.add(fluoroReportedField);
    checkFluoroReported=new Checkbox("Use reported dose?",false);                  panel.add(checkFluoroReported);
   methodEven=new Checkbox("Even distribution?",true);       panel.add(methodEven);
    methodWeighted=new Checkbox("Weighted distribution?",false);            panel.add(methodWeighted);
   checkSD=new Checkbox("Analyse subdirs?",true);
   panel.add(checkSD);

   buttonAna = new JButton("Start analysis");
   buttonAna.addActionListener(this);
   panel.add(buttonAna);

   add(panel, BorderLayout.NORTH);
   TAinfo=new JTextArea(20,20);
   TAinfo.setEditable(false);
   JScrollPane JSP=new JScrollPane(TAinfo);
   add(JSP,BorderLayout.SOUTH);
   pack();
   show();
}


public void actionPerformed(ActionEvent e)
{
   dir_ana=textDir.getText();
   bShow_SD=checkSD.getState();
   bFluoroTime= checkFluoroTime.getState();
   bFluoroDAP= checkFluoroDAP.getState();
   bFluoroReported= checkFluoroReported.getState();
   bmethodEven = methodEven.getState();
```

```
    bmethodWeighted = methodWeighted.getState();

    if (e.getSource() == buttonDirAna)
    {
       JFileChooser fc = new JFileChooser(textDir.getText());
       fc.setDialogTitle("Select a file in the directory to be analysed...");
       int returnVal=fc.showOpenDialog(this);
       if (returnVal == JFileChooser.APPROVE_OPTION)
       {
             textDir.setText(fc.getCurrentDirectory().getAbsolutePath());
             panel.updateUI();
       }
          return;
    }

    if (e.getSource() == buttonAna)
    {
       arrayLength = 0;
       fluoroMetric = Float.parseFloat(fluoroTimeField.getText());
       Date dt=new Date();
       TAinfo.setText("");
       TAinfo.append("Date and time of analysis: "+dt+"\n");
       dataSetArray = new DataSet[200];
       readFiles(dir_ana);
       sortDetails();
       TAinfo.append("\n" + arrayLength + "\t files were stored \t and " + dataSetArray.length + " views were found");

       if(bFluoroTime){ paramChoice = 1; fluoroMetric = Float.parseFloat(fluoroTimeField.getText());}
       else if(bFluoroDAP){ paramChoice = 2; fluoroMetric = Float.parseFloat(fluoroDAPField.getText());}
       else { paramChoice = 3; fluoroMetric = Float.parseFloat(fluoroReportedField.getText());}

       if(bmethodEven){ methodChoice = 1;} else if(bmethodWeighted){ methodChoice = 2;} else { methodChoice = 3; }

       ImagePlus radiationFields = DrawFields.drawFields(dataSetArray,paramChoice, methodChoice, fluoroMetric,1,0 );
       radiationFields.show();
       IJ.resetMinAndMax();
       return;
    }
}

/** ------------------------------------------------
 * Read files
 */

public void readFiles(String dir1)       //show only specific tags
{
    int i,j;
    File_Reader currentFile;
    File f;
    String[]list=new File(dir1).list();
    if (list==null) return;
    for (int i0=0; i0<list.length; i0++)
    {
       f = new File(dir1+"\\"+list[i0]);
       if (!f.isDirectory())
       {
          try
          {
             currentFile = new File_Reader(dir1+"\\"+list[i0]);
             currentFile.findDicomDetails();
             dataSetArray[arrayLength]=currentFile.getDataSet();
             TAinfo.append(f.toString()+"\t This was read \n");
             arrayLength++;
          }

          catch (Exception e)
          {
             IJ.write("Something went wrong");
             System.out.println(e);
          }
       }
       else
       {
          TAinfo.append(f.toString()+"\t Is a directory \n");
          if (bShow_SD){ readFiles(dir1+"\\"+list[i0]);}
       }
    }
}
```

```
/** ------------------------------------------------------
 * Sort to find valid files and store in a ideal size array.
 */
public void sortDetails(){
if(arrayLength != 0){
      int sumSPD = 0;
      findValidElements();
      DataSet[] tempSet = new DataSet[numberOfViews];
      int index = 0;
   if(numberOfViews != 0){
      for(int k =0;k<arrayLength; k++){
         try{
                float kVp = Float.parseFloat( new String(
                (byte[])(dataSetArray[k].getElement(TagFromName.KVP).getValueField())));
                int xRayTubeCurrent = Integer.parseInt( new String(
                (byte[])(dataSetArray[k].getElement(TagFromName.XrayTubeCurrent).getValueField())).trim()); //IS
                int exposureTime = Integer.parseInt( new String(
                (byte[])(dataSetArray[k].getElement(TagFromName.ExposureTime).getValueField())).trim()); //IS
                int cineRate = Integer.parseInt( new String(
                (byte[])(dataSetArray[k].getElement(TagFromName.CineRate).getValueField())).trim()); //IS
                float averagePulseWidth = Float.parseFloat( new String(
                (byte[])(dataSetArray[k].getElement(TagFromName.AveragePulseWidth).getValueField())).trim()); //DS
                float imageAndFluoroscopyAreaDoseProduct = Float.parseFloat( new String(
                (byte[])(dataSetArray[k].getElement(TagFromName.ImageAndFluoroscopyAreaDoseProduct).getValueField
                ())).trim()); //DS
                int sPD = (int)Float.parseFloat( new String(
                (byte[])(dataSetArray[k].getElement(TagFromName.DistanceSourceToPatient).getValueField())).trim());
                tempSet[index] = dataSetArray[k];
                index ++;
         }
         catch(Exception e){}
         }
         int averageSPD = sumSPD / numberOfViews;
         TAinfo.append("\n" + "Average SPD: " + averageSPD);
         dataSetArray = tempSet;
      }
   }
}

/** ------------------------------------------------------
 * Work-around method to find the number of valid views.
 */
   public void findValidElements(){
      numberOfViews = 0;
   for(int k =0;k<arrayLength; k++){
         try{
                float kVp = Float.parseFloat( new String(
                (byte[])(dataSetArray[k].getElement(TagFromName.KVP).getValueField())));
                int xRayTubeCurrent = Integer.parseInt( new String(
                (byte[])(dataSetArray[k].getElement(TagFromName.XrayTubeCurrent).getValueField())).trim()); //IS
                int exposureTime = Integer.parseInt( new String(
                (byte[])(dataSetArray[k].getElement(TagFromName.ExposureTime).getValueField())).trim()); //IS
                int cineRate = Integer.parseInt( new String(
                (byte[])(dataSetArray[k].getElement(TagFromName.CineRate).getValueField())).trim()); //IS
                float averagePulseWidth = Float.parseFloat( new String(
                (byte[])(dataSetArray[k].getElement(TagFromName.AveragePulseWidth).getValueField())).trim()); //DS
                float imageAndFluoroscopyAreaDoseProduct = Float.parseFloat( new String(
                (byte[])(dataSetArray[k].getElement(TagFromName.ImageAndFluoroscopyAreaDoseProduct).getValueField
                ())).trim()); //DS
                int sPD = (int)Float.parseFloat( new String(
                (byte[])(dataSetArray[k].getElement(TagFromName.DistanceSourceToPatient).getValueField())).trim());
                numberOfViews++;
         }
         catch(Exception e){}
        }
      }

public void runSimulation(String dir, int paramChoice, int methodChoice, float metric, int iter)
{
arrayLength = 0;
dataSetArray = new DataSet[200];
readFiles(dir);
sortDetails();
if(numberOfViews != 0){
   for(int couch = 0; couch <2; couch ++){
       ImagePlus radiationFields = DrawFields.drawFields(dataSetArray,paramChoice, methodChoice, metric, iter, couch
       );
```

```
            radiationFields.setDisplayRange(0,(radiationFields.getChannelProcessor()).getHistogramMax());
            IJ.saveAs(radiationFields,"jpeg",dir + " " + couch);
            radiationFields.close();
        }
    }
    }
}
```

DrawFields

```
/**
 * A class which accepts an array of dataSet's and calculates fields of exposure.
 * @ Andrew Blair
 * @ 1.0 June 2008
 */

import ij.*;
import ij.gui.*;
import ij.process.ImageProcessor;
import java.util.*;
import java.io.*;
import java.awt.Polygon;
import java.awt.Rectangle;
import javax.vecmath.Vector3d;

public class DrawFields
{
    public DrawFields(){}
    public static ImagePlus drawFields(DataSet[] dataSet, int paramChoice, int methodChoice, float param, int iter, int table)
    {
        /**
         * ParamChoice  1. Time          MethodChoice          1. Even
         *              2. DAP                                 2. Weighted
         *              3. Dose
         */

        DataSet[] dataArray = dataSet;
        float fluoroMetric = param;
        int couchHeightMethod = table;
        DataSet currentDataSet;
          ImagePlus radiationFields = NewImage.createFloatImage("Radiation
          Fields",2048/2,2500/2,1,NewImage.FILL_WHITE);
        int numberOfFields=dataArray.length;
        double pixelToDistanceRatio = 1.0/0.168/2;     //in pixels per mm
        int counter = 0;
        float averageKVP = 0;
        float tableHeight = 750;
        float totalCineDose=0;
        float totalFluoroDose = 0;
        float totalDose = 0;
        float fluoroDose =0;
        float maxDose = 0;
        float totalCineDAP = 0;
        float totalDAP = 0;
        float totalReportedDAP =0;
        double currentMin=100000;

        System.out.println("kVp" + "\t" + "mA" + "\t" + "ang1" + "\t" + "ang2" + "\t" + "dose" + "\n");

        /** Find table height, total Cine DAP and average kVp */

        while(counter < numberOfFields)
        {
            try {
                currentDataSet = dataArray[counter];
                float positionerPrimaryAngle = -1* Float.parseFloat( new String(
                (byte[])(currentDataSet.getElement(TagFromName.PositionerPrimaryAngle).getValueField())).trim()); //DS
                float positionerSecondaryAngle = -1* Float.parseFloat( new String(
                (byte[])(currentDataSet.getElement(TagFromName.PositionerSecondaryAngle).getValueField())).trim()); //DS
                float kVp = Float.parseFloat( new String(
                (byte[])(currentDataSet.getElement(TagFromName.KVP).getValueField())));
                float areaDoseProduct = Float.parseFloat( new String(
                (byte[])(currentDataSet.getElement(TagFromName.ImageAndFluoroscopyAreaDoseProduct).getValueField())).t
                rim()); //DS
                averageKVP += kVp;
```

```
            totalReportedDAP += areaDoseProduct;
            double sumSquares = Math.pow(positionerPrimaryAngle,2) + Math.pow(positionerSecondaryAngle,2);
            if(sumSquares < currentMin){
            tableHeight = Float.parseFloat( new String(
            (byte[])(currentDataSet.getElement(TagFromName.DistanceSourceToPatient).getValueField())).trim()) - 184;
            //DS
            currentMin = sumSquares;
          }
       }

       catch (Exception e){}
       finally { counter++;}
}

if(couchHeightMethod!=0) { tableHeight = 750 - 120; }


  averageKVP = averageKVP / numberOfFields;
         if(paramChoice == 1){ // Fluoro time
        fluoroDose = ((float)Math.log((averageKVP + 3)) * 101 - 414.3f) * fluoroMetric * 1.2f; // Smaller BSF added to the
        unfors reading
         }
        if(paramChoice == 2){ fluoroMetric = fluoroMetric/10;} // Converting DAP to appropriate units. Done here to give
        same call from scripter and GUI.
if(paramChoice == 2 && paramChoice == 3 ){ // DAP or Reported dose
   fluoroMetric = fluoroMetric * (1-(31388*(float)Math.pow(averageKVP,-1.71))/100) * 1.405f;
}

counter = 0;
while(counter < numberOfFields)
{
       currentDataSet = dataArray[counter];
          try {
          float kVp = Float.parseFloat( new String(
          (byte[])(currentDataSet.getElement(TagFromName.KVP).getValueField())));
          String radiationSetting = new String(
          (byte[])(currentDataSet.getElement(TagFromName.RadiationSetting).getValueField()));
          int cineRate = Integer.parseInt( new String(
          (byte[])(currentDataSet.getElement(TagFromName.CineRate).getValueField())).trim());
          int xRayTubeCurrent = Integer.parseInt( new String(
          (byte[])(currentDataSet.getElement(TagFromName.XrayTubeCurrent).getValueField())).trim())
          int exposureTime = Integer.parseInt( new String(
          (byte[])(currentDataSet.getElement(TagFromName.ExposureTime).getValueField())).trim());
          float areaDoseProduct = Float.parseFloat( new String(
          (byte[])(currentDataSet.getElement(TagFromName.ImageAndFluoroscopyAreaDoseProduct).getValueField())).t
          rim());
          float averagePulseWidth = Float.parseFloat( new String(
          (byte[])(currentDataSet.getElement(TagFromName.AveragePulseWidth).getValueField())).trim());
          float intensifierSize = Float.parseFloat( new String(
          (byte[])(currentDataSet.getElement(TagFromName.IntensifierSize).getValueField())).trim());
          float positionerPrimaryAngle = Float.parseFloat( new String(
          (byte[])(currentDataSet.getElement(TagFromName.PositionerPrimaryAngle).getValueField())).trim());
          float positionerSecondaryAngle = Float.parseFloat( new String(
          (byte[])(currentDataSet.getElement(TagFromName.PositionerSecondaryAngle).getValueField())).trim());
          float distanceSourceToPatient = Float.parseFloat( new String(
          (byte[])(currentDataSet.getElement(TagFromName.DistanceSourceToPatient).getValueField())).trim());
          float distanceSourceToDetector = Float.parseFloat( new String(
          (byte[])(currentDataSet.getElement(TagFromName.DistanceSourceToDetector).getValueField())).trim());
          String shutterShape = (new String(
          (byte[])(currentDataSet.getElement(TagFromName.ShutterShape).getValueField()))).trim();

         /**
          * * * Calculate the 4 points of the square.
          */
          float radius = 750; // was 600 mm
          double zTableHeight = tableHeight - 750;
          float magnificationFactor = distanceSourceToPatient/distanceSourceToDetector;
          float fieldSize;
          if(shutterShape.equals("RECTANGULAR")){fieldSize = (float)(intensifierSize *
          Math.sin(Math.toRadians(45)));}else{fieldSize = intensifierSize;}
          fieldSize = fieldSize - 10; // Add a 10mm extra collimation since the radiation field is smaller than the reported
          size.
          double primaryAngle = -1*Math.toRadians(positionerPrimaryAngle);
          double secondaryAngle = -1*Math.toRadians(positionerSecondaryAngle);
          double dPrimaryAngle = Math.atan((fieldSize/2)/(distanceSourceToDetector-750));
          double dSecondaryAngle = dPrimaryAngle;
          double radCol = distanceSourceToDetector-750;
```

```
double xSpot = -radius*Math.cos(secondaryAngle)*Math.sin(primaryAngle);
double ySpot = -radius*Math.sin(secondaryAngle);
double zSpot = -radius *Math.cos(primaryAngle)*Math.cos(secondaryAngle);

   double xSide1 = radCol * Math.cos(secondaryAngle+dSecondaryAngle)*Math.sin(primaryAngle);
   double xSide2 = radCol * Math.cos(secondaryAngle-dSecondaryAngle)*Math.sin(primaryAngle);
   double xSide3 = radCol * Math.cos(secondaryAngle)*Math.sin(primaryAngle + dPrimaryAngle);
   double xSide4 = radCol * Math.cos(secondaryAngle)*Math.sin(primaryAngle - dPrimaryAngle);

double ySide1 = radCol * Math.sin(secondaryAngle + dSecondaryAngle);
double ySide2 = radCol * Math.sin(secondaryAngle - dSecondaryAngle);
double ySide3 = radCol * Math.sin(secondaryAngle);
double ySide4 = ySide3;

   double zSide1 = radCol * Math.cos(primaryAngle)*Math.cos(secondaryAngle + dSecondaryAngle);
   double zSide2 = radCol * Math.cos(primaryAngle)*Math.cos(secondaryAngle - dSecondaryAngle);
   double zSide3 = radCol * Math.cos(primaryAngle + dPrimaryAngle)*Math.cos(secondaryAngle);
   double zSide4 = radCol * Math.cos(primaryAngle - dPrimaryAngle)*Math.cos(secondaryAngle);


double xCentre = radCol * Math.cos(secondaryAngle)*Math.sin(primaryAngle);
double yCentre = radCol * Math.sin(secondaryAngle);
double zCentre = radCol * Math.cos(primaryAngle)*Math.cos(secondaryAngle);

// ******* Parametric Equations ******* \\

/** Line to centre */
double xCentreLine = xCentre;
double yCentreLine = yCentre;
double zCentreLine = zCentre;

/** Side 1 */

double t = ((Math.pow(xCentre,2)+Math.pow(yCentre,2)+Math.pow(zCentre,2)))
/(xCentre*(xSide1)+yCentre*(ySide1)+zCentre*(zSide1));
double xline1 = (xSide1)*t;double yline1 = (ySide1)*t;double zline1 = (zSide1)*t;
double[] point1 = {xline1,yline1,zline1};
   double distanceToSide1 = Math.sqrt(Math.pow((xline1-xCentre),2)+Math.pow((yline1-
   yCentre),2)+Math.pow((zline1-zCentre),2));
   double isInPlane1 = -xCentre*(xline1-xCentre)-yCentre*(yline1-yCentre)-zCentre*(zline1-zCentre);

   /** Side 2 */
   t = ((Math.pow(xCentre,2)+Math.pow(yCentre,2)+Math.pow(zCentre,2)))
   /(xCentre*(xSide2)+yCentre*(ySide2)+zCentre*(zSide2));
   double xline2 = (xSide2)*t;double yline2 = (ySide2)*t;double zline2 = (zSide2)*t;
   double[] point2 = {xline2,yline2,zline2};
   double distanceToSide2 = Math.sqrt(Math.pow((xline2-xCentre),2)+Math.pow((yline2-
   yCentre),2)+Math.pow((zline2-zCentre),2));
   double isInPlane2 = -xCentre*(xline2-xCentre)-yCentre*(yline2-yCentre)-zCentre*(zline2-zCentre);

/** Side 3 */

Vector3d vec1 = new Vector3d(-xCentre,-yCentre,-zCentre);
Vector3d vec2 = new Vector3d(xline1-xCentre,yline1-yCentre,zline1-zCentre);
Vector3d vec3 = new Vector3d();
vec3.cross(vec1,vec2);
double xVectSide1= ((0-yCentre)*(zline1-zCentre)) - ((0-zCentre)*(yline1-yCentre));
double yVectSide1= -(((0-xCentre)*(zline1-zCentre)) - ((0-zCentre)*(xline1-xCentre)));
double zVectSide1= ((0-xCentre)*(yline1-yCentre)) - ((0-yCentre)*(xline1-xCentre));
   t = (fieldSize/2)/(Math.sqrt(Math.pow(xVectSide1,2)+Math.pow(yVectSide1,2)+Math.pow(zVectSide1,2)));
   double xline3 = xCentre + xVectSide1*t;double yline3 = yCentre + yVectSide1*t;double zline3 = zCentre +
   zVectSide1*t;
   double[] point3 = {xline3,yline3,zline3};
   double distanceToSide3 = Math.sqrt(Math.pow((xline3-xCentre),2)+Math.pow((yline3-
   yCentre),2)+Math.pow((zline3-zCentre),2));
   double isInPlane3 = -xCentre*(xline3-xCentre)-yCentre*(yline3-yCentre)-zCentre*(zline3-zCentre);


/** Side 4 */

Vector3d vec4 = new Vector3d();
vec4.cross(vec2,vec1);
double xVectSide2= ((yline1-yCentre)*(0-zCentre)) - ((zline1-zCentre)*(0-yCentre));
double yVectSide2= -(((xline1-xCentre)*(0-zCentre)) - ((zline1-zCentre)*(0-xCentre)));
double zVectSide2= ((xline1-xCentre)*(0-yCentre)) - ((yline1-yCentre)*(0-xCentre));
   t = (fieldSize/2)/(Math.sqrt(Math.pow(xVectSide2,2)+Math.pow(yVectSide2,2)+Math.pow(zVectSide2,2)));
   double xline4 = xCentre + xVectSide2*t;double yline4 = yCentre + yVectSide2*t;double zline4 = zCentre +
   zVectSide2*t;
```

```
   double[] point4 = {xline4,yline4,zline4};
   double distanceToSide4 = Math.sqrt(Math.pow((xline4-xCentre),2)+Math.pow((yline4-
   yCentre),2)+Math.pow((zline4-zCentre),2));
   double isInPlane4 = -xCentre*(xline4-xCentre)-yCentre*(yline4-yCentre)-zCentre*(zline4-zCentre);

/** Vector Corner 1 */
double xVec1 = ( (point1[0]-xCentre)+ (point3[0]-xCentre));
double yVec1 = ( (point1[1]-yCentre)+ (point3[1]-yCentre));
double zVec1 = ( (point1[2]-zCentre)+ (point3[2]-zCentre));

   double vectorLength1 = Math.sqrt(Math.pow(xVec1,2)+Math.pow(yVec1,2)+Math.pow(zVec1,2));

double xCorner1 = xCentre + xVec1;
double yCorner1 = yCentre + yVec1;
double zCorner1 = zCentre + zVec1;

t = (zTableHeight-zSpot)/(zCorner1-zSpot);
double xCornerLine1 = xSpot + (xCorner1 - xSpot)*t;
double yCornerLine1 = ySpot + (yCorner1 - ySpot)*t;
double zCornerLine1 = zSpot + (zCorner1 - zSpot)*t;
double[] corner1 = {xCornerLine1,yCornerLine1};

/** Vector Corner 2 */
double xVec2 = ( (point1[0]-xCentre)+ (point4[0]-xCentre));
double yVec2 = ( (point1[1]-yCentre)+ (point4[1]-yCentre));
double zVec2 = ( (point1[2]-zCentre)+ (point4[2]-zCentre));
   double vectorLength2 = Math.sqrt(Math.pow(xVec2,2)+Math.pow(yVec2,2)+Math.pow(zVec2,2));
double xCorner2 = xCentre + xVec2;
double yCorner2 = yCentre + yVec2;
double zCorner2 = zCentre + zVec2;
t = (zTableHeight-zSpot)/(zCorner2-zSpot);
double xCornerLine2 = xSpot + (xCorner2 - xSpot)*t;
double yCornerLine2 = ySpot + (yCorner2 - ySpot)*t;
double zCornerLine2 = zSpot + (zCorner2 - zSpot)*t;
double[] corner2 = {xCornerLine2, yCornerLine2};

/** Vector Corner 3 */
double xVec3 = ( (point2[0]-xCentre)+ (point3[0]-xCentre));
double yVec3 = ( (point2[1]-yCentre)+ (point3[1]-yCentre));
double zVec3 = ( (point2[2]-zCentre)+ (point3[2]-zCentre));
   double vectorLength3 = Math.sqrt(Math.pow(xVec3,2)+Math.pow(yVec3,2)+Math.pow(zVec3,2));
double xCorner3 = xCentre + xVec3;
double yCorner3 = yCentre + yVec3;
double zCorner3 = zCentre + zVec3;
t = (zTableHeight-zSpot)/(zCorner3-zSpot);
double xCornerLine3 = xSpot + (xCorner3 - xSpot)*t;
double yCornerLine3 = ySpot + (yCorner3 - ySpot)*t;
double zCornerLine3 = zSpot + (zCorner3 - zSpot)*t;
double[] corner3 = {xCornerLine3, yCornerLine3};

/** Vector Corner 4 */
double xVec4 = ( (point2[0]-xCentre)+ (point4[0]-xCentre));
double yVec4 = ( (point2[1]-yCentre)+ (point4[1]-yCentre));
double zVec4 = ( (point2[2]-zCentre)+ (point4[2]-zCentre));
   double vectorLength4 = Math.sqrt(Math.pow(xVec4,2)+Math.pow(yVec4,2)+Math.pow(zVec4,2));
double xCorner4 = xCentre + xVec4;
double yCorner4 = yCentre + yVec4;
double zCorner4 = zCentre + zVec4;
t = (zTableHeight-zSpot)/(zCorner4-zSpot);
double xCornerLine4 = xSpot + (xCorner4 - xSpot)*t;
double yCornerLine4 = ySpot + (yCorner4 - ySpot)*t;
double zCornerLine4 = zSpot + (zCorner4 - zSpot)*t;
double[] corner4 = {xCornerLine4, yCornerLine4};

/** Centre line test */
t = (zTableHeight-zSpot)/(zCentre-zSpot);
double xCentreLine4 = xSpot + (xCentre - xSpot)*t;
double yCentreLine4 = ySpot + (yCentre - ySpot)*t;
double zCentreLine4 = zSpot + (zCentre - zSpot)*t;
double[] corner5 = {xSpot + (xCentreLine4-xSpot)*t, ySpot + (yCentreLine4-ySpot)*t};
double xCenterOfMass = (corner1[0] + corner2[0] + corner3[0] + corner4[0]) / 4;
double yCenterOfMass = (corner1[1] + corner2[1] + corner3[1] + corner4[1]) / 4;
double angle1 = Math.atan2(corner1[1]-yCenterOfMass,corner1[0]-xCenterOfMass);
double angle2 = Math.atan2(corner2[1]-yCenterOfMass,corner2[0]-xCenterOfMass);
double angle3 = Math.atan2(corner3[1]-yCenterOfMass,corner3[0]-xCenterOfMass);
double angle4 = Math.atan2(corner4[1]-yCenterOfMass,corner4[0]-xCenterOfMass);
double[] angles = {angle1,angle2,angle3,angle4};
```

```
Arrays.sort(angles);

Hashtable set = new Hashtable();
set.put(angle1,corner1);
set.put(angle2,corner2);
set.put(angle3,corner3);
set.put(angle4,corner4);

Vector points = new Vector(4);
points.add(set.get(angles[0]));
points.add(set.get(angles[1]));
points.add(set.get(angles[2]));
points.add(set.get(angles[3]));

/**
 * Draw fields.
 */

  if(shutterShape.equals("RECTANGULAR") && positionerPrimaryAngle < 70 && positionerSecondaryAngle <70){
  ImageProcessor imp = radiationFields.getProcessor();
  int width = imp.getWidth();
  int height = imp.getHeight();

    int[] xPoints = {(int)(width/2 + ((int)((double[])points.get(0))[0]*pixelToDistanceRatio)),(int)(width/2 +
    ((int)((double[])points.get(1))[0]*pixelToDistanceRatio)),
     (int)(width/2 + ((int)((double[])points.get(2))[0]*pixelToDistanceRatio)),(int)(width/2 +
    ((int)((double[])points.get(3))[0]*pixelToDistanceRatio))};
    int[] yPoints = {(int)(height/2 + ((int)((double[])points.get(0))[1]*pixelToDistanceRatio)),(int)(height/2 +
    ((int)((double[])points.get(1))[1]*pixelToDistanceRatio)),
     (int)(height/2 + ((int)((double[])points.get(2))[1]*pixelToDistanceRatio)),(int)(height/2 +
    ((int)((double[])points.get(3))[1]*pixelToDistanceRatio))};
    PolygonRoi currentField = new PolygonRoi(xPoints,yPoints,4,Roi.POLYGON);
    Rectangle boundingBox = currentField.getBounds();

  /**
  * Find the Dose
  */
    float area = (float)Math.pow((fieldSize*(tableHeight/distanceSourceToDetector)),2); //mm2
    float dose = areaDoseProduct/area*10000 *1.08f; // in mGy, machine DAP is stored as dGycm2
    float fluoroDosePerField = 0;

 /** Find Fluoro Dose */
 if(paramChoice == 1){ //fluoro time
    if(methodChoice == 1){ // Even dist
       fluoroDosePerField = fluoroDose/numberOfFields;
     }
     if(methodChoice == 2){ // Weighted
        fluoroDosePerField = fluoroDose * areaDoseProduct / totalReportedDAP;
     }
 }

 if(paramChoice == 2){ // DAP
    if(methodChoice == 1){ // Even dist
       fluoroDosePerField = fluoroMetric/area*10000/numberOfFields;
     }
     if(methodChoice == 2){ // Weighted
           fluoroDosePerField = fluoroMetric/area*10000* areaDoseProduct / totalReportedDAP;
     }
  }

  if(paramChoice == 3){ // DAP
    if(methodChoice == 1){ // Even dist
       fluoroDosePerField = fluoroMetric/numberOfFields;
     }
     if(methodChoice == 2){ // Weighted
       fluoroDosePerField = fluoroMetric * areaDoseProduct / totalReportedDAP;
     }
  }


    float correction = 31388*(float)Math.pow(kVp,-1.71); // Correction in % for table attenuation and kVp response
    of DAP meter.
 float bsf;
    if(kVp<70){ bsf = 1.39f; }   else if(kVp>100){ bsf = 1.42f; }    else { bsf = 0.001f * kVp + 1.32f; }

 float DAP = areaDoseProduct * (1-correction/100) * bsf ;
 totalCineDAP = totalCineDAP + DAP;
 DAP = DAP + fluoroDosePerField * area/10000 *1.08f;
```

```
                totalDAP = totalDAP + DAP;
                dose = dose * (1-correction/100) * bsf ;
                totalCineDose = totalCineDose + dose;
                dose = dose + fluoroDosePerField * 1.08f;
                totalDose = totalDose + dose;
                   System.out.println(kVp + "\t" + xRayTubeCurrent + "\t" + positionerPrimaryAngle + "\t" +
                   positionerSecondaryAngle + "\t" + dose + "\n");
                /**
                 * Fill in the pixels with dose based on DAP.
                 */
                int boxWidth = (int)boundingBox.getWidth();
                int boxHeight = (int)boundingBox.getHeight();
                int boxX = (int)boundingBox.getX();
                int boxY = (int)boundingBox.getY();

                for(int j = boxY;j<(boxY+boxHeight);j++){
                   for(int i = boxX; i<(boxWidth+boxX); i++){
                      if(currentField.contains(i,j)){
                         float currentPixel = imp.getf(i,j);
                         float newDose = currentPixel + dose;
                         if(newDose > maxDose){maxDose = currentPixel + dose;}
                         imp.setf(i,j,newDose);
                      }
                   }
                }
             }
          }

          catch (Exception e){
          System.err.println(e.getMessage());}
          finally { counter++;}

       }
       /**
        * Print details to file -----------------------------------
        */

         String patientName = new String( (byte[])(dataSet[0].getElement(TagFromName.PatientName).getValueField()));
       String fileName;
       if(paramChoice ==1){ fileName = "C:\\Patient CDs\\Fluorotime"; }
       else if(paramChoice ==2){ fileName = "C:\\Patient CDs\\Reported DAP"; }
       else { fileName = "C:\\Patient CDs\\Reported Dose"; }
       if(methodChoice ==1){ fileName = fileName + " Even"; }
       else { fileName = fileName + " Weighted"; }
       if(couchHeightMethod ==1){ fileName = fileName + " fixed.txt"; }
       else { fileName = fileName + " auto.txt"; }
       try {
          PrintWriter out  = new PrintWriter(new BufferedWriter(new FileWriter(fileName,true)));
          boolean error = false;
          if(iter ==1){
             out.println(fileName);
                out.write("Patient name" + "\t MaxDose \t CouchHeight \t TotalCineDap (Reported) \t TotalCineDose \t
                TotalFluoroDAP \t TotalFluoroDose \t TotalDAP \t TotalDose");
             out.println();
             error = out.checkError();
          }
           out.write(patientName + "\t" + maxDose + "\t" + (tableHeight-750)/10 +"\t" + totalCineDAP/10 + "\t" + totalCineDose
           + "\t" + (totalDAP-totalCineDAP)
          + "\t" + (totalDose - totalCineDose) + "\t" + totalDAP/10 + "\t" + totalDose);
          out.println();
          out.close();
       }
         catch( IOException e){System.err.println(e.getMessage());}
         System.out.println("-------------------------------------" + " \n Max dose: " + (int)maxDose + " mGy" + "\t couch height: " +
         (int)((tableHeight-750)/10) + " cm" );
         System.out.println("\n Total Cine DAP (reported): " + (int)totalCineDAP/10+"("+(int)totalReportedDAP/10+")" + "
         Gy/cm2" + "\t Total cine dose: " + (int)totalCineDose + " mGy" );
         System.out.println("\n Total fluoro DAP: " + (int)(totalDAP-totalCineDAP) + " dGycm2" + "\t Total fluoro dose
         (calculated): " + (int)(totalDose - totalCineDose) + " mGy");
         System.out.println("\n Total DAP: " + (int)totalDAP/10  + " Gy/cm2" + "\t Total dose: " + (int)totalDose + " mGy");
         return radiationFields;
   }
}
```